SILICON NANOCRYSTALS AND DEFECT STATES IN SILICON RICH SILICON NITRIDE FOR OPTOELECTRONIC APPLICATIONS

by

Shakil Mohammed

APPROVED BY SUPERVISORY COMMITTEE:

_____

Stuart F. Cogan, Chair

_____

Orlando Auciello

_____

Anton V. Malko

_____

Joseph J. Pancrazio

_____

Walter E. Voit

*In memory of my father*

# SILICON NANOCRYSTALS AND DEFECT STATES IN SILICON RICH SILICON NITRIDE FOR OPTOELECTRONIC APPLICATIONS

by

Shakil Mohammed, BS, MS

DISSERTATION

Presented to the Faculty of

The University of Texas at Dallas

in Partial Fulfillment

of the Requirements

for the Degree of

DOCTOR OF PHILOSOPHY IN

MATERIALS SCIENCE AND ENGINEERING

THE UNIVERSITY OF TEXAS AT DALLAS

December 2016

# ACKNOWLEDGEMENTS

I would first like to thank my adviser Dr. Stuart F. Cogan for giving me the opportunity of completing my PhD under his guidance and also supporting and encouraging me during my most difficult times at the graduate school. I am extremely grateful that I had the opportunity to work with him and his diverse group at the Neural Interfaces Laboratory who have been like a part of my family. My heartfelt gratitude goes to Dr. Alexandra Joshi-Imre, Dr. Jimin Maeng and the graduate students who were behind each of my successes during the recent months. In addition, I would like to extend my appreciation to my committee members, especially Prof. Joseph Pancrazio and Dr. Walter Voit for their support and encouragement at different events. I would like to acknowledge Dr. Anton Malko and his team, Dr. Siddharth Sampat and Mike Nimmo for helping with the photoluminescence measurements. Dr. Yuanning Chen of Microsol Technologies, who has supported me financially and has been a moral support throughout the years – I will always be in debt to her. I would like to acknowledge Dr. Chris Hinkle for funding me during the earlier years at UT Dallas and also allowing me to use all the data and analysis in this dissertation. Everyone else who walked in different phases during my graduate years at UT Dallas including Dr. Israel Mejia, Dr. Sarkar Anwar, Dr. Bhaswar Chakrabarti, Dr. Hong Dong, Jing Yang, Dewan Kabir, Natis Shafiq, Creighton Buie and so many others – they will always remain as a shining light in my life for their friendship, mentorship and selfless cooperation. The outstanding cleanroom staffs Mr. Wallace Martin, Dr. Gordon Pollack, Mr. Scott Riekena and Mr. John Maynard have been extremely caring and helpful towards training and allowing me access to complex equipment for all of my experimental needs. Finally, I cannot but thank my better half

Nujhat, for bearing all the difficulties with me, standing by me patiently while bringing up our two precious daughters Wafa and Yusra – I survived and managed to complete it all because of her.

October 2016

SILICON NANOCRYSTALS AND DEFECT STATES IN SILICON RICH SILICON NITRIDE FOR OPTOELECTRONIC APPLICATIONS

Shakil Mohammed, PhD
The University of Texas at Dallas, 2016

Supervising Professor: Stuart F. Cogan

Research interest in silicon nanocrystals (Si-NC) has increased significantly as a result of the desire to improve the light emission efficiency of bulk silicon. Si-NCs embedded in silicon nitride have desirable characteristics for optoelectronic applications since they can increase the tunneling probability and have a lower tunneling barrier than silicon oxide. Higher tunneling probability is an important feature as it can be used to develop more efficient electroluminescent and photovoltaic devices. In this dissertation, the Si-rich $Si_3N_4$ (SRN) was prepared using low pressure chemical vapor deposition (LPCVD) and RF sputtering followed by high temperature treatment in order to precipitate Si-NCs within the silicon nitride matrix. Several different characterization techniques were used on the Si-NC samples in order to understand the physical, structural, optical and electrical behavior of the nanocrystals. Characterization techniques used in this analysis included photoluminescence (PL), time resolved PL, X-ray diffraction, X-ray photoelectron spectroscopy, Fourier transform infrared spectroscopy, Raman spectroscopy, transmission electron microscopy, ellipsometry and capacitance-voltage (C-V) measurements. Silicon nitride was found to contain a high defect density which suppressed the PL effect from the Si-NC. The

PL observed from each different SRN sample correlated to defect states, namely dangling bonds and oxygen related bonding. Although substantial evidence suggested that Si-NC had formed within the SRN sample, a PL effect due to the quantum confinement effect (QCE) from the nanocrystals could not be detected. However, Si-rich $SiO_x$ samples exhibited excellent PL which correlated with the QCE for an indirect bandgap semiconductor. Further experiments were conducted using forming gas in order to passivate the defects in the SRN. Though significant changes in PL was not achieved due to passivation, the electrical behavior from the SRN indicated that the intrinsically charged defects may have been passivated.

TABLE OF CONTENTS

LIST OF FIGURES

# LIST OF TABLES

# CHAPTER 1

# INTRODUCTION

## 1.1 Motivation

Since the establishment of the semiconductor industry, silicon has played a major role as a semiconductor material in thin film fabrication and development of devices for microelectronic, optoelectronic, and biomedical applications. As a result, silicon related processing and its production in mass have been developed with precision and reduced defects. The extensive research on silicon and its related devices has enabled the scientific community to understand and explain its physical, electrical and chemical properties. In semiconductor physics, silicon's characteristics are used as a base to explain the behavior of other materials. Silicon also forms a natural oxide $SiO_2$, which has been found to function as an excellent insulator and diffusion barrier to impurities.

In optoelectronics, there has been a growing interest in using silicon as a viable material since it is easily integrated with existing complementary metal oxide semiconductor (CMOS) technology. However, the challenge imposed with silicon in this regard is that it has an indirect bandgap and cannot emit visible light with high efficiency, as opposed to its direct bandgap counterparts such as GaAs, InP or GaP. Hence, Si could not be suitably integrated into micro-photonics or optoelectronics devices. Light emission by free carrier recombination is highly unlikely in an indirect bandgap, and in the case of bulk silicon, most of the emitted spectrum is observed in the near infrared region since its bandgap is only 1.1 eV. Therefore, the realization of a device capable of emitting light in the visible spectra (400 to 800 nm) using bulk silicon has not been possible yet. The challenges imposed by silicon's inefficient behavior related to

optoelectronic devices has opened up the possibility of researching methods to improve the light efficiency of silicon and thereby develop new photonic and optoelectronic devices. Some of the previously investigated approaches to improving silicon's light emitting efficiency have been discussed by Yuan *et al.* [1] and include Brillouin zone folding and band structure engineering of silicon with other Group IV materials [2], radiative recombination of carriers at specific type dislocations in silicon [3], [4], incorporation of a direct bandgap compound (e.g. $\beta$-$FeSi_2$) in silicon [5], [6], and implantation of rare-earth ions in silicon that act as luminescence centers [7]–[9].

Canham's discovery of porous silicon in the 1990s brought a major breakthrough after resolving silicon's light efficiency [10]. Porous silicon prepared by electrochemical etching exhibited strong visible photoluminescence (PL) at room temperature. Although the discovery of luminescence from porous silicon laid the foundation for improving silicon's light efficiency, it is still difficult to implement porous silicon because of its fragile mechanical properties and inhomogeneous structure [11]. Furthermore, the quality of porous silicon degrades over time due to its ambient atmosphere, and its integration into device fabrication has been challenging.

Eventually, the scientific community came across several other novel ideas where silicon's light efficiency was improved by introducing silicon nanostructures (amorphous and crystalline) in an insulating material (e.g. $SiO_2$, $Si_3N_4$ or SiC) that followed Canham's original idea and further improved the understanding behind the luminescence from such structures. Over the past two decades, substantial research was performed following the development and understanding of the structural and optical properties that improve the light emission efficiency of silicon.

With that end in view, silicon nanocrystals (Si-NC), also known as silicon quantum dots (Si-QD), were developed [12] in an insulating matrix. The simple processing and optical properties

made Si-NC a suitable material for investigation. Several different aspects of Si-NC embedded in $SiO_2$ matrices have been investigated. However, there has been a growing interest in nanocrystals embedded in silicon nitride ($Si_3N_4$) since it has 1) a lower probability of electron/hole leaking into the matrix from the Si-NC as opposed to SiC and 2) its smaller bandgap over $SiO_2$ offers a higher carrier mobility and better transport between Si-NC, which is essential for light emitting applications. Therefore, the primary focus of this dissertation is Si-NCs embedded in $Si_3N_4$ as a suitable material system for studying the luminescence properties of Si-compatible optoelectronic materials.

## 1.2 Direct and Indirect Bandgap of Semiconductors

The band structure of a semiconductor material consists of a filled valence band and a conduction band that remains empty at absolute zero. The electrons can transfer from the valence to the conduction band via (1) thermal excitation at temperatures higher than absolute zero, (2) absorption of photons, or (3) energy supplied by an applied bias. The negatively charged electron, $e^-$ transfers to the conduction band by leaving a hole $h^+$ in the valence band. Alternately, an electron from a conduction band can transfer to the valence band and recombine with the hole. The electron and hole for their opposite charges are always bound together and hence form a pair termed *the exciton*.

During an excitonic process, momentum and energy are conserved in a direct bandgap material without the mediation of any particle other than the photon. Such processes are termed as radiative recombination/generation. In the case of an indirect bandgap material, such as silicon or germanium, the absorption process requires an additional particle called the phonon for the conservation of momentum. A phonon is a quasiparticle which is associated with the lattice

vibrations in a solid. An electron can only transit from the maximum of the valence band to the minimum of the conduction band when it is accompanied by both the photon and phonon. Such processes are termed non-radiative recombination/generation. The transition and excitation processes in an indirect and direct semiconductor are depicted in Figure 1.1.

## 1.3 Overcoming Silicon's Light Efficiency Limitations

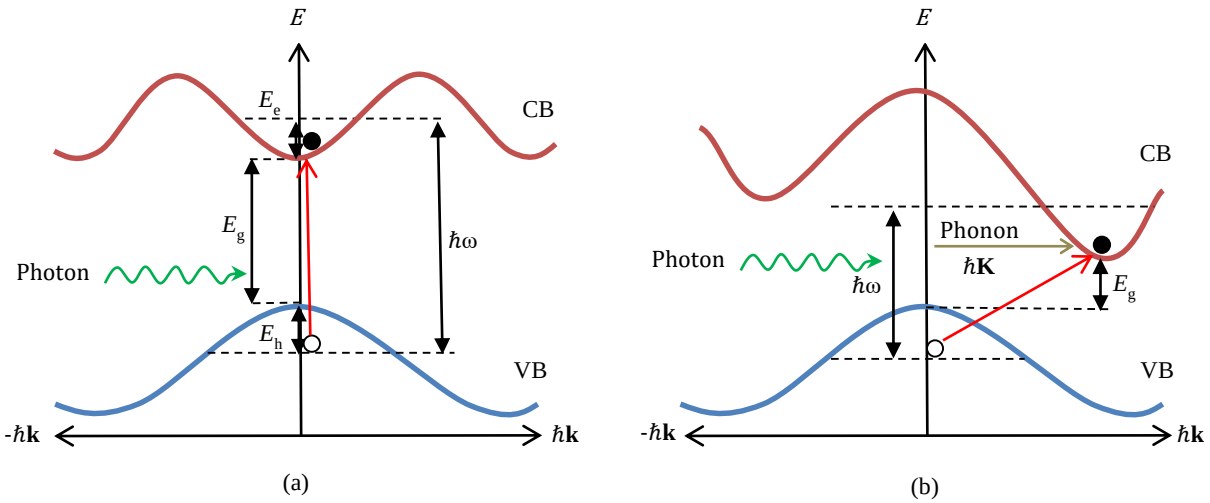


Figure 1.1. In part (a), the energy conservation during the creation of an exciton as the result of photon absorption is shown in a schematic band structure. The sum of the kinetic energies of electron and holes plus the band gap energy is equal to the photon energy. Part (b) shows the transition of an electron from the valence band to the conduction band in an indirect semiconductor. For momentum transition in *k*-space, a phonon as an assistant particle has to be added.

Due to the non-radiative recombination in an indirect bandgap, the quantum efficiency drops down to <0.001% as compared to around 10 – 30% from a direct bandgap material (e.g. GaAs). In bulk silicon, the non-radiative recombination dissipates heat energy and acts as the dominant process after the relaxation of the excited state electrons. As a result, radiative recombination becomes less probable. In general, the lifetime of the non-radiative recombination processes in indirect bandgaps semiconductors are several orders of magnitude faster than the

radiative process. In bulk silicon, the radiative decay times are on the order of microseconds to milliseconds [13] whereas the non-radiative decay times observed are picoseconds to several nanoseconds [14]. Since non-radiative processes are due to phonon mediation, they may occur at a defect or impurity present at the interface or in the bulk of the material. Since the non-radiative processes are always faster than the radiative, the decay associated with non-radiative states will always prevail between the two processes [13]. Therefore, the relative probability of the non-radiative recombination compared to the probability of radiative recombination is large in bulk silicon. This causes extremely inefficient photon emission in bulk silicon, making it less favored over other direct bandgap semiconductors in LEDs and lasers and has ultimately resulted in limiting the advancement of silicon photonic and optoelectronic applications.

Nanocrystalline quantum dots, as mentioned previously, are one of the methods proposed to improve the light emission efficiency in indirect bandgap semiconductors. Typically, the quantum dots are grown inside an insulating matrix by first depositing a silicon rich film and consequently annealing it at high temperatures. In Figure 1.2, the tiny ordered structures in circles are nanocrystalline Si that was precipitated in a $Si_3N_4$ matrix after deposition. Their sizes can range from 1 to 10 nm and may consist of thousands to millions of atoms. The energy band structure of a nanocrystal resembles that of a single atom to a certain extent, and hence they are often called *artificial atoms*.

The behavior of silicon quantum dots can be explained by the simple particle in a box problem described in quantum mechanics. It can be assumed that the electrons in a nanocrystal are confined in a well bounded by an infinite potential (in this case the oxide or the nitride matrix). By solving the Schrödinger's equation for the box, the ground state energy is found to vary inversely

with the square of width of the potential well. At low energies, the energy states are discrete whereas at sufficiently high energy, the energy states are continuous. Due to the confinement of the electron within the potential well (i.e. defined position), the momentum wavefunction is assumed to be spread and therefore have no impact on the transition of the electron. Such an effect is termed the *Quantum Confinement Effect* (*QCE*).

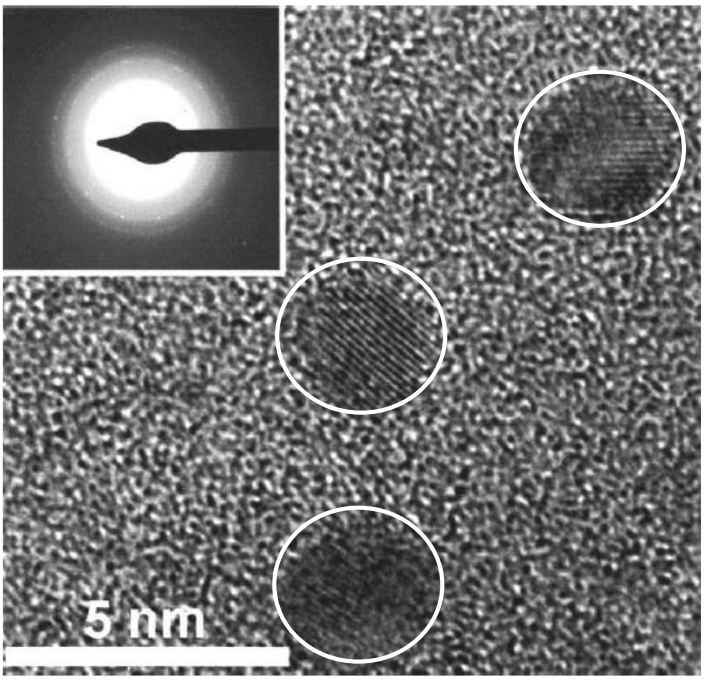


Figure 1.2. HRTEM image of crystalline silicon quantum dots embedded in $Si_3N_4$ grown by PECVD. The inset shows the ring patterns for the transmission electron diffraction from crystalline Si QDs. Reprinted with permission from Ref. [15], Copyright 2006, AIP Publishing LLC.

Confinement raises the energy of the ground state and creates discrete density of states at low energies, causing an uncertainty in the momentum of the particle. According to Heisenberg's uncertainty principle $\Delta x \Delta p \geq \hbar/2$, if the position of an electron is well defined (i.e. electron confined in the potential well), the uncertainty in momentum will increase. Recombination will then occur

as a “pseudo” direct effect without the phonons, which will in turn raise the probability of radiative recombination.

Not all nanocrystals can exhibit the QCE effect. A certain distance must separate the bound electron-hole pair, or exciton, in order to observe the QCE. This phenomenon can be explained by Coulomb attraction, where the electron-hole pair problem is solved by using the hydrogen atom model. The Bohr radius between the electron and hole (which is the critical length separating the two particles) is found to be 4.9 nm for Si. Therefore, in order for Si to function as quantum dots, the nanoclusters must be smaller than 5 nm in diameter.

### 1.4 Radiative vs. Nonradiative Recombination

Silicon nanocrystals that demonstrate quantum confinement effect can exhibit an emission several orders of magnitude brighter than bulk silicon. The radiative quantum efficiency in bulk Si is ~$10^{-6}$ [16] whereas in Si-NC, it is at least five orders of magnitudes higher [17], [18]. The low absorption cross section of silicon (i.e. probability of the photon absorption) in nanocrystals does not play a significant role in enhancing the radiative emission over bulk silicon.

The non-radiative states in bulk silicon are dominated by Shockley-Hall-Read recombination located at the middle of the bandgap which are present due to the defects and impurities in the crystal [19]. Surface defects and Auger recombination also play a crucial role as non-radiative states which reduce the light emission in bulk silicon as well. In Auger recombination, the energy of the exciton is transferred to a third charge carrier. Any of the non-radiative recombination mechanisms mentioned above within the Si-NC are undesirable. A single such non-radiative recombination center present within a luminescent structure consisting of Si-NCs can significantly reduce the light efficiency [20]. Several experiments performed on Si-NCs

have provided information from the non-radiative states only and hence made it difficult to determine the quantum confinement due to radiative processes.

The radiative recombination rate can be improved by confining the carriers in real space. From Heisenberg's uncertainty principle, this will eventually cause a spreading of the wave-functions in momentum space. For an indirect bandgap material like silicon, this is going to increase the probability of radiative recombination rate. However, even with nearly no phonon transition probability observed at liquid helium temperatures [21], [22], the Si-NC with the smallest size ($\leq 2$ nm) will still remain an indirect bandgap material.

## 1.5 Fabrication and Post Processing of Silicon Nanocrystals

Recently, the development of luminescent Si nanostructures has focused on using deposition techniques such as chemical vapor deposition (CVD), physical vapor deposition (PVD), and thermal evaporation among others. A subsequent annealing is often performed in order to precipitate the nanoclusters in an insulating matrix. Nanoclusters prepared by such methods are better suited for device applications due to their improved compatibility with silicon processing technology. The materials deposited using these "dry" methods are stable with better performance than electrochemical depositions.

### 1.5.1 Deposition Techniques

Silicon nanoclusters embedded in a silicon oxide matrix have been prepared using various methods. Some of the widely used techniques are microwave-induced or laser-induced decomposition of silane ($SiH_4$) like precursors [23], low-pressure chemical vapor deposition (LPCVD) [24], ion implantation of $Si^+$ into $SiO_2$ films [25] , co-sputtering of silicon and $SiO_2$ [26],

evaporation of silicon monoxide (SiO) [27], pulsed-laser deposition (PLD) of Si [28], and plasma-enhanced chemical vapor deposition (PECVD) of $SiO_x$ [29]. Some of the techniques offer faster and easier processing, such as plasma enhanced chemical vapor deposition (PECVD). However, the gas precursors used in this technique were found to contain a higher amount of impurities, which degrade the overall performance of the nanocrystals [30]. Another method widely adopted was the deposition of a thin layered structure such as $Si/SiO_2$ and $SiO/SiO_2$ superlattices, where the size of the nanocrystals could be controlled precisely by predefining the thickness of the deposited layer [31]. Although the techniques discussed above mostly involved the synthesis of Si-NC in $SiO_2$, similar techniques and deposition conditions have been adopted after processing Si-NCs in $Si_3N_4$ and SiC as well.

### 1.5.2 Post-deposition Processing of Silicon Nanostructures

One of the important steps after depositing the silicon-rich dielectric thin films is to anneal them at sufficiently high temperatures to induce a precipitation where the metastable thin film decomposes into two stable phases: a silicon nanocluster and a matrix that is close to the stoichiometric composition. In addition, several other post-deposition processing methods, such as oxidation, forming gas and plasma treatment have been used to remove defects in crystals. High temperature annealing is typically carried out in a vacuum or in highly pure $N_2$ or Ar ambient in order to minimize any defect that may be induced from the surrounding environment. Annealing can also influence the size distribution and the density of the nanocrystals.

The as-deposited $SiO_x[SiN_x]$ starts to phase separate out into a Si nanocluster and a more stable $SiO_2[Si_3N_4]$ at temperatures of 400–700 °C through the following equation [27]:

$$SiO_x[SiN_x] \rightarrow \frac{x}{2} SiO_2[Si_3N_4] + \left(1 - \frac{x}{2}\right) Si$$

Nanocrystal formation from silicon-rich thin films after a thermal treatment generally involves two steps: (1) the diffusion and the nucleation of the silicon phase and (2) the subsequent growth of the initially formed crystals by diffusion. The investigation of nanocrystal growth in silicon-rich $SiO_2$ deposited by CVD was described by Nesbit [32] and indicated a diffusion controlled growth given by:

$$D(T) = D_0 \exp\left(-\frac{E_A}{RT}\right)$$

where $E_A$ is the activation energy and $R$ is the universal gas constant. The activation energy of the films was measured to be 1.9 eV/atom and $D_0 = 1.2\times10^{-9}$ cm$^2$/s. A minimum excess of silicon in the silicon rich layer was required to start the initial nanocrystal formation.

Usually, annealing of the $SiO_x$ films is performed at 1100 °C or higher for full crystallization of the silicon phases. However, it was also found that the crystallinity of silicon can also be affected depending on the ratio between the silicon and oxygen. With ratios O/Si<1.0, annealing below 1100 °C would also crystallize the silicon [33]. Films that have a composition of 1<O/Si<1.9 require annealing temperatures of 1050 °C for crystallization. However, Hartstein *et al.* [34] also showed that often temperatures in excess of 1150 °C were needed for complete crystallization of the excess silicon.

High temperature annealing also has drawbacks as it may enhance the dissociation of certain bonds and introduce point defects within the matrix. These defects often have a higher density that may eventually impede the device performance as well as the efficiency of the Si-NCs. Careful consideration of the annealing temperature and ambient environment may reduce the

formation of such defects. Sometimes a post-annealing gas passivation is performed to greatly reduce these newly formed defects.

### 1.5.3 Passivation of Silicon Nanocrystals

As mentioned above, the high temperature anneal can often dissociate the chemical bonds, which will eventually introduce new defects in the form of a dangling bond. These dangling bonds can exist at the interface between the Si/dielectric layer and act as charge trapping centers. Other defects may also exist intrinsically within the dielectric or may get introduced by external impurities. Any such defect is unwanted as they can affect the overall efficiency of the Si nanoclusters. Lannoo *et al*. [35] has shown that the photoluminescence from a nanocrystal can be effectively quenched by a single dangling bond. It has been demonstrated that these defects due to the dangling bonds can be greatly reduced (passivation) by annealing the samples in forming gas (5–10% $H_2$ in $N_2$) at moderately high temperatures [36], [37]. An annealing in forming gas (FG) at ~400 °C for 30 minutes can enhance the luminescence intensity from two to ten times [38], [39]. Wilkinson *et al.* [40] have studied the kinetics of hydrogen passivation of $P_b$ defects for silicon nanocrystals in $SiO_2$ determining that ~500 °C is the optimal temperature for the passivation anneal. Wilkinson also observed that the atomic H, which can be dissociated by a metal cap acting as a catalyst can further improve the PL intensity of the Si-nanocrystals [41].

The forming gas passivation in $Si_3N_4$ based systems has been less researched mainly because $Si_3N_4$ acts as a diffusion barrier to forming gas or any other gases. The diffusion coefficient of FG for an activation energy of $E_A = 2.94 \pm 0.15$ eV into $Si_3N_4$ was ~$10^{-17}$ $cm^2/s$ to $5\times10^{-14}$ $cm^2/s$ when the anneal temperature varied from 700 °C to 1000 °C [42], which is lower than the diffusion of FG in $SiO_2$ annealed at a lower temperature (~$10^{-14}$ $cm^2/s$ at 350 °C).

## 1.6 Applications of Silicon Nanocrystals

Silicon nanocrystals prepared using various techniques are studied for a wide range of applications in the fields of microelectronics and optoelectronics. The investigation of silicon nanocrystal is currently one of the most active frontiers in physics, chemistry, and engineering. Active research has been focused on understanding the behavior of nanocrystals, improving their performances and integrating them with semiconductor devices. A handful of applications with a few relevant examples are discussed below.

### 1.6.1 Light Emission

The most relevant and perhaps most researched use of the Si-NC followed the realization of its efficient luminescence within the visible spectra which makes it an ideal candidate for light emitting applications. The work by Pavesi *et al.* [12] is highly referenced in the field of silicon nanostructures where the authors reported a high optical gain in silicon quantum dots dispersed in a silicon oxide matrix.

There has been a successful demonstration of electrically stimulated light emission (electroluminescence) from silicon nanocrystals where the silicon quantum dots embedded in a nitride matrix were deposited on a doped silicon wafer along with a transparent layer (amorphous silicon carbide and transparent indium-tin-oxide (ITO) electrode [43]). Photoluminescence varied from infrared to blue in those samples without any need for additional annealing.

Recently, it was also demonstrated that quantum confined silicon nanocrystals can be included into organic light-emitting diode (OLED) devices with promising results [44]. The external quantum efficiency in such devices was measured to be 0.6% for the silicon quantum dots.

### 1.6.2 Photovoltaics

Silicon has been widely used as an active layer in photovoltaics for a very long time. However, bulk silicon is capable of harvesting the sun's heat energy. In order to generate energy from the visible spectra of sunlight, Si-NCs whose bandgaps can be tuned precisely are a better option over bulk silicon, as it is possible to integrate them with the existing Si-based solar cells. As a result, multiple junction solar cells, which are solely based on silicon layers with variable optical bandgaps can be fabricated. These solar cells can generate multiple excitons thereby increasing the excitation energy, and also increase the absorption strength of the material.

One of the methods where the Si-NCs were incorporated in photovoltaic devices was by forming Si-NC/$SiO_2$ superlattices. As discussed earlier, the bandgap of the nanocrystal can be suitably tuned inside a superlattice and it can provide good electronic transport properties. Conibeer *et al.* [45] and Cho *et al.* [46] proposed the use of this approach to realize third generation, tandem solar cells where each layer of the device is composed of silicon quantum dots with different sizes and optical bandgaps. This approach overcomes the limitation of a single junction solar cell (Shockley–Queisser limit), with the additional attractive prospect of achieving this with a single material.

### 1.6.3 Microelectronics

Silicon nanocrystals are potential candidates for the development of electronic devices. In microelectronics, the Si-NCs are widely researched for memory applications. Floating gate memories based on Si-NC are promising for developing an ultra-dense and ultralow-power memory. Si-NCs of approximately 2 – 3 nm sizes can be embedded close to the transistor channel

in the gate dielectric to store charges, which can successfully perform better than conventional memory devices with a faster read/write speed, higher reliability and lower power dissipation [47].

With all the advantages of silicon nanocrystals described above, it is evident that Si-NC applications are a very interesting field of research that has plenty of challenges to overcome and further room to grow. With that in mind, scientists are still dedicating their labor to understanding the various phenomenon of these nanocrystals so that Si-NCs can be used effectively in the semiconductor industry in the future without the need to replace silicon with other material.

## 1.7 Silicon Carbide for Biomedical Implants

Amorphous silicon carbide (a-SiC) thin-film dielectric coating has emerged as a promising candidate for the encapsulation of implantable biomedical devices [48]–[51]. It has a lower dissolution rate at 37 °C in phosphate buffered saline (PBS) than silicon nitride [48] and hence can tolerate in the cortex without any degradation over a long period of time. For devices with metal electrodes that are going to be implanted in the brain, it is required that the overall structure of the thin-film device is straight. At the Neural Interfaces Laboratory of UT Dallas, metal electrode arrays (MEA) for neural applications were fabricated on a Si wafer by using a stack of Polyimide-SiC-metal-SiC-polyimide design. The MEAs were released in water and expected that the device is straight. In order for the device to be straight, controlling the stress of the material in the MEA is extremely important. The residual stress of a-SiC was found to be compressive which caused the devices to curl. Therefore, it was essential to understand the root cause of the stress and attempt to reduce the compressive stress to make the devices straight.

The change in residual stress in PECVD a-SiC films exposed to air and wet ambient was investigated. A close correlation between film oxidation and stress change was presented by a

series of mechanical and chemical analyses. It was found that the films deposited at low temperature or power were susceptible to oxidation and underwent significant increase in compressive stress over time. On the other hand, the films deposited at sufficiently high temperature ($\geq 325$ ˚C) and power density ($\geq 0.2$ $Wcm^{-2}$) did not exhibit pronounced oxidation and temporal stress variation. These results served as the foundation for developing a-SiC:H based dielectric coatings for implantable medical devices where thin-film stress management and long-term wet stability are essential.

## 1.8 Organization of the Dissertation

- Chapter 1: The theory and background of the silicon nanocrystals are explored. The advantage of silicon nanocrystals for improving silicon's light emission efficiency and its preparation methods are mentioned. There are challenges to extracting highly intense visible light from such systems due to large defect densities within the films. However, Si-NCs could be used in a wide range of applications in optoelectronics and microelectronics.
- Chapter 2: The experimental techniques are discussed. At first, the deposition techniques that are primarily used (namely LPCVD and sputtering) are briefly explained. The tools used for characterizing the Si-NC, namely photoluminescence (PL), time resolved PL, X-ray diffraction (XRD), X-ray photoelectron spectroscopy (XPS), Fourier transform infrared spectroscopy (FTIR), and Raman spectroscopy are explained briefly.

- Chapter 3: The chapter investigates the PL from the Si-rich silicon nitride films that were prepared by LPCVD and annealed at high temperature. The luminescent PL indicated that it had multiple convoluted peaks which originated from intrinsic defects within the nitride matrix and not Si nanocrystals.
- Chapter 4: The sputter deposition of Si-rich $SiN_x$ (SRN) and $SiO_x$ and their characterization is presented. The reactively sputtered SRN showed that it contained Si-nanocrystals as was evident in TEM, XRD and Raman. However, no PL emission could be detected. $SiO_x$ deposited by co-sputtering technique indeed displayed a very strong PL and a long TRPL, which are characteristics of indirect bandgap Si-NCs.
- Chapter 5: Co-sputter deposition and high temperature annealing of SRN samples are investigated. The SRN exhibiting PL also had substantial evidence of the formation of Si-NCs. However, the PL could not be correlated with the Si-NC, but only with defects identified to be originating from oxygen related and intrinsic states only.
- Chapter 6: On a separate project for biomedical implantable devices, PECVD deposited a-SiC:H films were investigated. For neural implants, SiC serves as an excellent material for coatings that are stable and resistant to corrosion. However, it was observed that a-SiC:H films undergoes change in the residual stress over time, which is undesirable for thin neural interfaces devices. It was found that oxygen and water vapor played a major role in oxidizing the a-SiC:H which results in changes in the residual stress state. eventually caused a change in the residual stress.
- Chapter 7: Conclusions and the scope of future experiments are explored.

# CHAPTER 2

# EXPERIMENTAL TECHNIQUES

## 2.1 Deposition Techniques

### 2.1.1 Sputtering Process

Figure 2.1 (a) is one of the sputtering systems housed in the UT Dallas cleanroom and Figure 2.1 (b) shows the schematic of the system. It is a physical vapor deposition system that was developed for the deposition of metals and insulators by igniting a plasma of an inert gas under a medium vacuum. The inert gas impacts the solid target and removes the atoms which then accelerate towards the target surface. In order for the ejected source atoms to diffuse through the plasma and arrive at the substrate, a vacuum of the order of ~$10^{-3}$ Torr is typically maintained during deposition. However, the chamber is initially evacuated to a pressure of ~$10^{-7}$ Torr prior to loading the samples in order to reduce the impurity content from the surrounding environment. Sputtering can be performed in two different modes, namely DC sputtering and RF sputtering. In DC sputtering, a fixed negative voltage is maintained on the target with respect to the substrate while the chamber is grounded. The inert gas (typically Ar) generates a plasma through impact ionization with high energy electrons. The ionization reaction is expressed as,

$$e^- + Ar \rightarrow Ar^+ + 2e^-$$

The positively charged $Ar^+$ ions get accelerated towards the negatively charged target and eventually dislodge atoms from the target after multiple collisions. DC sputtering is only appropriate for conductive materials such as metals. With insulators, the positively charged $Ar^+$ ions would accumulate on the target thereby reducing the negative charge of the target and

eventually lowering the potential in the chamber, which could shut down the plasma. RF sputtering is an alternative to the DC sputtering method where the applied voltage is cycled at a frequency of 13.56 MHz so that positive charges do not accumulate on the target.

Sputtering can occur both at the target and the source, but the system is configured so that sputtering is focused on the target and does not affect the substrate. Often a magnetron source is used in the sputtering chamber where a permanent magnet is placed behind the target in order to

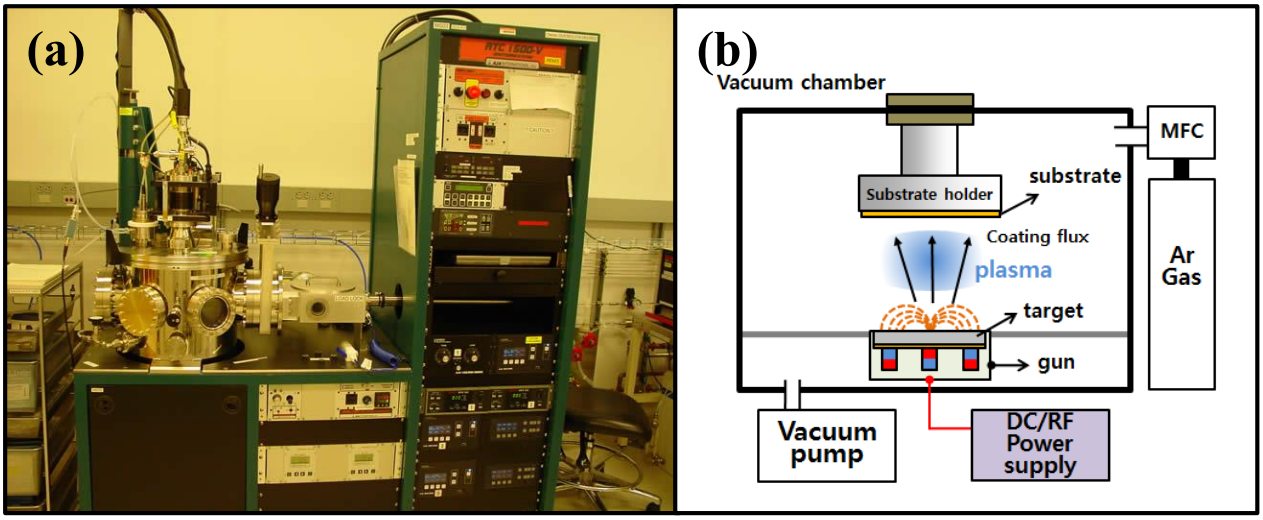


Figure 2.1. (a) The ATC 1500 sputter deposition system, by AJA International in UTD's cleanroom has 2 RF and 2 DC magnetron sources and can be heated in-situ up to 800 °C. (b) A schematic of the sputtering system showing the process of deposition inside the chamber. Reprinted from http://marriott.tistory.com/94.

confine the electrons to a small region near the surface of the target. This significantly increases the percentage of electrons taking part in the ionization process thereby enhancing the efficiency of the sputtering.

In this dissertation, two methods were explored for a compound deposition. The first is reactive sputtering where a target material was allowed to react with a gas in the chamber. The chemical reaction to form the film occurs at the substrate surface. Common gases used in the

sputtering chamber are $O_2$ and $N_2$, which during deposition dissociates first before being incorporated into the growing film. Reactive sputtering can be very difficult to control, especially when a certain concentration of the compound material is required. The second approach towards compound deposition is by using two separate targets to sputter at the same time, a method known as co-sputtering. Co-sputtering can provide better control over desired film stoichiometry as opposed to reactive sputtering since there is no gas dissociation or reactions of concern. We have used this approach to deposit silicon-rich $SiO_2$ (SRO) and silicon-rich $Si_3N_4$ (SRN) films of varying Si content that were suitable for the formation of a nanocrystalline structure.

### 2.1.2 Low-Pressure Chemical Vapor Deposition (LPCVD)

LPCVD is one of the several types of chemical vapor deposition techniques and is mostly used for depositing polysilicon, silicon oxide, and silicon nitride films. The thickness of the deposited material can be precisely monitored in the chamber during LPCVD, and so it can produce films that can vary from 2 nm to 5 μm in thickness. The chamber is typically maintained at a low pressure (~250 mTorr) and high temperatures (600 °C to 900 °C) for the depositions. The deposition in the chamber is achieved through the thermal decomposition of the precursor gases on the wafer. The furnace tubes are made of quartz so that they can withstand high temperatures for a prolonged duration. As seen in Figure 2.2 (b), the furnaces are typically positioned horizontally and the wafers are loaded on a boat so that the gases can directly flow on the surface of the wafer. Multiple wafers can be loaded on a single boat at a time to reduce the overall cost of thermal annealing.

In order to deposit silicon nitride in the LPCVD, the gas precursors used are dichlorosilane (DCS) and ammonia ($NH_3$). The furnace tube is typically maintained at a standby temperature of

400 °C. Prior to loading, the wafers are cleaned so that any impurity from the wafer does not contaminate the chamber. After loading, the temperature of the furnace tube is gradually increased to the set point. The gases at high temperature or low pressure get adsorbed on the surface of the wafer thereby forming a thin layer of silicon nitride. The byproducts generate a volatile gas that is evacuated out of the chamber. After the desired thickness is achieved, the furnace tube is cooled down to the standby temperature condition and then vented. The wafers are cooled down to at least

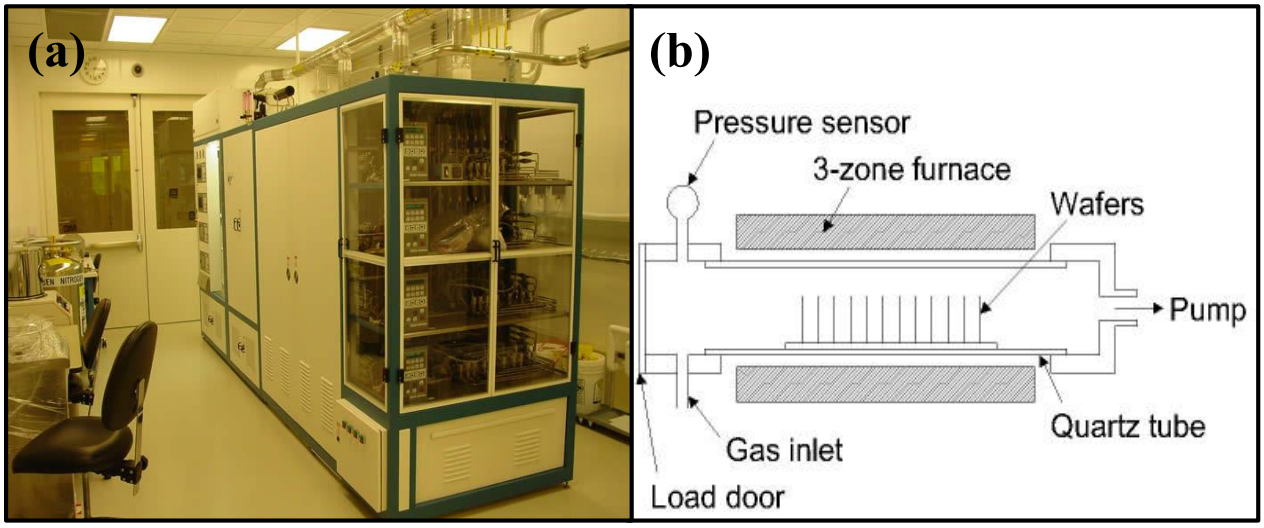


Figure 2.2. (a) The Tystar LPCVD tool at UTD's cleanroom consists of four horizontal sub-atmospheric furnace tubes that can process up to 6" diameter silicon wafers. (b) A schematic of the LPCVD system showing the wafers placed vertically inside a quartz tube. Reprinted from Ref. [52], Copyright 2000, Pearson.

100 °C before they are unloaded.

There are many advantages and disadvantages of using LPCVD. It can reduce autodoping in the wafers due to its low pressure and faster diffusion rates. Unlike PECVD, there is no requirement of a carrier or dilutant gas for the deposition and the gas flow can be lower to reduce the consumption of gases. The disadvantages of LPCVD are that the furnace tube has to be maintained at a very high temperature, which limits the processing of several low melting point

materials. Also, the materials in the chamber get deposited on both sides of the wafer, which adds extra processing step after removing the deposited films before device fabrication.

## 2.2 Materials Characterization

There are a number of tools that can be employed after studying the evolution of the Si-nanocrystals and their respective matrices. Photoluminescence spectroscopy and time-resolved photoluminescence (TRPL) has been an imperative tool for the Si-nanocrystals that could give information on the luminescence due to the confinement of the photons. With the help of X-ray diffraction (XRD), the crystalline structure of the nanocrystals and their sizes can be estimated. X-ray photoelectron spectroscopy (XPS) can probe the concentration of different bonds and provide information on the binding and oxidation of the elements. Although Fourier transform infrared (FTIR) spectroscopy cannot directly probe Si-nanocrystals, it is still very useful in extracting information concerning the different vibrational modes of the bonds present in the host matrix in relation to the variation of the temperature or other parameters. Raman spectroscopy has been found to be effective in determining the composition of the films as well as estimating the phase separation, size and stress induced on the films. And lastly, TEM is used to image the nanocrystals to have a ‘look’ at the structural formation of Si-NCs in the host matrix. A detailed description of the fundamental and working principles of the tools used for the purpose of Si-NCs is presented in the following pages.

### 2.2.1 Photoluminescence (PL) Spectroscopy

Photoluminescence spectroscopy is used to determine the bandgap of a semiconductor or quantum dot or the recombination mechanisms associated with the material that could be due to a

defect or confinement. It is also used to probe interface states and impurities, and other optical properties of QD [53]. PL spectroscopy is a contactless simple and versatile method that does not require any prior sample preparation and does not damage the sample. In PL, the samples are excited by a monochromatic light source and the emitted spectra due to excitation are detected. A high intensity light source (typically a laser) and a highly sensitive detector are often used in order to detect low efficient light. PL discussed in this dissertation is focused on amorphous/nanocrystalline silicon quantum dots in silicon nitrides and oxides, and includes the PL mechanisms caused by radiative defects in the film, interface states, variation in Si cluster size, and quantum confinement effect (QCE).

As discussed in the previous chapter, the external influence (in this case energy supplied by the laser) can create an *e*-*h* pair that emits a photon via radiative recombination. Sometimes the electron or hole can transit into a defect state via non-radiative recombination and eventually undergo a radiative recombination.

The PL spectroscopy is not always conclusive after explaining the radiative or non-radiative recombination. Therefore, the time-resolved PL spectroscopy in conjunction with the PL is often studied, where a very short light pulse is used to excite a sample. The emitted spectra in TRPL is recorded as a function of time and the intensity decays exponentially. The decay spectra can be obtained using an ultrafast pulsed laser as the excitation source. The decay spectrum gives direct information about the carrier relaxation and recombination mechanisms and allows measurement of the radiative lifetimes. The decay of the PL intensity is expressed in terms of an exponential function as [54]:

$$I(t) = I_0 \exp\left[-\left(\frac{t}{\tau}\right)\right]^{\beta}$$

where $\tau$ is the average lifetime and $\beta$ is the dispersion factor.

A schematic of the PL instrumentation is shown in Figure 2.3. The setup consists of a monochromatic excitation light source (e.g. lasers), a collimating system to collect the luminescence signal, a high pass wavelength filter, a spectrometer and a detector (liquid nitrogen

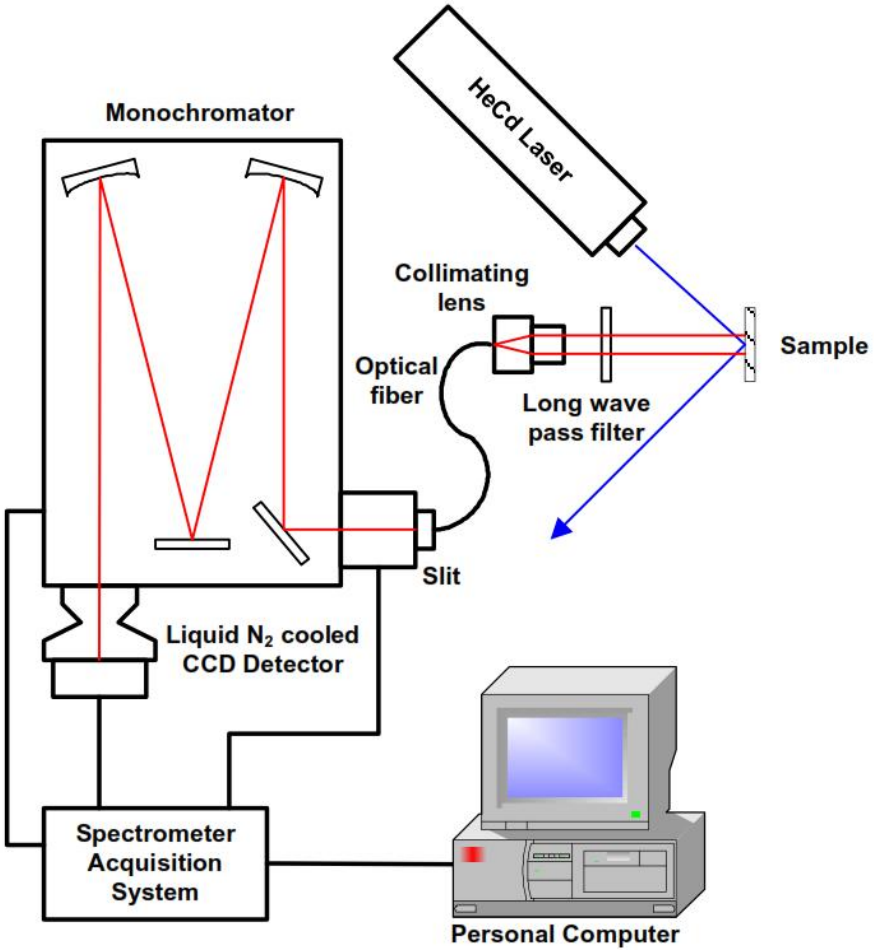


Figure 2.3. Schematic diagram of a photoluminescence system. The sample is excited using a laser light. The reflected signal from the laser is blocked using a long wave pass filter and the luminescence signal is passed through and eventually collected by a collimating system. The signal collected is then recorded by a spectrometer and detector. Reprinted from Ref. [55], Copyright 2005, L'École Polytechnique.

cooled charged coupled device camera). In order to measure the low temperature dependence of PL spectra, a cryostat or another temperature controllable sample holder is used for housing the samples [55].

### 2.2.2 X-ray Diffraction (XRD)

X-ray diffraction is an effective method for determining the crystal structure and orientation of materials. XRD employs the basic principle of elastic scattering of X-rays by electrons of atoms. W. L. Bragg [56] discovered that the diffracting plane is a lattice plane and hence developed the theory which is termed Bragg's law:

$$n\lambda = 2d \sin\theta$$

where $n$ is an integer representing the orders of the diffraction, $\lambda$ is the wavelength of the X-ray, $\theta$ is the half of the deviation of the diffracted beam, and $d$ is the interplanar spacing for a plane that is given by,

$$d = \frac{a}{\sqrt{h^2 + k^2 + l^2}}$$

where $a$ is the constant spacing between the atoms and $h$, $k$ and $l$ are the corresponding Miller indices.

The basic principle of the XRD is to shine X-rays on the specimen and detect the diffracted X-rays from the specimen which is recorded as the diffraction intensity versus the diffraction angle ($2\theta$). Figure 2.4 demonstrates the geometrical arrangement of an X-ray source, specimen, and detector. The X-ray tube typically consists of a Cu source that generates $K\alpha$ lines at 0.1542 nm as the strongest X-ray line. The X-ray generated from the tube passes through the Soller slits, which collimate the beam. A divergent beam passing through the slits strikes the specimen, which is

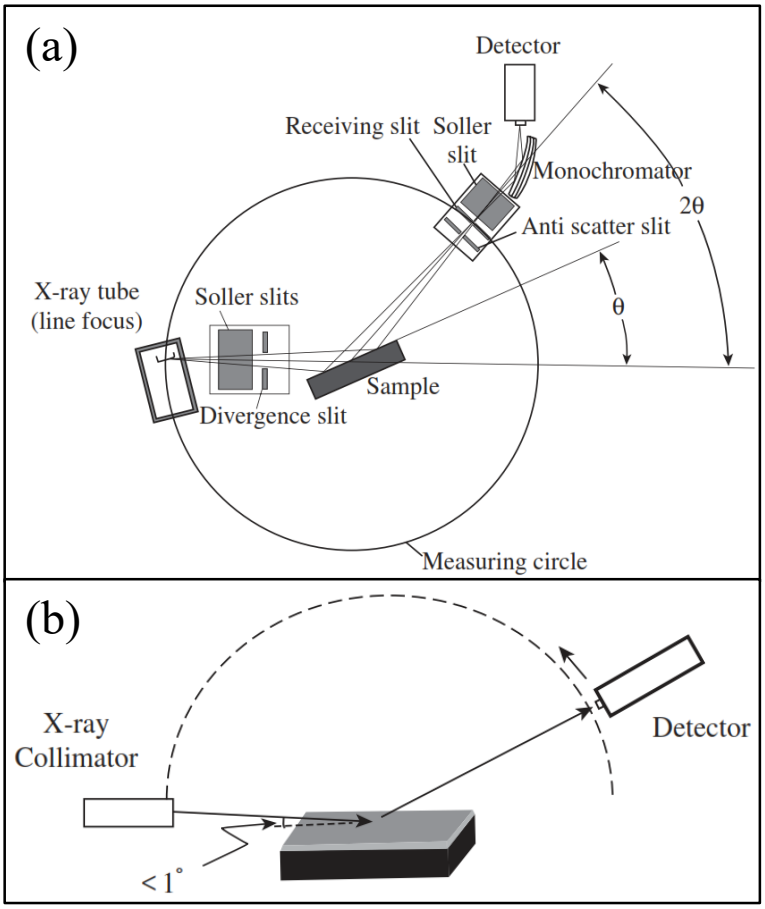


Figure 2.4. (a) Geometrical arrangement of X-ray diffractiometry. (b) Optical arrangement of thin film diffractiometry. Reprinted with permission from Ref. [57], Copyright 2008, John Wiley and Sons.

supported on a specimen table. The X-ray gets diffracted by the specimen and forms a convergent beam at the receiving slits before they enter a detector. It is then sent through a monochromatic filter and then collected by the detector [57].

For a thin-film specimen, a grazing incidence angle X-ray technique is more beneficial as this method collects the information mostly from the film surface but not from the substrate. The angle of incidence in such measurement is typically kept at <1° and it is kept fixed throughout the operation while the detector rotates to obtain the diffraction signal as illustrated in Figure 2.4 (b).

XRD has also been useful in approximating the crystal size of the sample. XRD can be especially helpful in understanding the size of silicon nanocrystals by correlating the XRD peaks with other techniques such as the transmission electron microscope (TEM). The nanocrystal's size can be estimated by using the simple formula by Scherer [58], which is given as follows:

$$L = \frac{\chi\lambda}{\beta \cos\theta}$$

where $\chi$ is the Scherrer constant which is equal to 0.94. $\theta$ is the Bragg angle, and $\lambda$ is the wavelength of the X-ray. Using the Scherrer formula, it is convenient to calculate the mean dimension of the nanocrystals.

XRD is also limited, as it cannot detect crystallites in an amorphous structure if the concentration of crystals is less than 2% [59].

### 2.2.3 X-ray Photoelectron Spectroscopy (XPS)

X-ray photoelectron spectroscopy (XPS) is a surface sensitive technique (depth < 10 nm) which is employed to identify chemical species and their chemical states. XPS is also used to characterize the concentration of particular elements in a compound material. It is utilized after analyzing the distribution of the materials and studying the uniformity of elements under observation.

XPS uses X-rays of a characteristics energy to emit electrons from the core level orbitals in atoms, otherwise known as photoelectrons. These photoelectrons are collimated and collected as a function of their kinetic energy (or binding energy), and the number of photoelectrons collected is plotted as the intensity versus the kinetic or binding energy. The binding energy of the photoelectron ($E_B$) is related to the kinetic energy ($E_K$) by the following equation:

$$E_B = h\nu - E_K - \Phi$$

Where $h\nu$ is the incident X-ray photon that has sufficient energy to knock out an inner shell electron and Φ is the parameter representing the energy required for an electron to escape from the

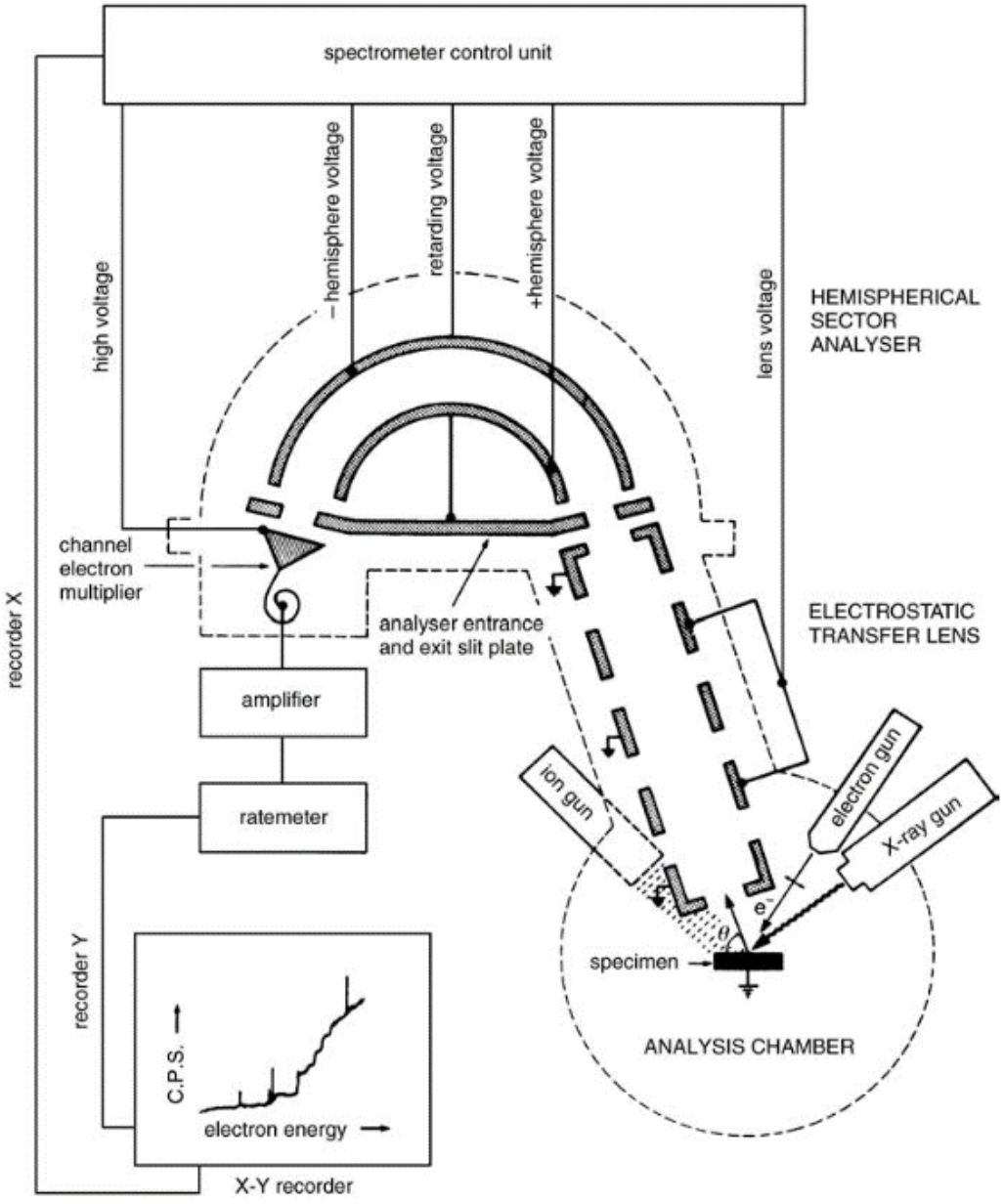


Figure 2.5. Structure of an X-ray photoelectron spectrometer. Reprinted with permission from Ref. [57], Copyright 2008, John Wiley and Sons.

material's surface, which depends on the sample material and spectrometer. The binding energy ($E_B$) of atomic electrons have characteristic values, and these values are used to identify elements.

An XPS spectrometer schematic is shown in Figure 2.5. The X-ray source is usually an Al- or Mg-coated anode struck by electrons generated at a high voltage (10–15 kV) source. Al *K*α or Mg *K*α radiation lines are produced at energies of 1486.7 eV and 1256.6 eV, respectively, with resolutions of about 1 eV. The X-rays typically cover a large area of the sample (~1 $cm^2$). Depending on the size of the sample holder, samples as small as 1 $cm^2$ up to 8-inch wafers can be introduced into the chamber for analysis. Commonly used XPS systems can reach ultrahigh vacuum pressures on the order of ~$10^{-9}$ Torr [57].

Insulating samples such as dielectrics may charge under the X-ray beam, which can result in a shift of the $E_B$ and broadening of the spectra, giving inaccurate information. The problem is usually resolved by the use of a neutralizer, which is a low-energy electron flood gun. Since the surface of an insulator becomes positively charged after electrons are devoid, the electron flood gun neutralizes the positive ions and reduces the charging effect.

The electrostatic transfer lenses are used to retard the electrons before they enter the analyzer in order to improve the energy resolution. There are different types of analyzers used in XPS. The hemispherical sector analyzer (HSA) consists of two concentric hemispheres with a positive and a negative voltage applied between them. By varying the voltage on both the transfer lenses and the analyzer, the trajectories of the photoelectrons with different energies are varied so that they are focused at the analyzer exit slit. The electrons get amplified at the exit slit by $10^5$–$10^6$ when passing through a channeltron type multiplier and they are eventually fed into an external conventional pulse counting electronics and then to the computer.

In many applications, the sample under analysis could develop a thick contaminant layer due to air exposure that could cover up the surface of interest. Such problems are resolved by utilizing argon ion sputtering, which is done inside the spectrometer while collecting data. In order to avoid artifacts that could worsen the surface structure, the sputtering is usually performed at a low power setting for a shorter time.

### 2.2.4 Fourier Transform Infrared (FTIR) Spectroscopy

Fourier transform infrared (FTIR) spectroscopy is a widely used vibrational spectroscopic technique, in which the Fourier transform method is used to obtain an infrared spectrum in a whole range of wavenumbers simultaneously. The key component in the FTIR system is the Michelson interferometer, as schematically illustrated in Figure 2.6 (a). The interferometer divides the incoming light into two beams through the beam splitter, which after passing through a moving mirror causes an optical path difference, and eventually recombine on a detector to produce interference fringes as a function of optical path difference.

The instrument consists of three basic components: an infrared light source, a beam splitter, and a detector. Additionally, it employs *attenuated total reflection* (ATR) which is an accessory of the IR spectrometers that is used to enhance the surface sensitivity from the materials. ATR refers to a particular type of reflection geometry where the infrared beam is reflected internally through a crystal. The beam is oriented to reflect multiple times within the crystal at an angle that causes total internal reflection. Above each point of reflection, an evanescent wave exits which is then used to characterize the substance under consideration. Figure 2.6 (b) shows a schematic of an ATR setup. Using the ATR setup, any information from the vibrational states from a liquid or solid can be extracted. The ATR crystal is made of a high index of refraction crystal which absorbs

minimum light from the region of interest. Typical materials as ATR crystals include silicon, germanium, zinc selenide, and diamond.

Two types of IR-detectors are commonly used: a thermal detector consisting of a pyroelectric crystal made of *deuterated triglycine sulfate* (DTGS) and a semiconductor detector which is made of *mercury cadmium telluride* (MCT). In a DTGS detector, the infrared radiation causes a temperature change which eventually changes the dielectric constant of the crystal. The capacitance is related to the dielectric constant and hence a voltage change across the DTGS is detected. The DTGS detector can detect wavenumbers in the range 4000–400 $cm^{-1}$. It is simple

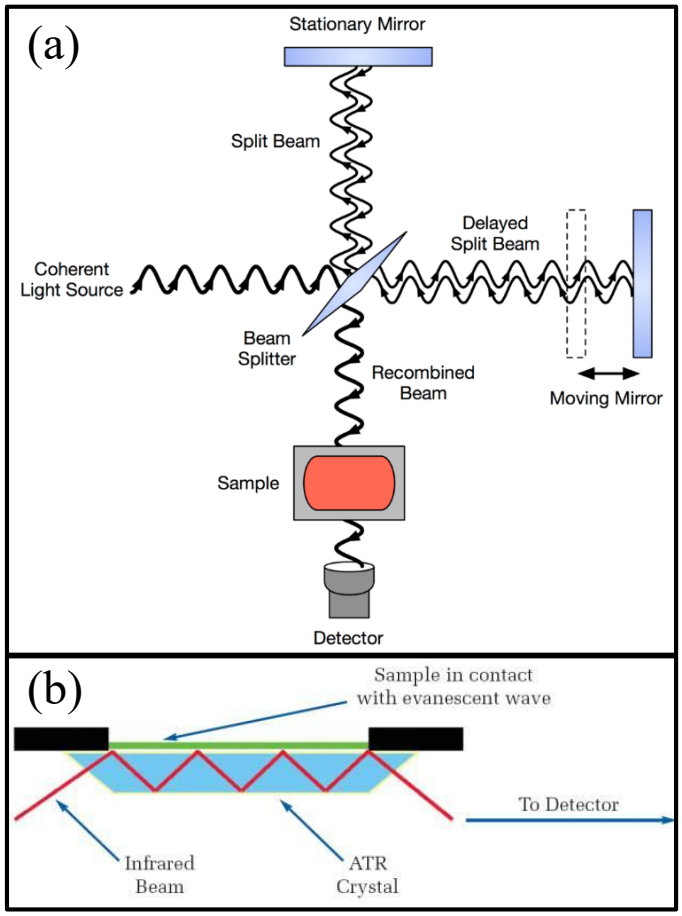


Figure 2.6. (a) Optical diagram of a Michelson interferometer in FTIR. (b) Sample in contact with the ATR crystal attachment. Reprinted from wikipedia.org-FTIR and https://shop.perkinelmer.com/content/TechnicalInfo/TCH_FTIRATR.pdf.

and inexpensive yet less sensitive than the MCT detector. An MCT detector absorbs infrared photons, which causes the electrons in the semiconductor bandgap to transfer from the valence to the conduction band. This results in the generation of an electric current. The MCT detector is up to ten times more sensitive than the DTGS type; but it is only limited to detecting radiation in the band 4000–700 $cm^{-1}$. The MCT detector is initially cooled down to liquid nitrogen temperature (−196 °C) before collecting the spectra [57].

### 2.2.5 Raman Spectroscopy

When monochromatic light of wavenumber $\nu_0$ is incident on a material, it undergoes elastic and inelastic scattering. The elastic scattering is termed as Rayleigh scattering whereas the inelastic scattering is known as the Raman scattering. In Raman scattering, the frequency spectrum of scattered light undergoes a change to $\nu_0 \pm \nu_M$, where $\nu_M$ is a vibrational frequency of the molecule under investigation/consideration. Raman effect is caused by the interaction of optical and vibrational oscillations and results in a change in vibrational energy of a molecule. A phonon is either created (Stokes process) or annihilated (anti-Stokes process) during the Raman scattering [60].

Inelastic scattering can be mediated by many different types of elementary excitations in the matter. In Raman scattering, only phonon mediated processes are considered, which correspond to the energy difference in the vibrational and rotational energy levels. There are several similarities between Raman and infrared spectra, although they have differences in the selection rules and relative band intensities. In order for a molecular vibration to be Raman active, a change in the induced dipole momentum is required which results in a change in the polarizability of the molecule [61]. As long as a change in the polarizability is concerned or there is an induced

dipole moment due to vibrations or rotations, the molecule will always be Raman active despite lacking a permanent dipole.

Raman microscopes can examine samples by focusing down on an area of 1 $\mu m^2$. It does not require any sample preparation and the sample collection can be quick and contactless. A typical Raman microscope (shown in Figure 2.7) consists of the following instruments: laser

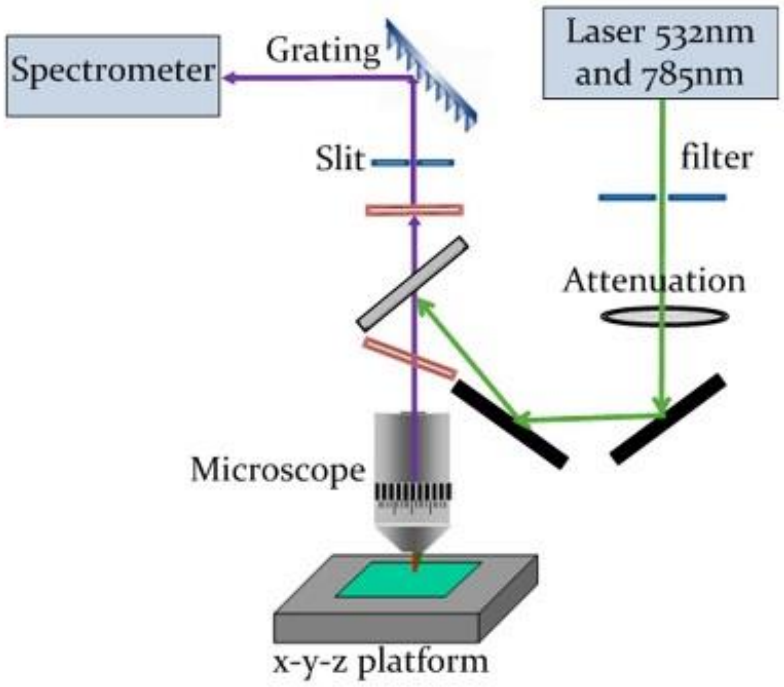


Figure 2.7. A schematic of a Raman microscope system that has two laser wavelengths available at 532 nm and 785 nm. Reprinted from Ref. [62], DOI: 10.7717/peerj.436/fig-1.

source, sample illumination and collection system, spectral analyzer, detection, computer control, and processing system. The laser source emits highly monochromatic light in the visible spectrum. After being scattered from the microscope, the light passes through special filters before reaching the spectral analyzer. Once the light enters the spectral analyzer, it gets dispersed according to its wavenumbers due to the diffraction grating. The scattered light is separated according to

wavelength and is recorded by a CCD detector. The shifts are calculated and plotted versus wavenumber in the Raman spectrum [57].

# CHAPTER 3

# CHEMICAL BONDING AND DEFECT STATES IN LPCVD GROWN SILICON-RICH $Si_3N_4$ FOR QUANTUM DOT APPLICATIONS

Authors – Shakil Mohammed,[1] Mike Nimmo,[2] Anton V. Malko,[2] Christopher L. Hinkle[1]

[1] Department of Materials Science and Engineering, The University of Texas at Dallas, 800 W. Campbell Rd., Richardson, TX 75080

[2] Department of Physics, The University of Texas at Dallas, 800 W. Campbell Rd., Richardson, TX 75080

Reprinted with permission from *Journal of Vacuum Science & Technology A*, **32**, 021507 (2014),

**Participation**

All experiments and data analysis had been performed by myself, with the exception of the photoluminescence and time resolved photoluminescence spectra which were collected by Mr. Mike Nimmo from Dr. Anton Malko's group.

## 3.1 Introduction

The discovery of luminescence from porous silicon [10] in addition to studies on the formation of silicon quantum dots (QDs) [29], [63], [64] has opened the door to vast opportunities for Si CMOS-compatible optical [65], electro-optical [45], and memristive applications [66]. The precipitation of Si-QDs from Si-rich host matrices has been demonstrated as a means of achieving luminescence for these applications. Numerous methods for the deposition of Si-rich films have been utilized including pulsed laser ablation [67], magnetron sputtering [68], plasma enhanced chemical vapor deposition (PECVD) [69], and low pressure chemical vapor deposition (LPCVD) [70]. The choice of host matrix plays an important role in the efficiency of these devices. Silicon nitride has a lower tunneling barrier than silicon oxide allowing an increase in the electron tunneling probability and more efficient transport of charge carriers than silicon oxide, making it more suitable as a host matrix for electroluminescent and photovoltaic devices [71]. Its resistance to impurity diffusion and moisture absorbance has made it an ideal material in semiconductor processing [52]. However, the defect density within the bulk and at the interface is significantly higher than its oxide counterpart [72], [73]. Additionally, Si dangling bonds (DB) increase proportionately as the film becomes more Si-rich [74].

Previous reports of silicon-rich nitrides and oxides [75] indicate that both quantum dots (QDs) and defect state effects can greatly impact the luminescence of these materials. Wang *et al*.

[76] reported luminescence due to quantum confinement in annealed SRN samples due to Si nanoclusters when excited with a 514.5 nm laser and defect states due to Si and N dangling bonds were observed under 325 nm excitation. Hao *et al.* [77] showed that the red emission in their PL was due to quantum confinement whereas the green and blue emission was attributed to band tail recombination and Si-related defects. Kistner *et al*. [78] reported strong PL emission arising only from band tail recombination, not QDs, in SRN samples prepared by PECVD and annealed at high temperature. Other studies have demonstrated strong PL from defect states present within the silicon nitride [79]–[81].

While numerous studies have been conducted on these Si-QD systems, [12], [15], [82] there are still many issues that need to be addressed in order to explain the chemical state evolution, charge transport, and luminescence mechanisms arising from the defect states and/or the Si-QDs. Therefore, the primary focus of this chapter is to correlate the chemical bonding and luminescence properties of the SRN thin films upon deposition and high temperature anneals and to describe this correlation in light of detected defect states.

## 3.2 Experimental

The SRN films were deposited on n-type Si(100) wafers (doping density ~$10^{17}$ $cm^{-3}$) which were first cleaned in RCA followed by dilute HF (100:1) etching for one minute to remove the native oxides. The deposition was performed in a Tystar LPCVD furnace with a constant gas flow ratio of $SiH_2Cl_2$:$NH_3$ of 6:1 in order to achieve the SRN films (stoichiometric $Si_3N_4$ uses a gas flow ratio of 1:3). The samples were deposited at 835 °C (standard temperature for stoichiometric $Si_3N_4$ deposition) and 730 °C (lowest temperature used in the furnace for nitride deposition), and

hence labeled hereafter as T835 and T730 respectively. The samples after deposition were cleaved and separate pieces of the same deposition were furnace annealed for 30 minutes at 800 °C, 900 °C, and 1000 °C in $N_2$ (99.9998%) ambient, respectively.

The room temperature photoluminescence (PL) and time resolved PL decay measurements were carried out using a Ti:sapphire laser, which was excited with 120 fs pulses at 405 nm at a repetition rate of 7.6 MHz and a power of 71 μW. Fourier transform infrared (FTIR) spectroscopy was performed using a ThermoElectron Nicolet 4700 spectrometer with Ge attenuated total reflectance (ATR) setup to probe the various vibrational bonding structures within the SRN thin film. A mercury cadmium telluride (MCT-A) detector was used to collect the FTIR spectra. X-ray photoelectron spectroscopy (XPS) was performed using a PHI 5800 spectrometer equipped with an Al *K*α monochromated X-ray source ($h\nu$ = 1486.7 eV) and the spectra were collected both for the surface and bulk (2 keV Ar-ion sputtering was performed for 5 minutes to probe inside the bulk of the deposited films). The thickness and optical properties of the films were investigated using a UVISEL phase modulated spectroscopic ellipsometer (HORIBA Scientific). The data was measured at an incidence angle of 70° over a range of 1.5 to 5.9 eV. A Nicolet Almega XR Dispersive Raman spectrometer was excited at 532 nm at room temperature to measure the chemical structure of the SRN and any QD precipitates that may have formed during anneal. A Rigaku Ultima III X-ray diffractometer (XRD) configured for grazing incidence angle was used to probe the crystal structure of the films. Finally, high-resolution transmission electron microscopy (HRTEM) images were obtained from a 200 kV field emission JEOL 2100F instrument.

Similarly processed SRN films with a thickness of 50 nm were used as the gate dielectric for metal-insulator semiconductor capacitors (MISCAP) to investigate the charge trapping due to the detected defect states. Aluminum was used as the gate metal and back contact for the MISCAPs. The capacitance-voltage (C-V) measurements were carried out at room temperature on a Cascade probe station using an HP4284 LCR meter.

### 3.3 Results

Figure 3.1 shows the photoluminescence spectra of the as deposited and 1000 °C annealed samples of T730 and T835. Both samples exhibited strong PL emission in the visible spectral region with a maximum intensity at ~645 nm (T730) and ~680 nm (T835). However, the broad peak clearly has multiple peaks convoluted together. A detailed, self-consistent, simultaneous fit was performed that indicated seven distinct peaks convoluted within the broad envelope. The corresponding energies and Gaussian widths of the individual peaks are listed in Table 3.1. The peaks are assigned as P1 to P7 in increasing wavelength (decreasing energy). The relative changes in the PL peak intensities observed from T730 to T835 could be from either 1) changes in QD size or 2) a compositional-dependent change in the concentration of defect states within the nitride. We will now provide evidence that it is the latter of these two explanations and elucidate the chemical nature of these defects.

Table 3.1. Deconvoluted peak positions and Gaussian widths for T730 and T835 PL spectra.

| | **P1** | **P2** | **P3** | **P4** | **P5** | **P6** | **P7** |
|---|---|---|---|---|---|---|---|
| **PL peak wavelength (nm)** | 538 | 594 | 641 | 687 | 725 | 746 | 764 |
| **PL peak energy (eV)** | 2.30 | 2.09 | 1.94 | 1.81 | 1.71 | 1.66 | 1.62 |
| **Gaussian width (nm)** | 65.05 | 61.15 | 62.13 | 58.38 | 47.84 | 16.61 | 32.96 |

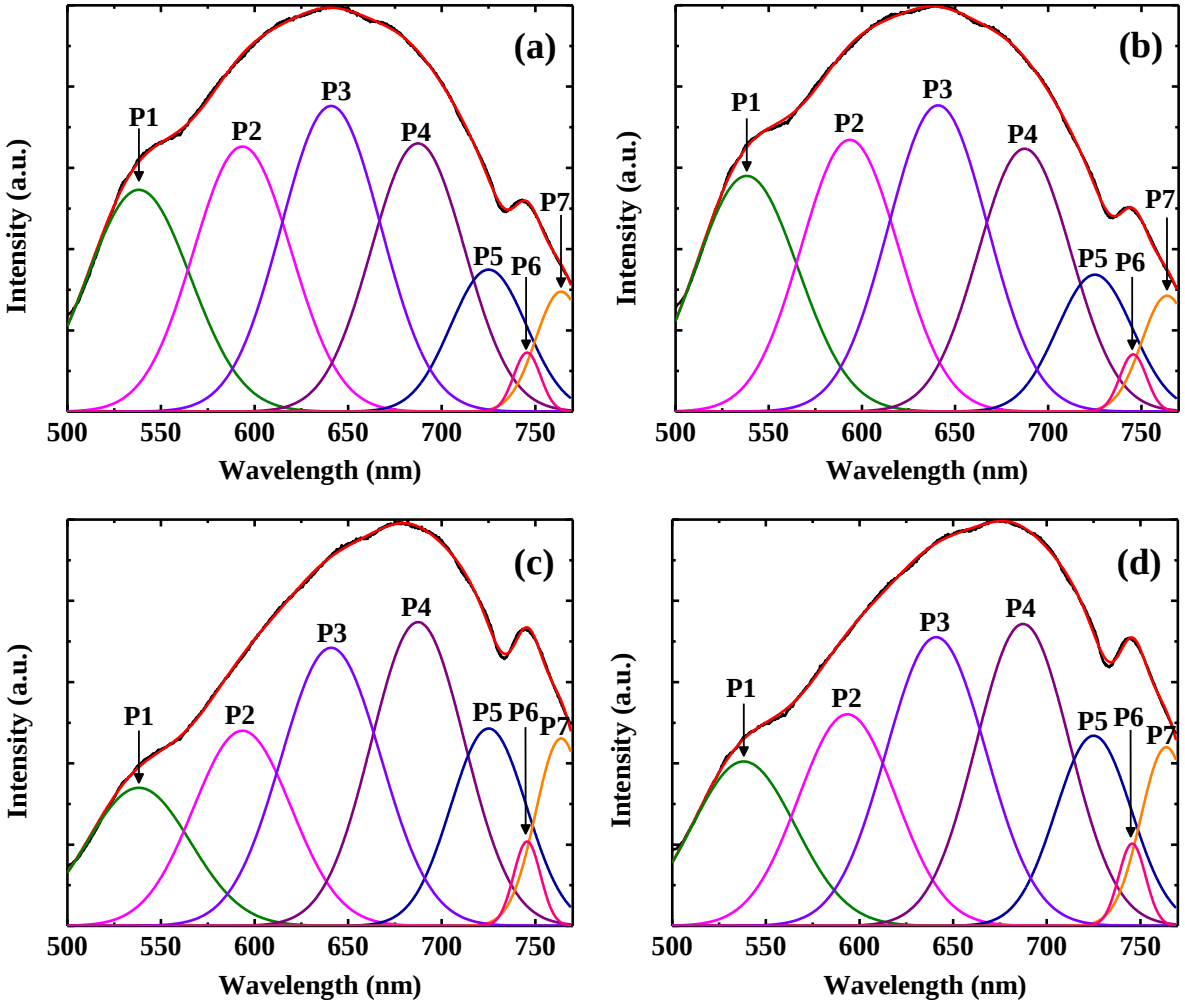


Figure 3.1. PL measurements on (a) sample T730, as deposited, (b) sample T730, annealed in $N_2$ at 1000 °C, (c) sample T835, as deposited, and (d) sample T835 annealed in $N_2$ at 1000 °C. The self-consistent, simultaneous peak fits show that there are seven distinct peaks convoluted together within the broad envelope.

The time resolved PL spectra in Figure 3.2 were measured at room temperature at the highest peak intensities for each sample (i.e., 645 nm for the T730 samples and 680 nm for T835) and were fitted using a double-exponential function:

$$I(t) = I_1 \exp\left(-\frac{t}{\tau_1}\right) + I_2 \exp\left(-\frac{t}{\tau_2}\right)$$

The extracted time constants $\tau$ and their respective amplitudes $I_1$ and $I_2$ are listed in Table 3.2. In all samples, the time constant $\tau_1$ was found to be in the sub-nanosecond range whereas $\tau_2$ was on the order of a few nanoseconds (less than 10 ns). The time signature for a quantum confined state is usually found to be a stretched exponential function with time constants ranging between tens to hundreds of microseconds [84] and they vary depending on the size of the QD [85]. There are reports that Si-QDs can have carrier lifetimes in nanoseconds both in an oxide and nitride host matrix [86]. However, decay constants corresponding to tens of nanoseconds in Si-rich oxides (SRO) were also attributed to radiative defects [87], with such PL emissions reported in the 410-460 nm region. Since the time decay constants in our samples are very short, it is likely that the PL peaks arise from non-radiative trapping and recombination on surface states or at defect states within the Si-nitride, not QDs [83]. The extracted decay constants do not show any noticeable change for samples annealed at higher temperatures, indicating that the higher anneals had little to no impact on the dynamics of the defect states.

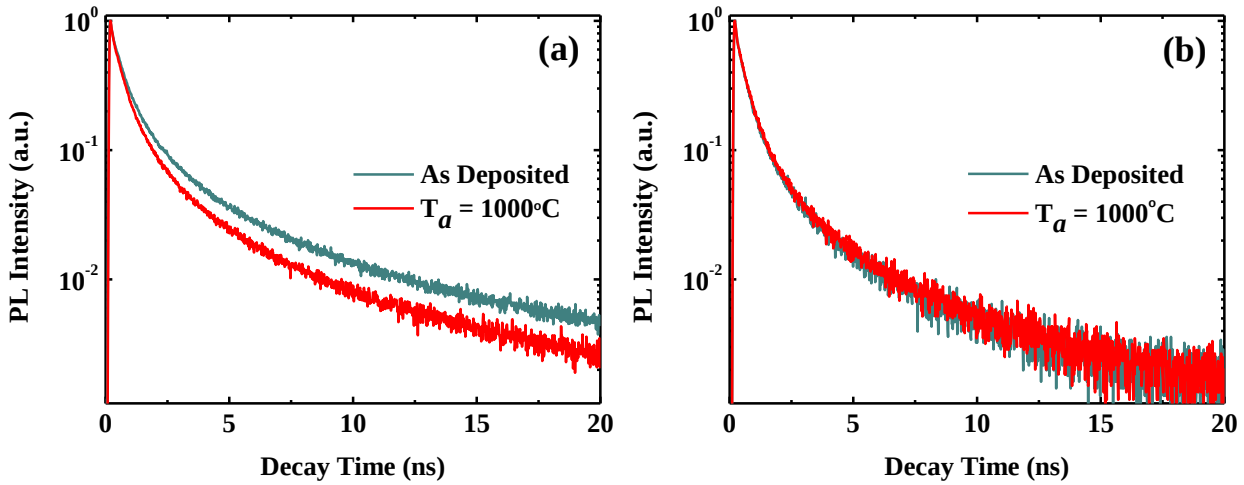


Figure 3.2. The kinetics of PL time decay for (a) T730 and (b) T835. The time decay can be fitted using a double exponential function with one time constant in the sub-nanosecond range and the second time constant in the few nanoseconds range. These time constants are indicative of non-radiative trapping and recombination on surface states or at defect states within the Si-nitride, not quantum confinement (Ref. [83])

Table 3.2. The decay constants and their respective amplitudes measured from the time resolved PL spectra.

| Sample | | $\tau_1$ (ns) | Amplitude, $I_1$ | $\tau_2$ (ns) | Amplitude, $I_2$ |
|---|---|---|---|---|---|
| **T730** | As dep. | 0.465 | 1.154 | 3.17 | 0.188 |
| | $T_a$ = 1000 °C | 0.398 | 1.263 | 2.413 | 0.193 |
| **T835** | As dep. | 0.320 | 1.468 | 1.725 | 0.219 |
| | $T_a$ = 1000 °C | 0.329 | 1.416 | 1.758 | 0.226 |

Figure 3.3 (a) and (b) show the Si 2*p* XPS spectra for T730 and T835 annealed at 1000 °C for bulk (post-sputtering) of the film. The spectra were fitted using Voigt line shapes in conjunction

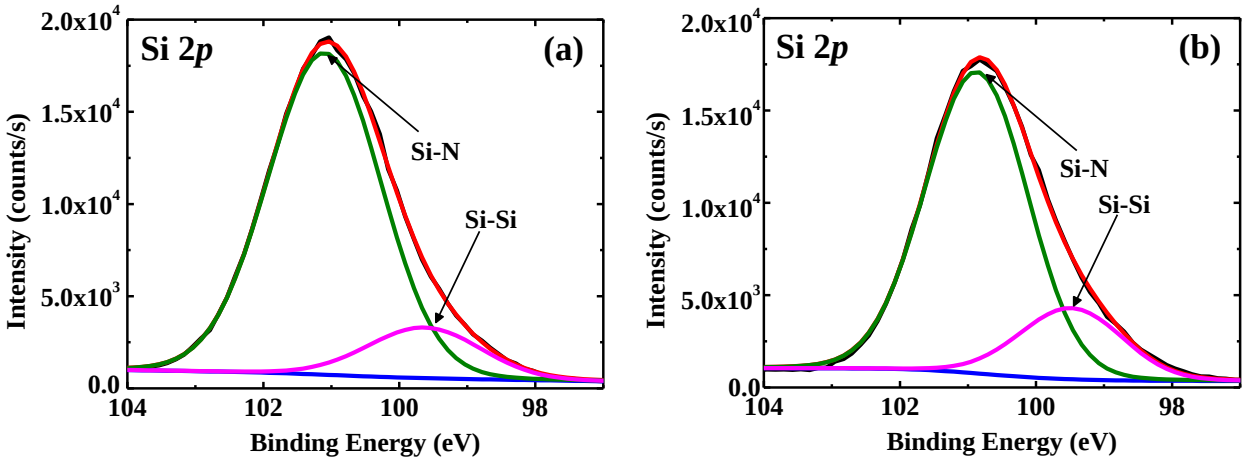


Figure 3.3. XPS of the Si 2p spectra for (a) T730 and (b) T835 annealed in $N_2$ at 1000 °C. The deconvolution gives two distinct peaks in both the samples, Si–Si (99.5 eV) and Si–N (100.9 eV) type bonding. The ratio between Si–Si peak area to Si–N peak area is larger in T835 than T730, indicating that T835 is more Si-rich than T730.

with a Shirley background subtraction utilizing "AAnalyzer" software [88]. Detailed peak fitting of the Si 2*p* spectra shows two peaks centered at 99.5 eV and 100.9 eV corresponding to Si–Si and Si–N type bonding, respectively, as expected for Si-rich silicon nitride films. The N 1*s* spectra (not shown) confirm the Si–N bonding. The ratio of the Si–Si to Si–N integrated intensities (i.e. Si–Si peak area: Si–N peak area) is larger in T835 than T730, indicating that T835 is more Si-rich than

T730. Additionally, the binding energy separation between the N 1*s* and Si 2*p* spectral regions is larger for T835 compared to T730, again revealing that T835 is more Si-rich.

A multi-component Si-rich $Si_3N_4$ ellipsometry model was constructed for determining the optical and structural properties of the thin film. The film thickness and volume fraction were determined using the Bruggeman Effective Medium Approximation (BEMA) for silicon nitride [89]. The optical properties were obtained using the Tauc-Lorentz model [90]–[92]. For a single transition, the imaginary part of the dielectric function is given by,

$$\epsilon_{TL} = \begin{cases} \dfrac{AE_0\left(E - E_g\right)^2}{(E^2 - E_0^2)^2 + C^2E^2}\dfrac{1}{E}, E > E_g \\ 0, E \leq E_g \end{cases}$$

where $E_0$ is the energy of the absorption peak, $E_g$ is the optical band gap, $C$ is the broadening parameter and $A$ represents the oscillator strength. In calculating the band gap $E_g$, the parameters from Ref. [92] were used to fit the data. The model was derived using the pre-defined dispersion formula in the DeltaPsi2 software where a combined layer of a-Si and a-$SiN_x$ was used on top of a c-Si reference. In addition, it was assumed that there were no voids within the SRN layer and the surface of the film was uniform. However, since the presence of surface native oxides was observed in the FTIR/XPS, a thin layer of $SiO_2$ was also included. The thickness and volume fraction were initially measured using the reference files of the materials with the optical constants fixed. The refractive indices, absorption coefficients and the band gaps were then obtained by performing the fit using the TL parameters with the results shown in Table 3.3.

The data indicates (and is consistent with XPS and FTIR) the films to be comprised of two distinct, phase separated SRN regions with different compositions for both T835 and T730 (similar

to precipitates in a host matrix). In each sample, the precipitate SRN regions are found to be very Si-rich with a Si:N ratio of 1.25 for T835 and 1.20 for T730 corresponding to a SRN with bandgaps of 2.5 eV and 2.7 eV, respectively [93]. However, only a small fraction of the total film volume is composed of this material (17% in T835 and 10% in T730). The host matrix SRN was found to have a band gap of approximately 4.9 eV and a Si:N ratio of 0.78 in both cases. These findings are consistent with the previously described XPS analysis and again confirm that T835 is more Si-rich than T730. We believe the detection of these precipitates within a host matrix indicates the onset of QD formation although these precipitates are not fully formed QDs. The relatively low density of these precipitates in conjunction with the high concentration of defect states leads to the PL spectra being dominated by non-radiative recombination with the fast time decay.

Table 3.3. Measured thicknesses, band gaps, and volume fractions of multiple Si-rich compositions in samples T730 and T835. The refractive indices and absorption coefficients are listed for 550 nm wavelength.

| **Sample** | | **Thickness (nm)** | **Refractive index $n_0$** | **Absorption coefficient $k_0$** | **Si-$Si_3N_4$ (1) $E_g$ (eV)** | **Si-$Si_3N_4$ (2) $E_g$ (eV)** | **Si-$Si_3N_4$ (2) $f$ (%)** | $\chi^2$ |
|---|---|---|---|---|---|---|---|---|
| **T730** | As dep. | 107.81 ± 1.38 | 2.227 | 0.362 | 4.89 ± 0.22 | 2.60 ± 0.08 | 9.89 ± 1.09 | 1.963 |
| | $T_a$ = 1000 °C | 105.81 ± 1.23 | 2.227 | 0.381 | 4.92 ± 0.23 | 2.70 ± 0.08 | 10.45 ± 1.29 | 2.201 |
| **T835** | As dep. | 135.39 ± 1.57 | 2.329 | 0.456 | 4.89 ± 0.19 | 2.50 ± 0.05 | 14.38 ± 1.64 | 1.793 |
| | $T_a$ = 1000 °C | 126.97 ± 1.15 | 2.371 | 0.498 | 4.87 ± 0.22 | 2.55 ± 0.05 | 16.89 ± 1.82 | 1.877 |

The FTIR spectra of these films are shown in Figure 3.4. The detector cuts off the spectra at 650 $cm^{-1}$ which explains the drop in intensity below 700 $cm^{-1}$. The peak centered at 800 $cm^{-1}$, is attributed to a Si–N stretching mode as a $Si_3$–Si–N like bonding arrangement [94]. This chemical species corresponds to the very Si-rich precipitate SRN observed in the ellipsometry data. Hasegawa [95] previously observed a peak near 840 $cm^{-1}$ which was assigned to be $Si_2$–Si–N bonding. Lucovsky proposed that peaks arising within the range of 836 $cm^{-1}$ to 854 $cm^{-1}$ correlate with the $Si_3$–Si–N stretching mode where a silicon atom is replaced with a H atom [94]. However,

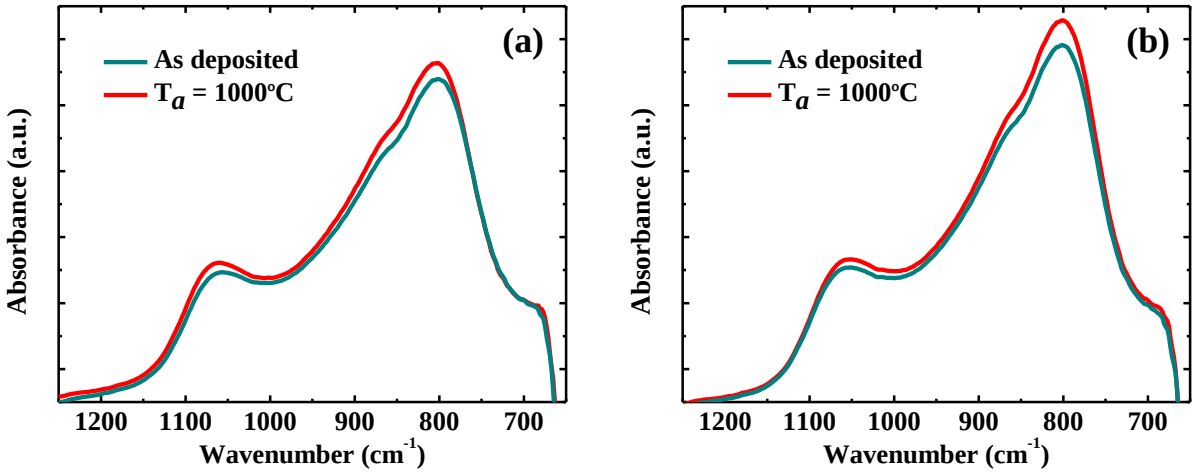


Figure 3.4. FTIR spectra for (a) T730 and (b) T835. The peaks at 800 $cm^{-1}$ and 865 $cm^{-1}$ are from the Si-N stretching modes of the very Si-rich precipitate SRN and the host SRN, respectively.

the absence of peaks in our data corresponding to Si–H (2126 – 2152 $cm^{-1}$) and N–H (1177 and 3340 $cm^{-1}$) indicates that these samples have no residual hydrogen due to the elevated deposition temperature, despite the use of silane as a precursor. Therefore, the peak in our data, centered at 865 $cm^{-1}$, is attributed to a $Si_x$–Si–N ($x \leq 2$) bonding arrangement and correlates with the host matrix. These two peaks observed in the FTIR are consistent with the Si 2*p* spectra from XPS. We note the absence of a peak near 950 $cm^{-1}$, which other authors have observed as a N-rich $SiN_4$ bond [96]. The peak centered at 1065 $cm^{-1}$ is due to surface Si–O–Si bonds which do not play a

role in the observed PL. XPS measurements confirmed the presence of surface oxides in the pre-sputtered films, which were not present in the bulk of the film (not shown).

Raman measurements were performed on the samples to identify an amorphous or crystalline Si phase due to QDs in the film, yet no observable differences were noticed in the as deposited or annealed samples. XRD also did not show the evolution of crystalline Si in the film that would indicate the presence of a nanocrystalline quantum dot. The film was amorphous in nature, which was confirmed by HRTEM (not shown), further confirming that the PL emission was not due to Si-QDs.

C-V measurements were performed on SRN MISCAPs with an area of 0.03 $mm^2$. As seen in Figure 3.5, a large hysteresis is observed in the samples signifying a large number of bulk traps present within the SRN thin film. The hysteresis is larger for the T835 sample indicating that this film has more bulk traps than the T730 sample. The relation $N = \Delta V_{FB} C_{max}/e$ approximates the

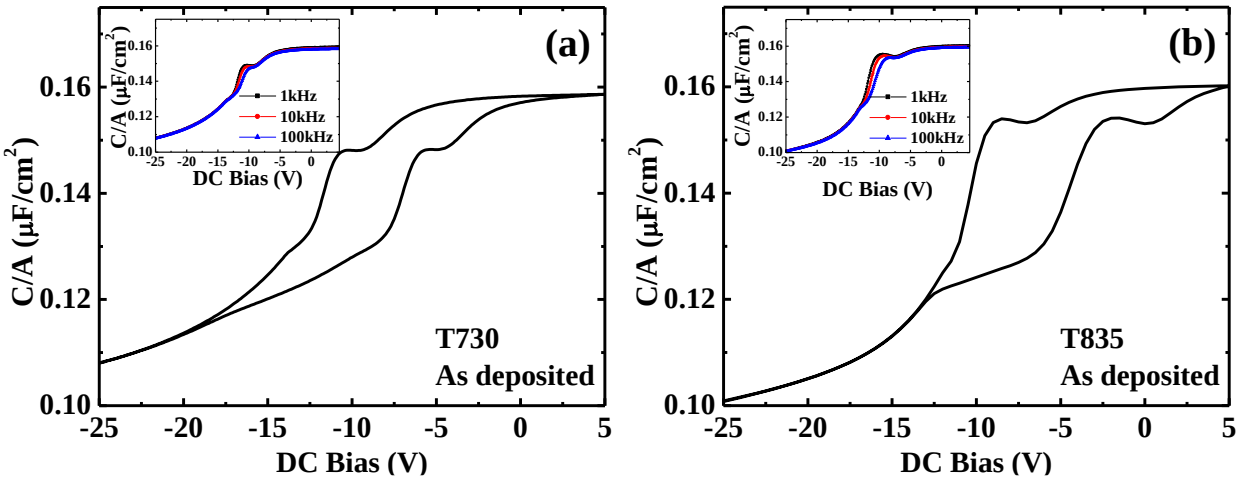


Figure 3.5. C-V measurements on the 50 nm thick SRN MISCAPs. The hysteresis was measured for the 10 kHz frequency. The wide hysteresis loop indicates that there are trapped charges in the SRN layer. The inset shows the C-V measured at different frequencies. The "hump" observed at -11V is due to a large number of defects present at the Si-wafer SRN interface. In T835, the "hump" increases indicating a larger concentration of defects present in T835 compared to T730 and correlating with increased Si DB concentrations in the more Si-rich sample.

density of traps within the films which was calculated to be ~$4.4\times10^{12}$ $cm^{-2}$ to $6.0\times10^{12}$ $cm^{-2}$. The insets in Figure 3.5 show a frequency dependent defect response observed at ~ -11V, due to a large number of defect states at the Si substrate interface. This defect state "hump" increases for the T835 sample, again indicating that for higher deposition temperatures, more defect states are present than for the T730 sample. These electrical measurements indicate that with increasing deposition temperature and the resulting increase in Si content, Si-DB defect states increase which correspond to the increased intensity of certain PL peaks as well as the XPS, FTIR, and ellipsometry data. In total, the data suggests that the PL peaks and shift in PL intensity demonstrated in Figure 3.1 is caused by composition-dependent defect state transitions and not QDs.

### 3.4 Discussion

After careful investigation using the aforementioned characterization techniques, it has been confirmed that a quantum confined state is absent within the matrix that would yield the peaks observed in the PL. Instead, we attribute the PL emission to defect states present within the SRN. The results observed from XPS, FTIR, ellipsometry and C-V measurements are in clear agreement with a correlation between defect states and the PL peaks observed.

In order to account for the multiple PL emission peaks, a model for the LPCVD grown SRN is proposed that combines the two separate SRN materials with distinct band gaps (as described in the ellipsometry data) in the form of a complex structure as shown in Figure 3.6. The thin film consists of defect states arising from Si- and N-dangling bonds. The neutral Si-DB, otherwise known as the $Si^0$ center is located energetically near mid-gap in silicon nitride. Due to

charge transfer, the neutral Si-DB can have charged states, $Si^+$ and $Si^-$, which are energetically located on either side of the $Si^0$ center. The N-DB has been calculated near the valence band of the silicon nitride [97]. In highly Si-rich materials such as these, the Si-centers are the predominant defect states present. The energetic positions of the Si- and N-DBs, with respect to vacuum, are

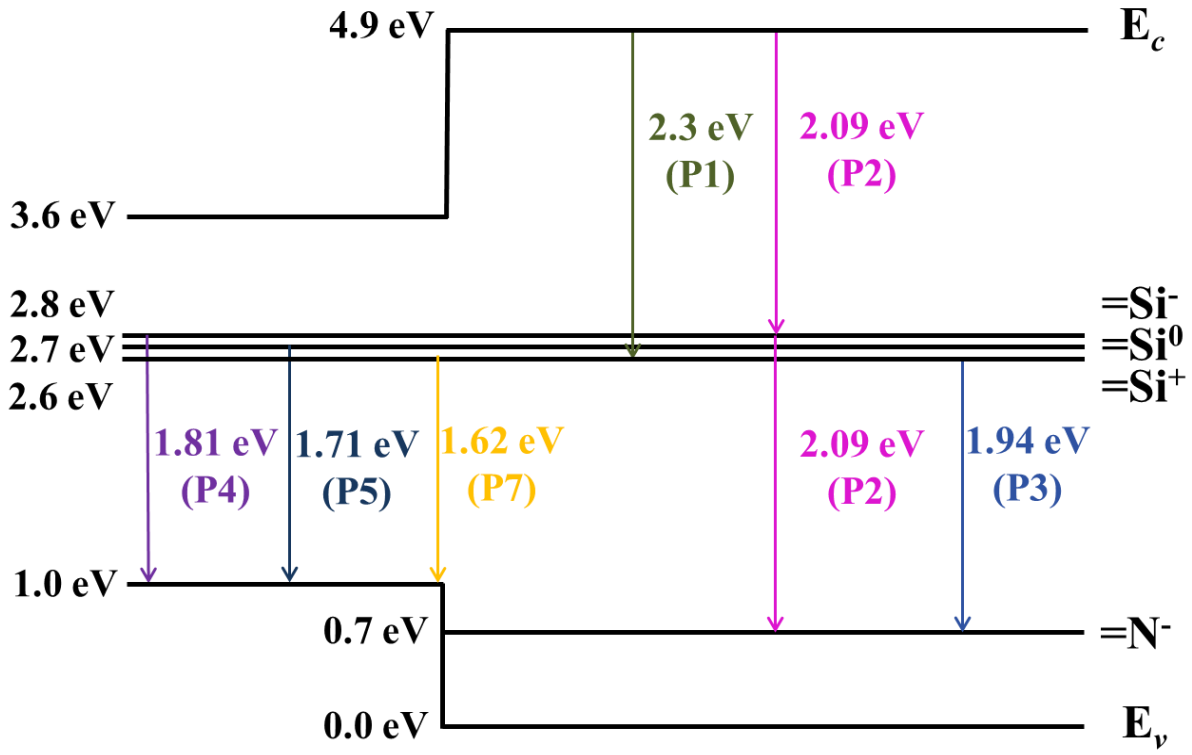


Figure 3.6. Proposed energy level structure of the SRN films. The energy levels of the defect states and band gaps are referenced with respect to the host matrix valence band. The left side of the model represents the precipitate SRN with a band gap of ~2.7 eV for T730 and ~2.5 eV for T835. The right side of the model is the host SRN matrix with a band gap of ~4.9 eV. The proposed transitions are color coordinated with the correlated deconvoluted peaks in the PL (Figure 3.1).

believed to be fixed, regardless of the film stoichiometry.

By considering the above model, we propose the following intermediate transitions between the band edges and the defect states (see Figure 3.6) that correlate with the observed PL peak intensities. The peak intensities in the PL for most of the peaks emerge from a single energy

transition while one of the peaks may utilize multiple energy transitions [98]. Peak P1 (2.3 eV) is assigned to a transition from the host matrix conduction band to a positively charged Si dangling bond state ($E_c \rightarrow Si^+$). Peak P2 (2.09 eV) is attributed a transition from the host matrix conduction band to the negatively charged Si dangling bond state ($E_c \rightarrow Si^-$) with additional contribution from the equivalent magnitude energy transition from that charged Si dangling bond state to a nitrogen dangling bond ($Si^- \rightarrow N^-$). P3 (1.94 eV) corresponds to the transition from the positively charged Si dangling bond state to the nitrogen dangling bond state ($Si^+ \rightarrow N^-$). Those first three peaks are each associated with the defect states and band edges of the host SRN matrix. With the increase in the deposition temperature, the peak intensities for P1, P2, and P3 are observed to *decrease* as the sample gets more Si-rich (i.e. the precipitates become a larger percentage of the film and there is a concomitant decrease of the percentage of the film that is the host matrix). As the concentration of the host material decreases, the transitional probabilities related to the PL intensities decrease as well. Peaks P4 (1.81 eV), P5 (1.71 eV), and P7 (1.62 eV) are attributed to transitions associated with the *precipitate* SRN that correspond to transitions from the three charge states of Si dangling bonds to the precipitate valence band edge, respectively (i.e., $Si^- \rightarrow E_v$, $Si^0 \rightarrow E_v$, and $Si^+ \rightarrow E_v$). The intensities of these peaks are observed to *increase* at higher deposition temperature, again due to the fact that the increase in the concentration of the precipitate SRN and the increased Si content within the precipitate increases the probability of those defect state transitions. Finally, peak P6 at 1.66 eV (746 nm) is observed to have a narrower Gaussian width compared to the other peaks. The origin of this transition is unknown at this time.

## 3.5 Conclusion

Si-rich silicon nitride films grown by LPCVD and furnace annealed have been investigated to understand the origin of the complex PL spectra observed. The PL spectra originating from these samples are not due to quantum confinement, but from Si- and N-dangling bond defect states within the material. Detailed correlation between multiple spectroscopic techniques has established that the SRN films have two distinct, phase separated SRN regions with different compositions, a highly Si-rich precipitate (the onset of a Si QD) and a Si-rich host matrix. The defects present in both regions of the SRN material account for transitions which correlate with the intensities of the deconvoluted peaks in the PL. The changes in the PL intensities are related to an increase in the Si-content for depositions performed at higher temperature. The defect states of the SRN therefore play a significant role in the material properties, and are very important to consider when investigating these materials for QD applications.

# CHAPTER 4

# CHARACTERIZATION OF SI-RICH NITRIDE AND SI-RICH OXIDE USING REACTIVE SPUTTER AND CO-SPUTTER DEPOSITION

## Participation

All experiments and data analysis were performed by myself with the following exceptions – The samples for TEM were prepared and images were obtained by Dr. Carlo Floresca from Professor Moon Kim's group. The photoluminescence and time resolved photoluminescence spectra were collected by Dr. Siddharth Sampat from Dr. Anton Malko's group.

## 4.1 Introduction

This chapter focuses on the deposition and characterization of the Si-rich oxide (SRO) and Si-rich nitride (SRN) films that were prepared in the sputtering system and consequently annealed at high temperature to form nanocrystalline silicon quantum dots (Si-QDs). Sputtering offers a better control over the stoichiometries of the films by gradually changing either the gas flow (in reactive sputtering) or power of the targets (in co-sputtering). This was critical after forming the silicon-rich silicon nitride or silicon oxide films. Besides, it was also offers deposition at room temperature and faster loading and unloading of samples over LPCVD.

An extensive study of the SRN and SRO films are presented in this chapter in terms of physical, chemical and optical characterization. There is evidence that nanocrystalline Si-QDs were formed both in SRN and SRO. The room temperature PL along with the time-resolved PL and low temperature PL all supported the presence of a Si-QD in the SRO sample. The reactively sputtered $SiN_x$ films after annealing exhibited crystalline Si in TEM image, which was further

supported by XRD and Raman. However, when illuminated under the laser, no PL could be detected. The TRPL spectra was fast decaying, which again indicated that the PL was exclusively due to defect states within the $SiN_x$.

## 4.2 Experimental

Initially, the SRN films were investigated using reactive sputtering of Si in $N_2$/Ar environment. The second set of experiments were performed on co-sputtered SRO, where the power of $SiO_2$ target was fixed while the power of the Si target was varied only.

The films were deposited on Si(100) wafers which were etched in dilute HF (100:1) initially for 2 minutes for removing the native oxides. All depositions were carried out in the AJA 1500 sputter tool at room temperature. The chamber was evacuated to a base pressure of $\sim 5\times10^{-7}$ Torr prior to deposition. For reactive sputtering, the power of Si target was fixed at 200 W while the $N_2$ and Ar gas flows were varied. For the co-sputtering, a constant flow of Ar at 20 sccm at $4\times10^{-3}$ Torr pressure was maintained while the power of Si varied and the power of $SiO_2$ target was fixed at 100 W. The deposition times varied accordingly to obtain a thickness of 100 nm for each different sample. The samples after deposition were cleaved and separate pieces of the same deposition were furnace annealed for 60 minutes in $N_2$ (99.9998% pure) ambient.

High-resolution transmission electron microscopy (HRTEM) images were obtained from a 200 kV field emission JEOL 2100F instrument. A Rigaku Ultima III X-ray diffractometer (XRD) configured for grazing incidence angle was used to probe the crystal structure of the films. A Nicolet Almega XR Dispersive Raman spectrometer was excited at 532 nm at room temperature to measure the chemical structure of the SRN and any QD precipitates that may have formed during

anneal. The room temperature photoluminescence measurements were carried out using a Ti:Sapphire laser for the reactively sputtered $SiN_x$ and a PicoQuant diode laser for the Si-rich $SiO_x$ samples. Further details of the PL settings are described in the following sections.

## 4.3 Reactive Sputtering of $SiN_x$

The two samples studied in this experiment were prepared by varying the $N_2$ flow rate to 0.5 sccm and 1 sccm while keeping the total flow of Ar and $N_2$ fixed to 20 sccm. The deposition conditions are listed in the table below.

Table 4.1. Deposition conditions of the reactively sputtered $SiN_x$ thin films.

| Sample | Pressure | Si Power | $T_D$ | $N_2$ flow | Ar flow |
|---|---|---|---|---|---|
| **RS1** | 4 mTorr | 200 W | 17 °C | 0.5 sccm | 19.5 sccm |
| **RS2** | | | | 1 sccm | 19 sccm |

The samples were subsequently annealed in the MiniBrute furnace for 60 minutes at temperatures $T_A$ = 800 °C, 900 °C and 1000 °C.

The samples were thinned and cleaned using the focused ion beam (FIB) prior to TEM imaging. The high resolution TEM (HRTEM) image of both the samples annealed at 1000 °C were obtained in order to observe crystalline structures of Si that may have formed during annealing. In Figure 4.1 (a) and (c), the full thickness of the $SiN_x$ thin film deposited on the Si wafer are visible. RS2, with a higher $N_2$ flow shows several tiny black spots distributed throughout the film, which after further zooming, as seen on Figure 4.1 (d), appears to have an ordered structure (circled region) surrounded by an amorphous structure, which is the a-$SiN_x$. Similar ordered structures have been reported by other authors that confirmed the presence of a Si-NC within a nitride matrix [45], [77], [99], [100]. The average grain size of the crystalline structure was estimated to be 7.5

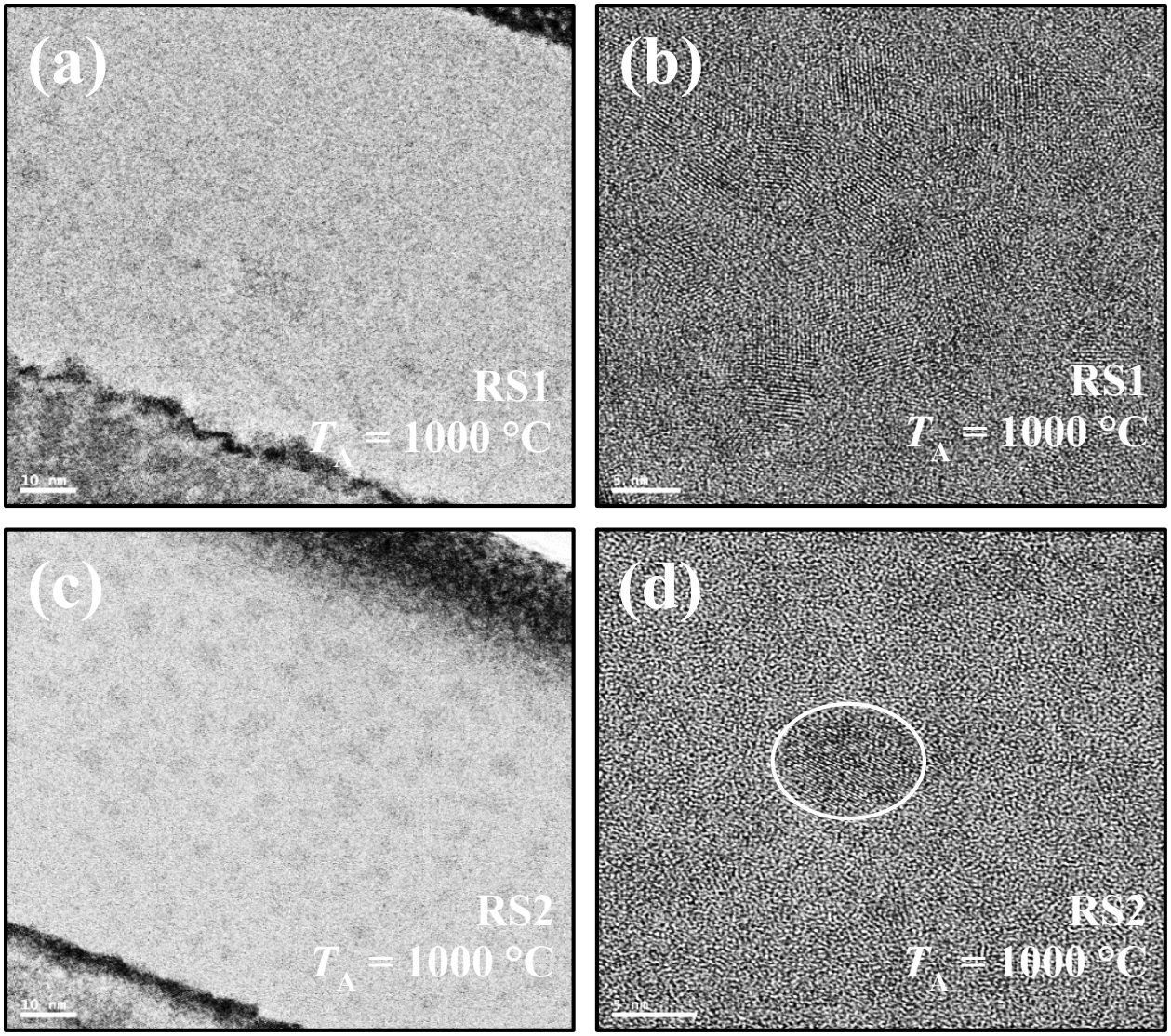

Figure 4.1. HRTEM image of the reactively sputtered $SiN_x$ films after annealed at 1000 °C. (a) and (c) are the full view of the $SiN_x$ layer on Si wafer for RS1 and RS2. (b) and (d) are the zoomed-in view of the same samples showing the morphology of the films with possible nanocrystals forming in the RS2 sample.

± 0.5 nm. Sample RS1 in Figure 4.1 (b) appear to have several overlapping ordered structure, which is characteristics of a polycrystalline Si.

To further verify the crystallinity of the films after annealing, X-ray diffraction (XRD) was collected on the as deposited and annealed samples of RS1 and RS2. The XRD spectra was collected at a grazing incidence angle $\Omega = 0.5°$ with a scan speed of 1°/min. Figure 4.2 is the XRD

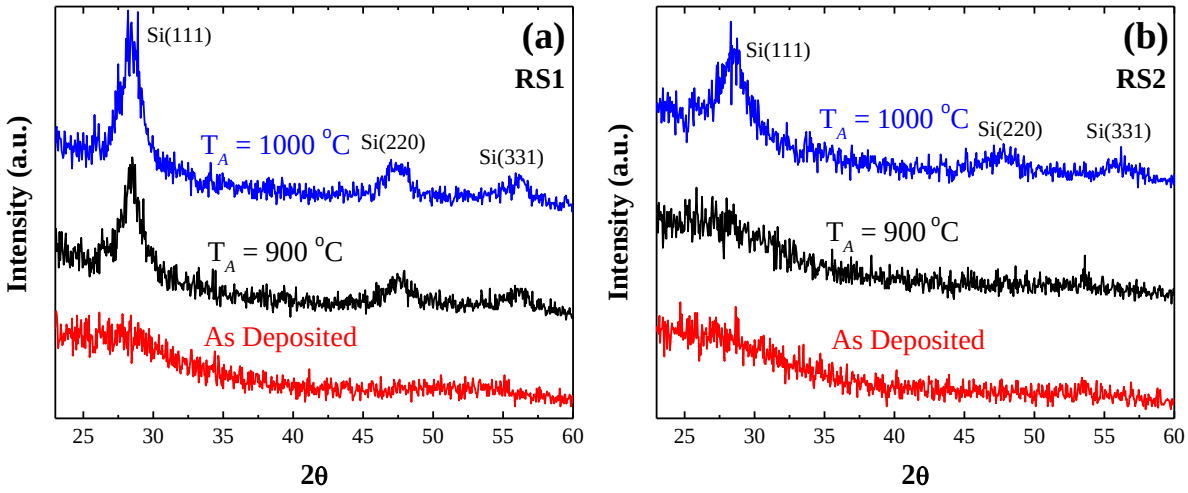


Figure 4.2. The GI-XRD spectra collected at Ω = 0.5° for the reactively sputtered $SiN_x$. (a) RS1, with a lower $N_2$ flow, shows that silicon starts crystallizing at 900 °C, whereas in (b) RS2, the crystallinity starts at 1000 °C.

of the $SiN_x$ samples scanned between 20° and 60°. No peaks appeared in the as deposited films meaning that they were amorphous after deposition. It is observed that higher temperature yields a higher concentration of crystalline Si in the film. The crystalline peaks of Si from planes (111), (220) and (311) are visible at 28.3°, 47.5° and 55.9°, respectively, after the sample RS1 was annealed at 900 °C and the intensity of the peaks further increased at 1000 °C. For RS2, which had a higher flow of $N_2$, thereby a reduced excess Si, the crystalline peaks only appeared after the sample was annealed at 1000 °C.

The Raman spectra presented in Figure 4.3 was collected for the RS2 as deposited and high temperature annealed samples. The as deposited sample, however, does not contain any amorphous Si phase due to excess Si centered at 480 $cm^{-1}$ as was reported in [101]–[103]. At 800 °C, a small peak centered at 521 $cm^{-1}$ and a broad peak at ~480 $cm^{-1}$ is observed, indicating a phase separation in a-$SiN_x$ forming a mixed a-Si and c-Si within the $SiN_x$. The peak at 521 $cm^{-1}$ further increased with 900 °C and 1000 °C. The peaks could not be correlated directly with XRD, especially in the

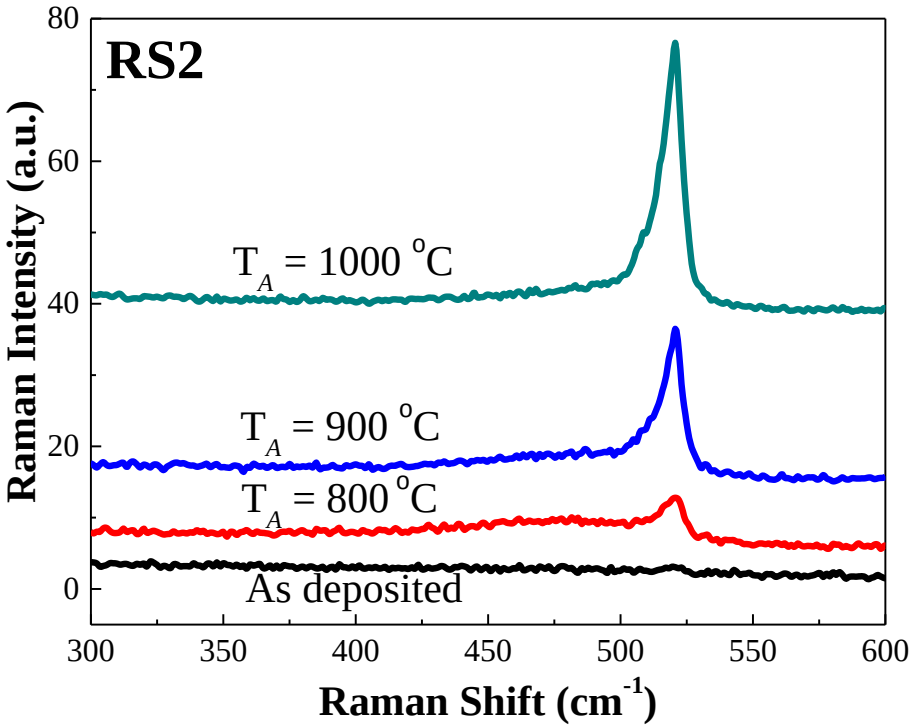


Figure 4.3. The phase transformation of the $SiN_x$ film RS2 due high temperature anneal as observed in the Raman spectra. The peak at 521 $cm^{-1}$ is due to the formation of Si-NC within the silicon nitride.

900 °C sample as no peak was observed in XRD whereas a sharp peak appeared in Raman. It could be due to difference in the limits of detection of these two techniques. In Raman, a crystalline structure can be detected within 0.1 at% whereas in XRD, the crystalline structures in an amorphous film are limited to a detection limit of 2 at% only [59].

With the evidence of Si-NC observed in TEM, XRD and Raman, it was important to study the photoluminescence (PL) spectra of the $SiN_x$ samples, especially in RS2. The room temperature PL was carried out by exciting the Ti:sapphire laser with 120 fs pulses at 405 nm at a repetition rate of 7.6 MHz and a power of 61 μW. At such a high power, the multiple peaks observed in the PL in Figure 4.4 (a) were only from the background. After annealing, no change in the PL spectra could be observed from the films, indicating that the laser could not excite any of the Si-NCs

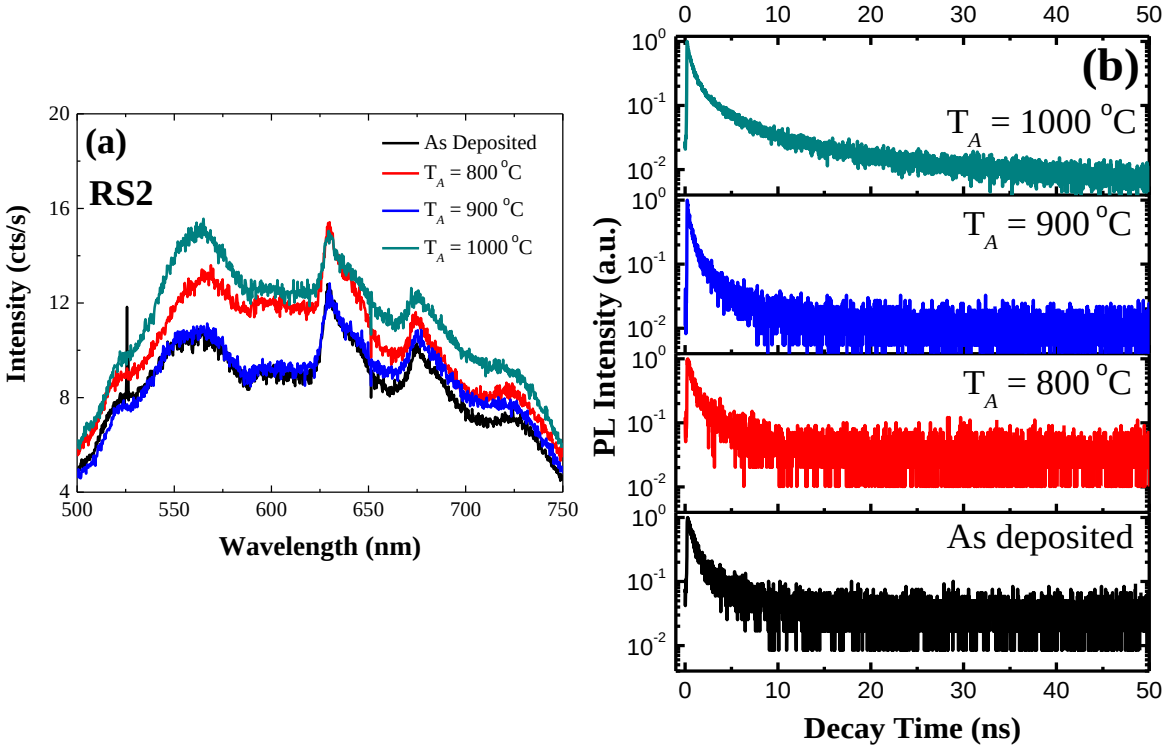


Figure 4.4. (a) The PL spectra of the as deposited and annealed samples of RS2 and (b) the corresponding time resolved PL decay of the samples.

within the $SiN_x$. Figure 4.4 (b) shows the time resolved PL spectra of the same samples, which are similar in characteristics in terms of decay time as was observed in the LPCVD grown SRN samples. The fast decay times indicate that the PL was again likely due to non-radiative states and not characteristics of Si-QDs.

## 4.4 Si-rich $SiO_x$ by Co-sputtering

Most of the research on Si-nanocrystals has been sought after $SiO_2$ based host matrices due to its well defined structural properties and simpler processing steps [12], [29], [31], [104], [105]. In order to better understand the quantum confinement effect, Si-rich $SiO_x$ films were prepared by sputtering the Si and $SiO_2$ targets together. The samples were sputtered on a n-type Si wafer at a

deposition pressure of $4\times10^{-3}$ Torr and constant Ar flow of 20 sccm at room temperature. The power of the $SiO_2$ target was kept fixed at 100 W while the power of Si varied only. Table 4.2 lists the deposition condition of the Si-rich $SiO_x$. The samples were labeled according to the power of the Si target.

Table 4.2. Deposition condition for the co-sputtered Si-rich $SiO_x$ films.

| Sample | Si power | $SiO_2$ power |
|---|---|---|
| O45 | 45 W | 100 W |
| O50 | 50 W | |
| O55 | 55 W | |
| O60 | 60 W | |

Soon after deposition, the samples were cleaved and separate pieces were annealed in the MiniBrute furnace in $N_2$ (99.9998%) ambient at 1100 °C for 60 minutes.

The room temperature PL measurements were carried out using a PicoQuant diode laser (50 ps pulse at 400 nm) with the repetition rate set to 200 kHz and a power of 20 nW. Lifetime data were measured using an avalanche photodiode with 250 ps resolution (Perkin Elmer SPCM AQR 13). Spectral data were collected using a liquid nitrogen cooled silicon CCD (Princeton Instruments).

Figure 4.5 (a) shows the PL spectra of the Si-$SiO_x$ samples after annealing. As opposed to the power or repetition rate used to collect the PL in $SiN_x$ samples, which was in the micro-watts and megahertz range, respectively, the parameters were low for the Si-$SiO_x$ samples. Even with such a low power and rate, an intense PL signal was observed from all the samples annealed at 1100 °C. The signals were composed of a single Gaussian, which means that a single effect may have caused the PL. The full-width half maximum (FWHM) of the spectra was ~120 nm. The PL intensity had increased from O45 to O50 and then eventually decreased for O55 and O60. This

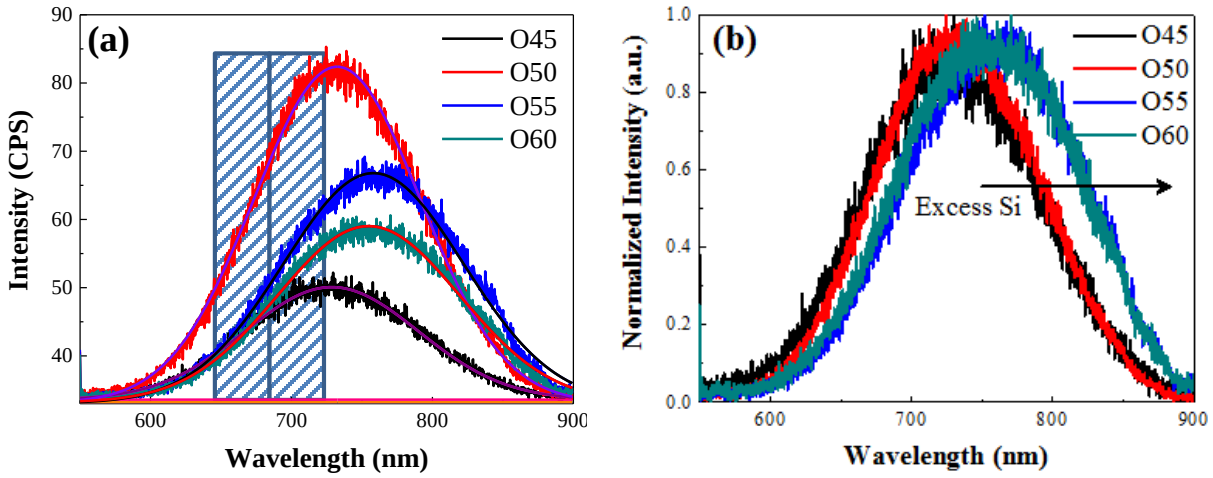


Figure 4.5. (a) The room temperature PL spectra of the Si-$SiO_x$ samples annealed at 1100 °C. The shaded region is the spectral window of the filter that was used to collect the TRPL. The solid lines represent the fits used to show that the peak composed of a single Gaussian only. (b) Normalized spectra of the Si-$SiO_x$. It is clearly visible how the PL redshifted as the concentration of excess Si increased.

means that the PL reached to a saturation for a certain concentration of Si and then it decreased as more Si was incorporated. When normalized, as seen in Figure 4.5 (b), the peaks shift to lower energy (higher wavelength) as more Si is incorporated. A similar trend in the PL spectral intensity change and shift in energy was reported by Charvet *el al*. [106] for a magnetron co-sputtered $Si/SiO_2$.

The PL peak position with the concentration of excess Si was related to the increase in the grain size of the nanocrystals, which is the basis of the quantum confinement effect. For an increase in the size of the nanocrystals, the PL peak is expected to redshift. The PL peak intensity was also observed to increase due to increase of Si into the films from 6% to 12%, but then it dropped for Si > 15%. The reason explained was that the relatively larger grain sizes due to the continuing Si enrichment could not luminesce and hence the overall PL emission decreased [106].

The time resolved PL spectra was collected using a filter centered at 680 ± 40 nm (shaded region in Figure 4.5 (a)) and are presented in Figure 4.6. The detector was only limited to a window collecting the decays up to 10 μs and the Si-$SiO_x$ annealed samples were observed to extend the decay beyond the window as the counts were still above zero. However, within the detection window, the spectra could be fitted using an exponential decay function that resulted in a decay time between 5 μs to 15 μs. Typically, the decay time of Si-QDs embedded in $SiO_2$ has been reported to be in the order of hundreds of microseconds to tens of milliseconds [107]–[109]. The

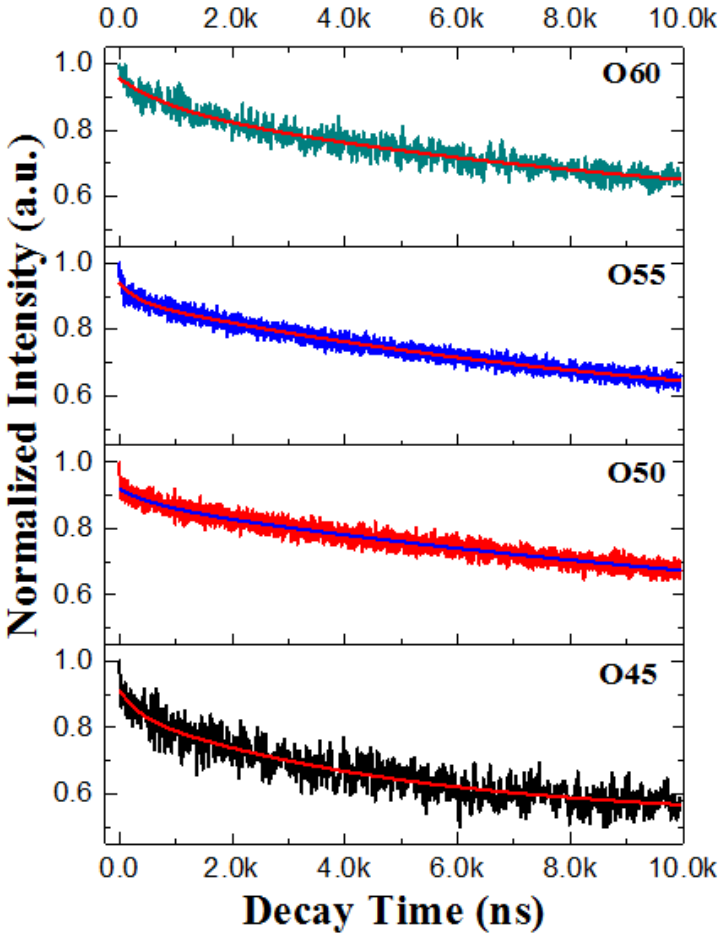


Figure 4.6. The time resolved PL spectra of the Si-$SiO_x$ samples annealed at 1100 °C. The solid line represents the fit performed over the decay curve.

detector window for the measurement of TRPL in the published literatures were broader to record the lifetime up to milliseconds in range.

However, the long decays along with the highly intense PL that redshifted with excess Si incorporation were a direct evidence that Si-QDs were present in the Si-$SiO_x$ system after annealing.

To further investigate the behavior of the quantum dots, low temperature PL and TRPL were collected from the samples. The low temperature measurements were performed in liquid nitrogen (LN2) for the sample O50 annealed at 1100 °C, which had the maximum PL intensity. The PL and TRPL were collected by lowering the temperature from room temperature (293K) to the LN2 temperature of 80K. The spectra are shown in Figure 4.7. It was noticed that the PL intensity increased as the measurement temperature decreased. The TRPL also had a longer exponential decay from 293K to 230K. But due to the limitation in the detector window, decay times measured at lower temperatures appeared to overlap with each other. As reported by Rinnert

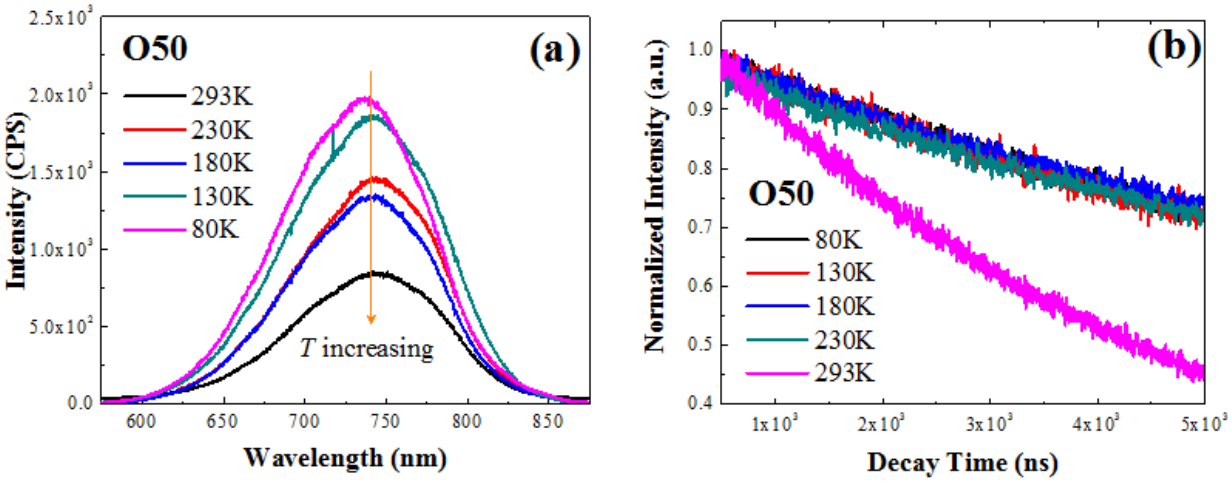


Figure 4.7. (a) The low temperature PL spectra in LN2 of the Si-$SiO_x$ sample O50 annealed at 1100 °C. The intensity of the PL increases as *T* decreases. (b) Normalized TRPL spectra of the same sample at low temperatures.

*et al*. [108] and Dovrat *el al*.[107], the decay times were observed to increase as the temperature was lowered from room temperature to liquid helium. At room temperatures, the TRPL is governed by both the radiative decay arising from the nanocrystals and non-radiative decay from its surroundings, namely from the defect states. The total lifetime is expressed in terms of the equation:

$$\frac{1}{\tau} = \frac{1}{\tau_R} + \frac{1}{\tau_{NR}}$$

where $1/\tau_R$ and $1/\tau_{NR}$ are the radiative and non-radiative decay rates, respectively [110]. At higher temperatures, the non-radiative processes play an important role, which in effect causes the total lifetime to decrease. As the temperature is further lowered, the decay lifetime is mainly governed by the radiative process $\tau \approx \tau_R$. Therefore, at lower temperatures, the lifetimes are longer.

The same reasoning applies to the PL intensity as well. As the measurement temperature is lowered from the room temperature, the PL is less affected by the temperature-activated non-radiative processes thereby increasing the overall intensity.

With the increase in the PL intensity at lower temperatures, the PL peak energy was observed to be shifting at higher energies (lower wavelength). In bulk semiconductors, the evolution of the gap with temperature is generally described by the phenomenological Varshni's law:

$$E_g^{bulk}(T) = E_g^{bulk}(0) - \frac{\alpha T^2}{T + \beta}$$

where $\alpha$ and $\beta$ are characteristic parameters [111]. This equation is well described for the evolution of Si gap with the variation in temperature. Similar argument was also presented for Si-NCs where

the gap was observed to vary thereby causing a blueshift in the PL peak energy at lower temperatures [108].

## 4.5 Conclusion

The goal of this chapter was to establish the framework for sputter deposition of Si-rich nitride and Si-rich oxide films in order to precipitate Si-nanocrystals after high temperature anneal within their respective matrices.

Reactive sputtering was performed using $N_2$ gas and Si target to prepare $SiN_x$ samples with different concentrations and eventually annealed at high temperatures. TEM indicated that regions within the silicon nitride had formed ordered structure resembling Si-NC. XRD further confirmed that the films had crystallized the excess Si after high temperature anneal. Raman also indicated that a phase transformation occurred at higher temperatures due to the peak intensity increasing at 521 $cm^{-1}$, which was characteristics of crystalline Si (c-Si).

However, when the samples were illuminated under the laser at sufficiently high power, no PL spectra could be detected except for its background. Also, the time resolved PL (TRPL) spectra had a very fast decaying lifetime, which indicated that the PL was coming from the non-radiative states only.

On the other hand, Si and $SiO_2$ were co-sputtered in the same chamber to form Si-rich $SiO_x$. After annealing the films at high temperature, a very strong PL was observed when the samples were excited at a lower power as opposed to the $SiN_x$. The PL FWHM was also narrower and single Gaussian like indicating that the effect was most likely due to the transition between band edges from a Si-NC. The TRPL also exhibited a very long lifetime, which is characteristics of the decays observed from an indirect bandgap semiconductor. The low temperature measurements

yielded a further increase in the PL intensity as the temperature was lowered, which indicated a reduction in the temperature-active defect states. The TRPL spectra also decayed with a longer lifetime and the PL peak energy shifted that related to the change in semiconductor gap states as was explained by Varshni's law.

# CHAPTER 5

# OXIDE RELATED DEFECTS IN QUANTUM DOT CONTAINING SILICON RICH SILICON NITRIDE FILMS

## Participation

All experiments and data analysis were performed by myself with the following exceptions – The photoluminescence and time resolved photoluminescence spectra were collected by Dr. Siddharth Sampat from Dr. Anton Malko's group. Raman spectra were collected from Prof. Yves Chabal's laboratory. Useful discussions and contributions were provided by Dr. Lee Walsh from Dr. Chris Hinkle's group.

## 5.1 Introduction

Silicon nanocrystals (Si-NC) embedded in a silicon oxide or nitride matrix have been an extensively researched field which attempts to open the door to overcoming bulk silicon's light emission inefficiency for optoelectronic devices. Much of the research of nanocrystals has been focused on $SiO_2$-based host matrices due to its well defined structural properties and simpler processing steps [12], [29], [31]. However, the high band offsets of the $SiO_2$ matrix with nanocrystalline silicon quantum dots (Si-QDs) can suppress the tunneling probability of carriers into the QDs in devices designed for electroluminescent and photovoltaic applications. In contrast, there is an interest in developing such Si-nanocrystals in a lower bandgap matrix such as $Si_3N_4$ as it offers smaller band offsets, which in turn can enhance the electrical carrier injection for efficient extraction of light from Si-based light emitting diodes (LEDs) [112].

Despite offering promise in optoelectronics, $Si_3N_4$ matrices typically have a higher defect density compared to Si-oxide [73]. In addition, there has been a debate on whether the photoluminescence (PL) observed from Si-NC in $Si_3N_4$ is due to radiative decay from a quantum confined state [15], [113] or non-radiative decay from a defect state or band tail luminescence [78], [81], [114], [115]. Nguyen *et al.* studied the impact of oxygen on the PL of silicon-rich silicon nitride films although they still suggested that the crystalline Si quantum dots formed in the silicon nitride matrix had a significant contribution to the observed PL in addition to the contribution of the O-related defect states [116].

In this paper, the evidence for Si-nanocrystals in silicon-rich silicon nitride (SRN) is detected in X-ray diffraction (XRD), Raman spectroscopy, and X-ray photoelectron spectroscopy (XPS). However, using TRPL we show that the PL emission, observed after high temperature anneal, is a result of transitions to and from non-radiative defect states related to oxide defects within the thin film, with no substantial contribution from the nanocrystals. Additionally, the shift in the PL peak energy is correlated to the change in the composition-dependent bandgap of the silicon nitride host matrix and not due to the size distribution of the quantum dots.

## 5.2 Experimental

The silicon-rich nitride (SRN) films were deposited on n-type Si (100) wafers (doping density ~$10^{17}$ $cm^{-3}$) which were etched in diluted hydrofluoric acid ($H_2O$:HF = 100:1) for 2 minutes to remove the native oxide. The deposition was carried out at room temperature in an AJA 1500 sputter tool using both Si and $Si_3N_4$ targets. The chamber was evacuated to a base pressure of ~$5\times10^{-7}$ Torr prior to deposition. A constant flow of Ar at 20 sccm and a chamber pressure of

$4\times10^{-3}$ Torr was maintained during deposition while the radio-frequency (RF) power of the $Si_3N_4$ target was fixed at 100 W. The RF-power of the Si target was varied from 0 W up to 60 W with sample notation reflecting the Si target power, i.e. N00, N20, and N60. Each sample thickness was 100 nm. With the increase in Si target power, the Si/N concentration also increased forming a more Si-rich silicon nitride film. The Si/N ratios as calculated by XPS were 1.07, 1.08, and 1.52 for N00, N20, and N60 samples, respectively (with ±10% experimental error of the XPS atomic sensitivity factor and fitting). Although a $Si_3N_4$ target material was used to deposit the N00 sample, the Si/N ratio reveal that the deposited material was not stoichiometric, as reported in previous studies [117], [118]. After deposition, the samples were cleaved and separate pieces of the same sample were furnace annealed for 60 minutes at 900 °C, 1000 °C, and 1100 °C in $N_2$ (99.9998% pure) at a flow rate of 4.5 liters/min, a standard process flow for the fabrication of Si-NCs [99], [115], [119].

Room temperature photoluminescence measurements were carried out using a PicoQuant diode laser (50 ps pulse at 400 nm) with the repetition rate set to 5 MHz, a power of 1.25 μW, and a 350 nm wide data range. Lifetime data were measured using an avalanche photodiode with 250 ps resolution (Perkin Elmer SPCM AQR 13). Spectral data were collected using a liquid nitrogen cooled silicon charge coupled device (CCD, Princeton Instruments). A Nicolet Almega XR Dispersive Raman spectrometer (532 nm excitation wavelength) was used to measure the chemical structure of the SRN and any Si-NC precipitates that may have formed during annealing. A Rigaku Ultima III X-ray diffractometer (XRD) configured for grazing incidence angle was used to probe the crystal structure of the films. X-ray photoelectron spectroscopy (XPS) was performed using a PHI VersaProbe II spectrometer equipped with an Al Kα monochromated X-ray source

(hν = 1486.7 eV). The spectra were collected after sputtering for 5 minutes using 1 keV Ar-ions to remove surface oxide. Fourier transform infrared (FTIR) spectroscopy was performed using a ThermoElectron Nicolet 4700 spectrometer with Ge attenuated total reflectance setup and a mercury cadmium telluride (MCT) detector to probe the various vibrational bonding structures within the SRN thin films.

## 5.3 Results

The room temperature PL measurements were performed on the as-deposited and annealed samples of the SRN (N00, N20, and N60) in order to understand the origin of the photoluminescence. In Figure 5.1 (a-c), the as-deposited spectra of N00, N20, and N60 exhibit only a very weak PL signal. Our previous report of SRN grown by low pressure chemical vapor deposition (LPCVD) had demonstrated a visible PL emission from as-deposited films [120]. It has also been reported that as-deposited silicon nitride samples prepared by plasma enhanced chemical vapor deposition (PECVD) were luminescent under certain laser powers, and the peak energies could be tuned via varying the deposition conditions [121]. In the present study, however, a photoluminescence peak was only visible after the samples were annealed at high temperature. In each sample, the peak intensities gradually increased with increasing annealing temperature from 900 °C to 1100 °C. Additionally, the luminescence from the N00 sample had the highest intensity while the PL intensities decreased as the excess Si concentration was increased. The peak positions also shifted to higher wavelength (lower energy) from N00 to N20 to N60.

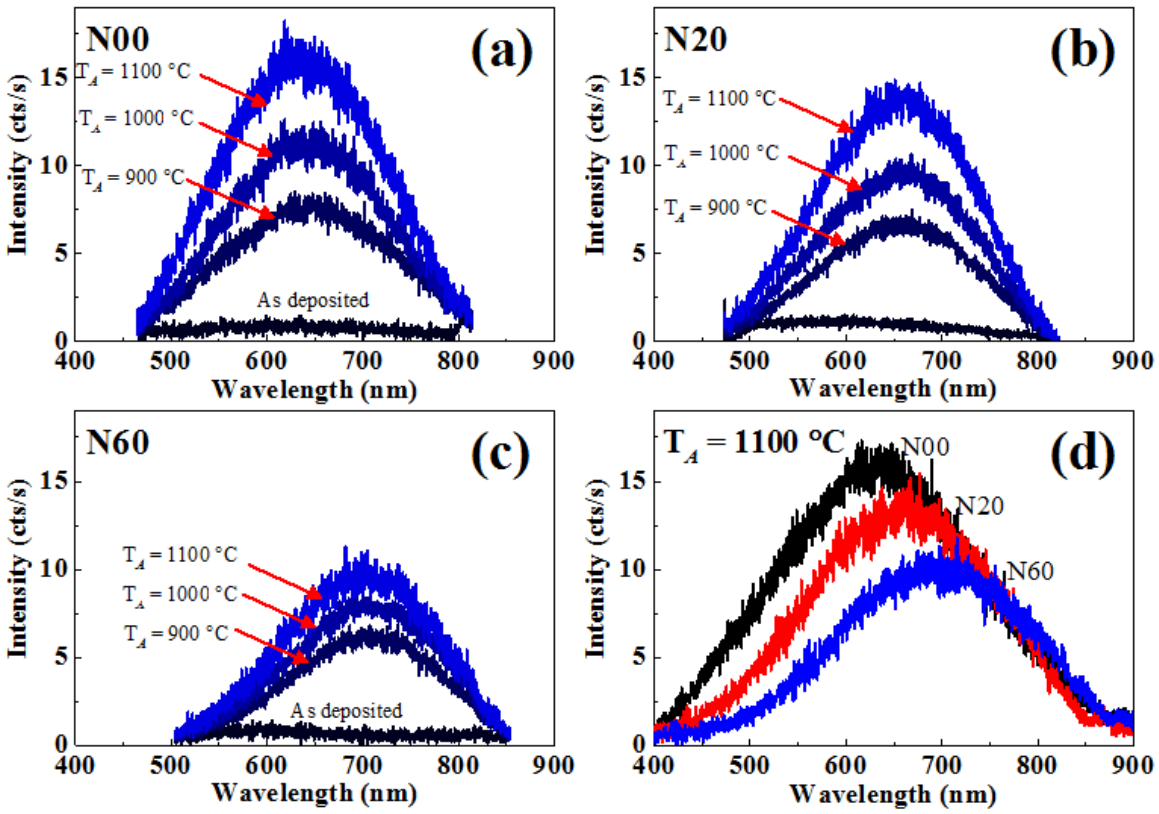


Figure 5.1. The photoluminescence (PL) spectra of (a) N00, (b) N20, and (c) N60 at various annealing temperatures. The PL intensity increases as annealing temperature increases. (d) PL spectra of N00, N20, and N60 after anneal at $T_A$ = 1100 °C. The PL peak shifts to higher wavelength as the Si concentration increases due to composition-dependent band edge shifts.

The time resolved PL was measured with a filter centered at 680 ± 40 nm. In Figure 5.2, the TRPL spectra for the N60 samples show very fast decaying components for different annealing temperatures. The decay curve can be fitted using an exponential function,

$$I(t) = \left[ I_i \exp\left(-\frac{t}{\tau_i}\right) \right]_n$$

where, $\tau$ is the decay constant.

The as-deposited sample is fit using a single exponential function whereas the $T_A$ = 900 °C, 1000 °C and 1100 °C were all fitted using a double exponential. The decay time constants and their respective amplitudes for the N60 samples are presented in Table 5.1. Similar values were

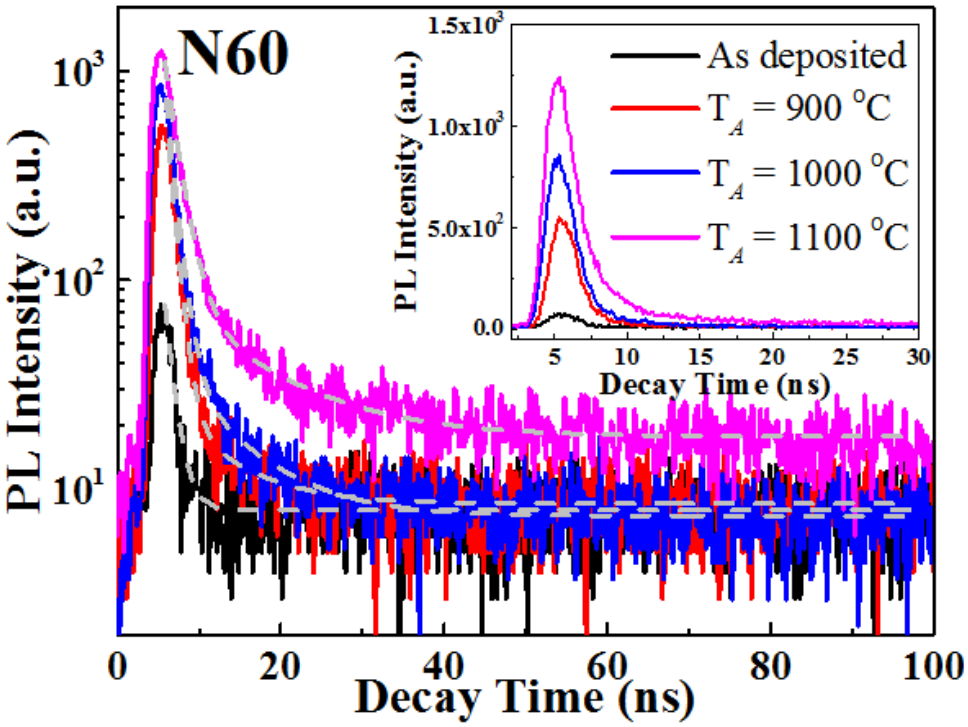


Figure 5.2. The time resolved photoluminescence (TRPL) spectra collected from sample N60 at 680 ± 40 nm. (Inset) The same data in linear scale. The dotted line represents the fitting of the spectra. The fit parameters are listed on Table 3.1 **Error! Reference source not found.**.

also obtained for the N00 and N20 samples. Since the decay time constants are on the order of nanoseconds, it is likely due to non-radiative decay associated with a defect state within the silicon nitride, a similar conclusion to that of Dal Negro *et al.* [83]. The decay associated with $\tau_1$ in every sample is the dominant mechanism with over 99% of the signal coming from that mechanism.

Table 5.1 Decay constants and their respective amplitudes for sample N60 extracted from the fits to the time resolved PL spectra.

| | $\tau_1$ (ns) | Amplitude, $I_1$ | $\tau_2$ (ns) | Amplitude, $I_2$ |
|---|---|---|---|---|
| **As deposited** | 1.09 ± 0.05 | 67.92 ± 1.98 | | |
| **$T_A$ = 900 °C** | 0.92 ± 0.02 | 422.80 ± 3.74 | 7.03 ± 1.42 | 15.34 ± 3.26 |
| **$T_A$ = 1000 °C** | 1.09 ± 0.01 | 689.47 ± 3.76 | 7.74 ± 0.79 | 30.87 ± 3.41 |
| **$T_A$ = 1100 °C** | 1.52 ± 0.02 | 1120.60 ± 6.0 | 10.74 ± 0.91 | 63.18 ± 5.42 |

XRD spectra was collected at a grazing incidence (GI) angle Ω = 0.5° with a scan speed of 1°/min. The substrate influence was avoided by rotating the sample stage by $\phi$ = 30° [122]. In Figure 5.3, the evolution of the crystalline Si peaks is shown for the as-deposited and annealed samples of N60. It is noted that higher temperature yields a higher concentration of crystalline Si in the film as expected. The (111), (220) and (311) peaks are visible at 28.3°, 47.5° and 55.9°,

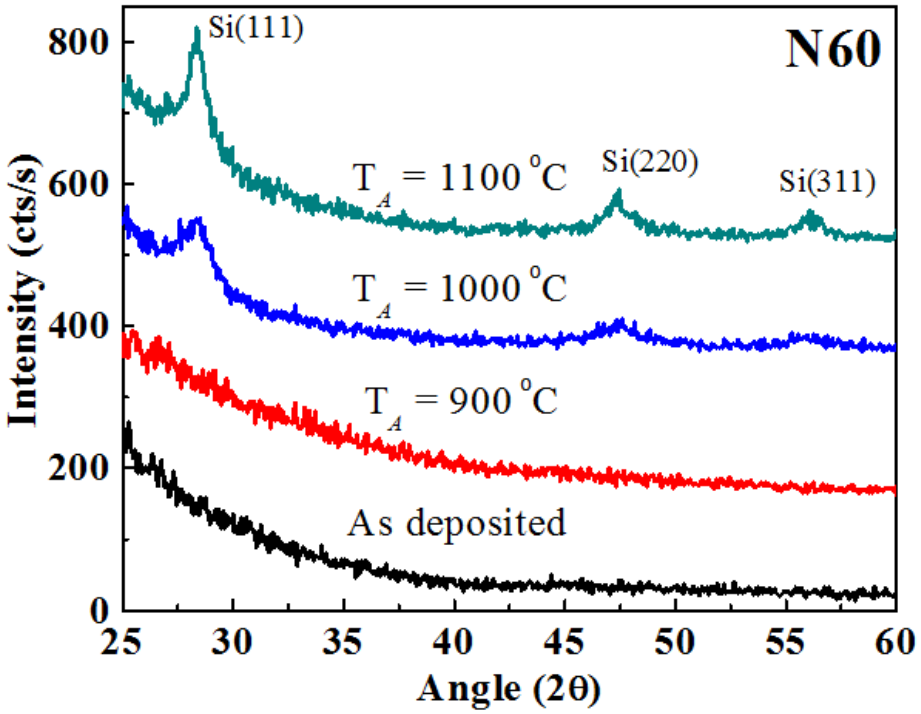


Figure 5.3. The GI-XRD spectra collected at Ω = 0.5° for N60 as-deposited and after the various high temperature anneals. Higher temperature annealing causes the excess Si in the SRN to crystallize into Si-NC, as confirmed by the peaks appearing at 28.3°, 47.5° and 55.9°.

respectively, after the sample was annealed at 1000 °C and the intensity of the peaks further increases after the 1100 °C anneal. From Scherrer's formula [58], an estimated average size for the formed Si quantum dots was calculated to be ~5 nm in diameter for the 1100 °C annealed N60 sample. Since no peaks were observed at 900 °C for N60 or in any annealed samples of N00 or

N20 (not shown), the concentration of crystalline Si QDs is below the ~2% detection limit of XRD [59] for those samples.

To further investigate the formation of the Si nanocrystals, Raman was performed and analyzed. In Figure 5.4, the Raman spectra collected from sample N60 deposited on silica (to eliminate crystalline Si peaks from the substrate) is shown. After annealing at 900 °C, a broad

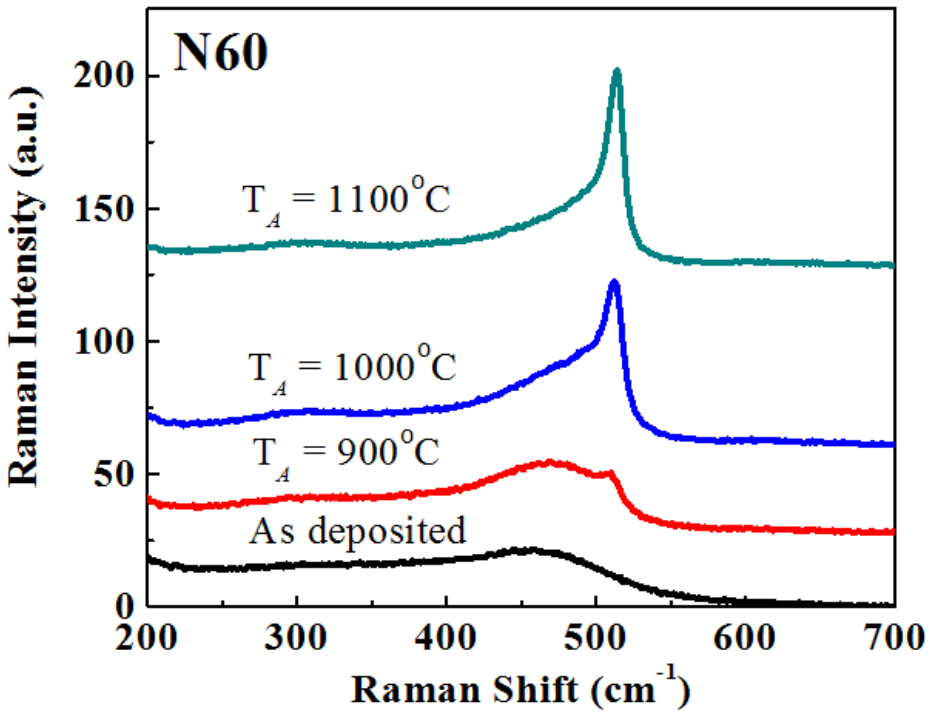


Figure 5.4. The formation of Si-NC is confirmed in Raman spectra for sample N60 after high temperature anneal. With increasing annealing temperature, amorphous Si (peak at 480 cm$^{-1}$) transforms into crystalline Si (~514 cm$^{-1}$).

shoulder at 480 cm$^{-1}$ was visible, which is the transverse optical (TO) mode associated with amorphous Si [77]. At 1000 °C, the TO mode of nanocrystalline Si appears as the additional sharp peak at 514 cm$^{-1}$ [123]. At 1100 °C, most of the amorphous Si has crystallized, although an a-Si shoulder is still detected. The Raman spectra further confirms the formation of Si-NC within the nitride matrix.

Figure 5.5 shows the Si 2*p*, N 1*s*, and O 1*s* XPS spectra of N00, N20, and N60, before and after annealing at 1100 °C. The spectra were fitted using Voigt line shapes in conjunction with a Shirley background subtraction. Detailed peak fitting of the Si 2*p* spectra before annealing shows three distinct peaks. The peaks centered at 99.6 eV and 103 eV correspond to Si–Si (amorphous

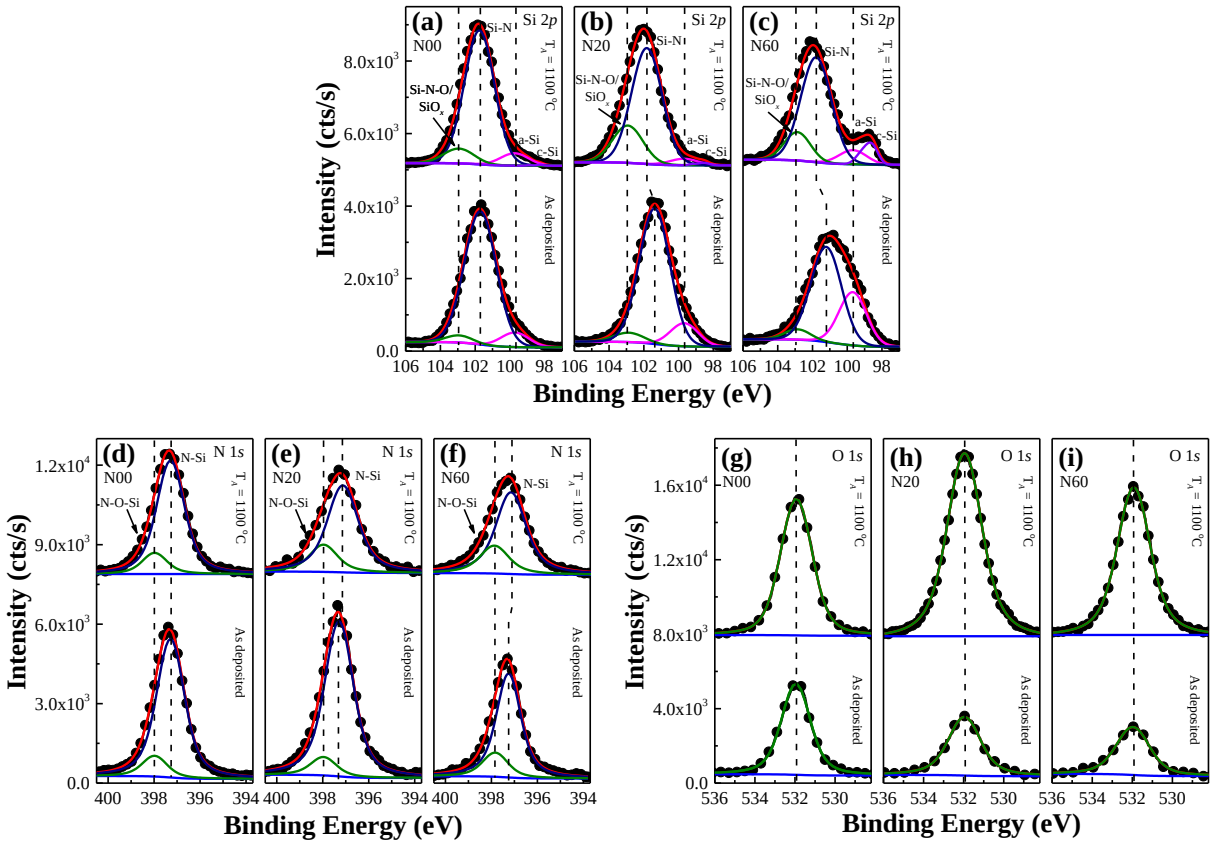


Figure 5.5. XPS of the SRN samples N00, N20, and N60 before and after anneal. The Si 2*p*, N 1*s*, and O 1*s* regions are shown in separate panels for all three samples. An increase in oxygen related bonding after high-temperature anneal correlates with the increase in PL intensity. In sample N60, the crystalline Si peak associated with Si-NC is also observed after anneal above 1000 °C.

Si) and Si–N–O type bonding, respectively, and do not shift after annealing. The central peak between 101.7 eV to 101.2 eV is a Si–N bond, which is expected for a $SiN_x$ type film [124]. Also, as expected, the Si–N peak in the Si 2*p* spectra shifts towards lower binding energy as the Si concentration increases. After annealing however, the Si–N peaks shift to ~101.8 eV, forming a

more stoichiometric $Si_3N_4$-like bonding [125]. A fourth peak was used to fit the spectra for the annealed samples at ~98.6 eV which is consistent with the formation of crystalline Si (c-Si) that forms during the high temperature anneal. In N00 and N20 this peak has a small contribution. However, in N60 the peak is clearly distinguishable and is consistent with the XRD and Raman data. The intensity of the amorphous Si (a-Si) peak decreases after annealing due to its conversion to c-Si. The N 1*s* spectra in Figure 5.5 (d), (e), and (f) were fitted using two peaks, one at 398.0 eV related to N–O–Si bonding, which does not shift after anneal. The second peak at ~397.3 eV is related to the N–Si bond and is observed to shift to lower binding energy with increasing Si concentration confirming that the films are Si-rich.

As mentioned previously, the Si/N ratios determined from XPS peak fitting were 1.07, 1.08, and 1.52 for N00, N20, and N60 samples, respectively (with ±10% experimental error). Although this suggests similar levels of silicon content in the N00 and N20 samples, the higher silicon content of N20 compared to N00 can be demonstrated by calculating the binding energy separation: $\Delta B.E = \mathrm{B.E}_{\mathrm{N}\ 1s} - \mathrm{B.E}_{\mathrm{Si}\ 2p}$ for the $SiN_x$ related features in the as-deposited samples. Using the above formula, we obtain $\Delta B.E$ values of 295.6 eV, 295.9 eV, and 296.05 eV for N00, N20, and N60. This consistent increase in the peak separation confirms the increase in Si content. As the $SiN_x$ matrix becomes more Si-rich, the Si 2*p* peak shifts to lower binding energy (closer to Si–Si bonding), while the N 1*s* peak shifts to higher binding energy (closer to N–N bonding). This confirms that N20 has a higher silicon content than N00.

The presence of oxygen is evident in the O 1*s* spectra in Figure 5.5 (g), (h), and (i), which is close to the binding energy of O–N–Si bonding [126]. The oxygen after sputtering in the XPS is not from the surface, but from the bulk of the film. Oxygen is incorporated in the as-deposited

films due to the base pressure in the sputtering chamber, which was $5\times10^{-7}$ Torr during loading ($4\times10^{-3}$ Torr during deposition), high enough to contain residual oxygen as seen in other reports [127]–[129]. The oxygen concentration is low for the as-deposited films, but increases after annealing. Despite annealing in $N_2$ (with 99.9998% purity), it is still possible for the films to partially oxidize at elevated temperatures since the majority of the impurities in the gas are oxygen containing species [130], with an effective flow rate of ~9 $cm^3$/min for an $N_2$ flow rate of $4.5\times10^3$ $cm^3$/min. The oxidation rate increases at higher annealing temperatures [131], thus resulting in the observed growth of the Si–O–N peak. The oxygen is 1.58, 3.48 and 3.76 times higher in the annealed sample than the as-deposited sample for N00, N20 and N60, respectively. With excess Si, more oxygen is incorporated into the films after anneal as the Si is more susceptible to oxidation compared to silicon nitride [132].

The FTIR spectra in Figure 5.6 compares the samples annealed at 1100 °C to the as deposited samples, and shows the region where the Si–N, Si–O–N, and Si–O stretching absorption modes are strongest in silicon nitride. The two distinct peaks at 820 and 870 $cm^{-1}$ are characteristic Si–N bands [96]. The spectra have been normalized to the Si–N peak intensity to enable a better comparison of the change in oxidation behavior as a function of increasing excess Si-content. The peak at ~750 $cm^{-1}$ is due to a Si-rich silicon nitride [133] and the increase of this peak as a function of increasing excess Si (from N00 to N60) is consistent with the deposition conditions and the XPS spectra. The features at ~900 $cm^{-1}$ and 1100 $cm^{-1}$ are due to Si–O–N [134] and Si–O (in $SiO_2$) modes, respectively. In the as-deposited samples both of these peaks have a low intensity.

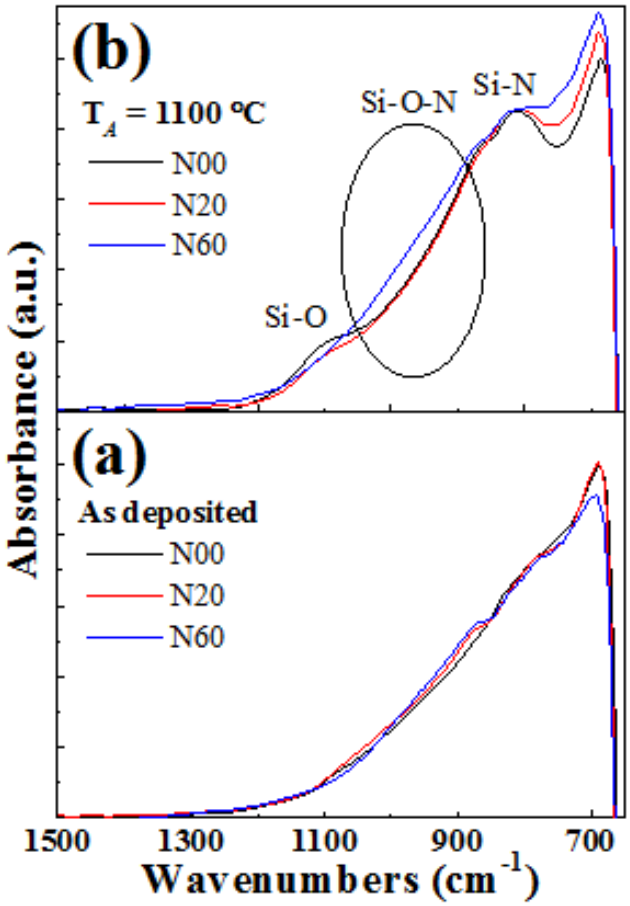


Figure 5.6. The FTIR spectra of N00, N20, and N60 samples (a) as deposited and (b) after annealing. All spectra were normalized to the Si-N feature at 820 $cm^{-1}$.

However, after annealing at 1100 °C, the N00 and N20 samples show an increase primarily in the Si–O peak at 1100 $cm^{-1}$, while N60 (the only sample that formed Si-NC) shows an increase primarily in the Si–O–N feature. In the N00 and N20 samples, Si-NCs do not precipitate fully and the amorphous Si (precursor to Si-NCs) oxidizes during the anneal forming Si–O (some additional Si–N–O is also formed due to oxidation of the matrix). Additionally, the peak position is at lower wavenumbers than that for stoichiometric $SiO_2$, indicating a substoichiometric $SiO_x$ bonding. This is consistent with the XPS spectra of Figure 5.5 (a) and (b) where the decrease of the amorphous Si peak and the increase in the $SiO_x$ peak are observed. The excess Si in the N60 sample

conversely, almost fully precipitates into Si-NCs from the nitride matrix and any $SiO_x$ that may have formed as an intermediate step. Following precipitation, the oxygen in the films introduced during the anneal interacts almost exclusively with the nitride matrix, forming Si–O–N rather than $SiO_2$. The intensity of the detected spectra drops off beyond 690 $cm^{-1}$ due to a loss of detector sensitivity.

## 5.4 Discussion

From XRD, Raman, and XPS, it is evident that the N60 sample had partial formation of Si-NC after anneal at 1000 °C which further increased at 1100 °C. N00 and N20 showed no detectable crystallized Si in XRD or Raman (not shown), yet all three samples exhibited photoluminescence upon anneal. Therefore, the PL cannot be exclusively (nor even primarily) due to Si-QDs. In fact, the fast decay observed in the TRPL spectra indicates that there is no detectable contribution from the Si-QDs.

The increase in the oxygen content after annealing as revealed by XPS and FTIR indicate that the films contain silicon oxynitride which can introduce new defect sites to the film. Augustine *et al*. [135] reported the presence of defect states in PECVD silicon oxynitride films arising from a silicon suboxide component. Although they did not specify the physical nature of defect states, they linked oxide related defects to the PL intensity increase with increasing annealing temperature. The ESR measurements performed on $SiO_xN_y$ films have revealed additional defect states beside the *K* and the *N*-centers [136]–[138]. There are point defects due to the oxygen bonded with an unpaired Si atom ($O_3{\equiv}Si{\bullet}$) known as the $E'_s$ center, which is located energetically near midgap in $SiO_xN_y$ [139], [140]. Similarly, the non-bonding oxygen hole center, $E'_\gamma$ ($\bullet O\text{-}Si{\equiv}O_3$) is another defect in $SiO_2$ that is close to the valence band edge [139], [140]. A

defect exclusive to the oxynitride film, the $N_x$ center, was identified by Cros et al. [136], which increased as the films became more oxygen rich. The $N_x$ center is due to a ≡Si–N•–O or =N•–O like bonding [137].

In addition to the O-related defects, numerous reports have suggested that the presence of defect states known as the *K*-center and *N*-center act as luminescence centers in $Si_3N_4$, which have been attributed to fast decay in PL [76], [81], [141]. The paramagnetic *K*-center, ($K^0$) is due to a Si dangling bond (Si back bonded to three N neighbors, N≡Si•) and is the predominant defect state in $Si_3N_4$. The $K^0$ center was calculated to be near midgap of $Si_3N_4$, similar to the $E'_s$ center, whereas the *N*-center (•N=Si) was found to be 0.5 eV above the valence band [137]. Typical concentrations of *K*-center densities measured using electron spin resonance (ESR) were found to be on the order of ~$10^{17}$ $cm^{-3}$ whereas in higher temperature annealed samples, this increased to ~$10^{18}$ $cm^{-3}$ [141], [142]. The energetic positions of the *K*- and *N*-centers, with respect to vacuum, are believed to be fixed, regardless of the film stoichiometry. The *N*-center likely lies below the valence band edge for Si-rich nitride films [143], so this cannot contribute to the observed PL in our films. While the *K*-center may have some contribution to the PL, the dramatic increase in PL signal and oxidation after annealing indicate that O-related defects are the dominant mechanism.

Defects associated with a-Si are also possible and have been detected previously close to midgap in the a-Si bandgap [144] (close to the energetic position of the $E'_s$, $N_x$, and $K^0$-centers). However, the trend in intensity of the a-Si peaks in the spectroscopic measurements is opposite to that observed in the PL. The strong increase in PL correlates with the increase in oxygen related features in the XPS and FTIR, indicating that the $E'_s$ ($O_3$≡Si$^{\bullet}$) and $N_x$ (≡Si–N$^{\bullet}$–O or =N$^{\bullet}$–O) centers are the likely culprits, and no significant contribution from the Si nanocrystals.

With the PL correlating to transitions to and from defects and not from QD-related radiative emission, the shifts in the PL energetic peak positions, observed in Figure 5.1 (d), cannot come from changes in the QD size. The shift in the PL energy can be explained due to the change in the relative positions of the composition dependent Si-rich $Si_3N_4$ matrix band edges [138]. With these composition-dependent band edge shifts and assuming the defect states, $E'_s$ and $N_x$, are fixed in energy with respect to vacuum, the transitions occurring to or from the defect states to the band edges of the nitride matrix will shift as a function of Si concentration. This is precisely what we observe, and the shifts are consistent with the reduction in matrix bandgap with increasing Si content. The drop in the PL intensity (from oxide-related defects) with increasing Si concentration (Figure 5.1(d)) is consistent with the decrease in the relative amount of silicon-(oxy)nitride within a unit volume.

## 5.5 Conclusion

Si-nanocrystals were formed in co-sputtered Si-rich silicon nitride films after a high temperature anneal, and their presence was confirmed by XPS, XRD, and Raman. A partial crystallization of the excess Si was observed in the N60 sample at 1000 °C and higher. The photoluminescence detected from these films could not be correlated with radiative transitions from the quantum confined states as the decay times from TRPL were several orders of magnitude faster than the typical indirect bandgap quantum dot. Following the standard process flow for Si-NCs in silicon nitride, the films were found to contain some oxygen which increased following a furnace anneal in $N_2$, as measured by XPS and FTIR, resulting in the formation of silicon oxynitride. The correlation between the PL intensity and oxygen related chemistry in spectroscopy indicates that the observed PL is almost exclusively from oxygen related defect states.

Additionally, the shift in the PL energy as a function of increasing Si content is simply a result of the change of the silicon nitride bandgap.

# CHAPTER 6

# EFFECT OF OXIDATION ON THE RESIDUAL STRESS OF SILICON CARBIDE

## Participation

The sample preparation and stress measurements were performed by Felix Deku. The FTIR and XPS measurements and analysis were performed by myself. Useful discussion and contributions were provided by Dr. Alexandra Joshi-Imre and Dr. Jimin Maeng from Dr. Stuart Cogan's group.

## 6.1 Introduction

Amorphous silicon carbide (a-SiC) thin-film dielectric coatings have emerged as a promising approach to the encapsulation of implantable biomedical devices [48]–[51]. SiC thin films have excellent barrier properties and resilience against adverse chemical conditions [145]. They are electronically resistive, resistant to corrosion [146], and well-tolerated in the cortex [48], [147]. They have a lower dissolution rate at 37 °C in phosphate buffered saline (PBS) than silicon nitride [48]. Also, they are hemocompatible and have been evaluated clinically as coatings for coronary stents [148].

As a thin film dielectric insulation, a-SiC is required to exhibit excellent barrier properties including low water vapor transmission rate, low leakage current, and minimal-to-no pinholes within the film. Although otherwise inert, due to the presence of weakly bonded hydrogen atoms, the carbide surface could oxidize to a few nanometers when exposed to ambient air [149]. The reaction kinetics has been shown to increase in films with increasing carbon and hydrogen compositions [150]. Mastelaro *et al*. [151] reported the presence of micro-voids in a-SiC films where films with higher void densities showed evidence of higher oxidation when exposed to air

over time. Controlling the chemical composition of amorphous dielectric coatings is thus necessary to achieve robust and long-term encapsulation reliability.

Plasma-enhanced chemical vapor deposition (PECVD) is widely used in the deposition of a-SiC (i.e., a-SiC:H) thin films due to its advantages including low-temperature deposition and precise residual stress control. The properties of PECVD a-SiC:H films could be tailored by regulating the deposition parameters such as power density, temperature, gas ratio, pressure as well as He or Ar dilution of the reactive gas [152]–[157], or by annealing at elevated temperatures post deposition [158].

It has been proposed that the compressive intrinsic stress arises in a-SiC:H films due to the incorporation of hydrogen atoms into the Si–C bond [159]. Other impurities such as oxygen and water vapor have been shown to produce compressive stress in other thin-films such as aluminum [160] and silicon monoxide [161]. Although most studies have correlated the change in residual stress of a-SiC films to deposition and ambient conditions, there are no reports on the temporal change of the film stress and its relation to the change in chemical bonding of the film due to environmental effects.

In the present study, the temporal change of residual stress in PECVD a-SiC:H films exposed to air and wet ambient were investigated. The correlation between film oxidation and stress change, along with the effects of different deposition temperature and power, were examined. X-ray photoelectron spectroscopy (XPS) and Fourier transform infrared (FTIR) analyses was carried out to understand the root cause of the stress variation over time in these films. Evidence of the films reacting with oxygen and water vapor from ambient environments are

presented. This study provides a useful progress toward low-stress and long-term SiC dielectric coatings for chronic implantable medical devices.

A second study was conducted on a-SiC to lower the deposition temperature to expand the range of applications to medical devices. It was found that by increasing the deposition power, the films deposited at lower temperature may have a reduced oxidation effect over time.

## 6.2 Experimental

**SiC film deposition.** Amorphous SiC:H thin films were deposited using a PlasmaTherm Unaxis 790 series PECVD system. The depositions were carried out on 100-mm Si (100) prime grade wafers along with double-sided polished (DSP) high resistivity Si wafers for FTIR measurements. A set of films were deposited at different temperature, ranging from 150 to 350 °C, at a fixed power density of 0.27 $Wcm^{-2}$. Another set of films were deposited at different power densities, ranging from 0.05 $Wcm^{-2}$ to 0.32 $Wcm^{-2}$, at a fixed temperature of 350 °C. For all depositions, a $SiH_4$:$CH_4$ gas ratio of 1:3 was used. The chamber was maintained at a pressure of 1000 mTorr with an Ar gas flow rate of 800 sccm during the deposition. The deposition time was kept constant for all depositions targeting a nominal thickness of ~1 μm.

**Sample storage and monitoring.** The a-SiC:H films were stored on a lab bench in air ambient at room temperature. The stress variation in these films was monitored once every 7 days over a period of 28 days. A different set of films were exposed to various ambient medium including dry air (7 ppm of $H_2O$), deionized (DI) water, $N_2$ (99.998%), and $O_2$ (99.994%). The stress variation in these films was monitored for 24 hours.

**SiC film characterization.** The film thickness was measured using a Nanometric NanoSpec 6100 analyzer. Data were collected from 20 different points randomly across the wafer

and the average values were recorded. The film stress was measured using a Toho Technology FLX-2320 system. The stress values were estimated based on changes in the radius of curvature of the silicon wafer due to the deposition of the a-SiC: H thin-film using Stoney equation [162]. XPS analyses were performed using a PHI VersaProbe II spectrometer equipped with an Al *Kα* monochromated X-ray source (h$\nu$ = 1486.7 eV). Prior to the spectra collection, the samples were pre-sputtered with 1 keV Ar ions for 10 minutes to remove surface oxide. FTIR analyses were performed using a ThermoElectron Nicolet iS50 spectrometer with a deuterated triglycine sulfate (DTGS) detector. The spectra were collected at a resolution of 4 $cm^{-1}$.

## 6.3 Results

### 6.3.1 Stress Variation Over Time

The residual stress of the a-SiC:H films is monitored over a period of 28 days in air exposure. Figure 6.1(a) illustrates the results from the films deposited at various temperature ranging from 150 to 350 °C at a fixed power density of 0.27 $Wcm^{-2}$. As recognized in other studies

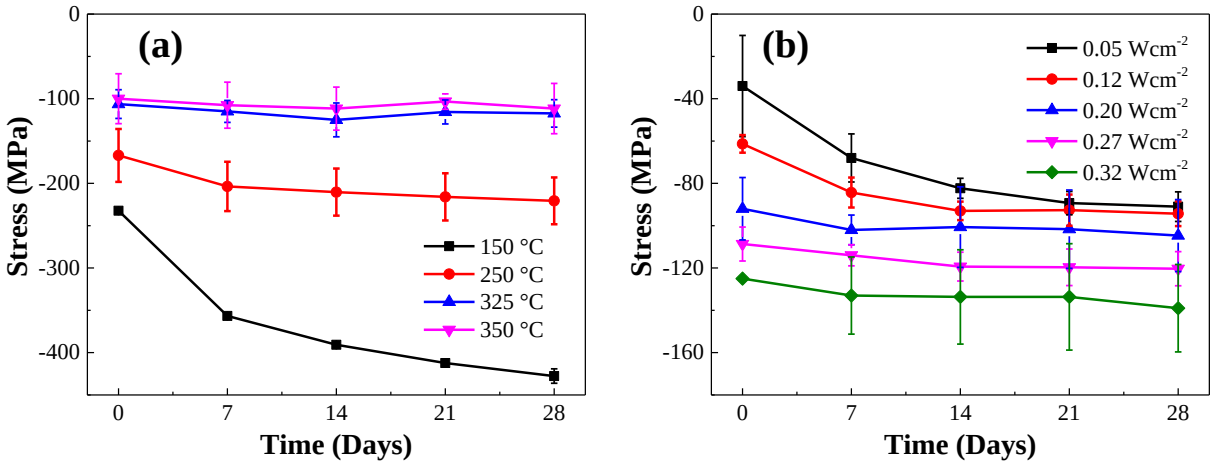


Figure 6.1. Residual stress in air-exposed a-SiC:H films deposited at (a) various temperature and (b) various power densities, monitored over a period of 28 days.

[157], the intrinsic compressive stress of the as-deposited films is shown to be lower when deposited at higher temperature (-230 MPa for $T_D$ = 150 °C and -100 MPa for $T_D$ = 350 °C). In the films deposited at $T_D$ = 325 °C and 350 °C, the stress remains almost invariant over 28 days at approximately -100 MPa. Unlikely, an abrupt increase in the compressive stress occurs in the low-temperature films during the initial 7 days; the stress changes from -163 to -203 MPa (24.5% increase), and from -226 to -356 MPa (57.5% increase), in the films deposited at $T_D$ = 250 °C and 150 °C, respectively. The compressive stress keeps increasing over time until Day 28. Figure 6.1 (b) shows the results from the films deposited at various power densities ranging from 50 to 320 W (0.05 to 0.32 $Wcm^{-2}$) at a fixed temperature of 350 °C. The intrinsic compressive stress of as-deposited films is shown to be higher when deposited at higher power (-35 MPa for 0.050 $Wcm^{-2}$ and -125 MPa for 0.32 $Wcm^{-2}$), agreeing well with other studies [157]. It is shown that the power at which the films are deposited also influences the changes in film stress over time; the residual stress remains relatively unchanged in the films deposited at power density equal to or greater than 0.2 $Wcm^{-2}$, while more pronounced changes are observed for low-power deposition conditions. These results clearly suggest that the residual stress in air-exposed a-SiC:H films is prone to change over time, especially when the films were deposited at low temperature or low power.

### 6.3.2 Chemical Bonding Analyses

Chemical bonding analyses were carried out to evaluate the cause of stress change in the air-exposed a-SiC:H films. Figure 6.2 represents the XPS spectra of the films deposited at different temperature. The data are collected after 30 days post-deposition. The spectra were fitted using Voigt line shapes in conjunction with a Shirley background subtraction utilizing “AAnalyzer”

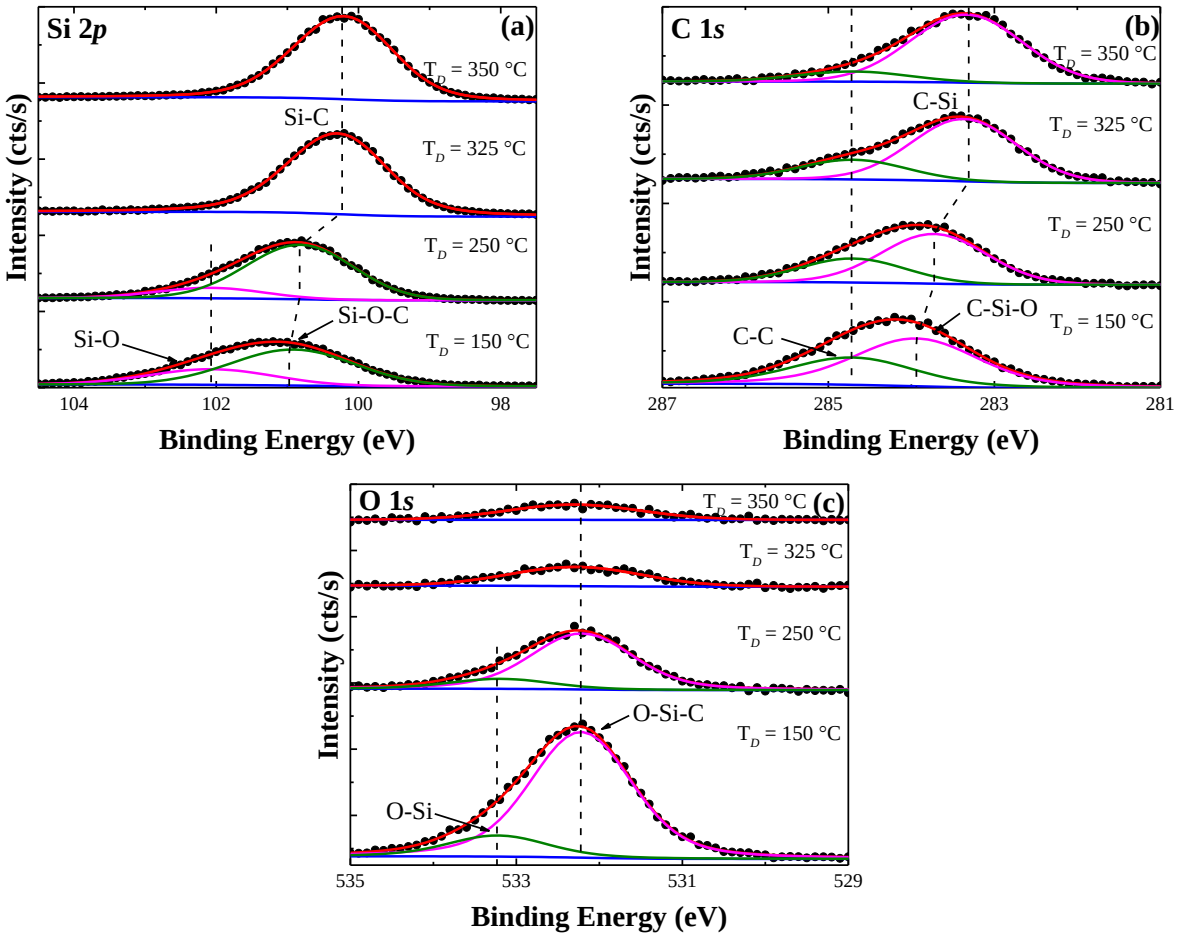


Figure 6.2. XPS spectra of air-exposed a-SiC:H films deposited at various temperature and collected after 30 days post-deposition. The dashed lines represent the peak position of different species in the regions of (a) Si 2*p*, (b) C 1*s* and (c) O 1*s*.

software [88]. Prior to fitting the spectra, the O 1*s* region is charge compensated by centering it at 532.2 eV. The Si 2*p* is fitted using a doublet peak by considering the fact of spin-orbit splitting of the spectrum. The doublet peak represented by a Si $2p_{3/2}$ and Si $2p_{1/2}$ are separated by 0.6 eV and an intensity ratio of 2:1 [163].

The peak position of Si 2*p* spectra in Figure 6.2 (a) is observed to shift to lower binding energy as deposition temperature varies from 150 °C to 350 °C. Both in $T_D$ = 350 °C and 325 °C, the spectra are fitted using a single peak centered at ~100.2 eV. This is characteristics of Si–C peak

[164]. For $T_D$ = 250 °C and 150 °C, the best fits are obtained by fitting the spectra with two distinct peaks. The original peak has shifted to 100.8 eV in the 250 °C sample and further to 101 eV at 150 °C. We identify this peak as Si–O–C bond. This peak position has previously been associated with $SiOC_3$ [165] or $Si_2OC_{2.2}$ [166] bonding, but $SiO_xC_y$ will be used herein as a general notation. The peak at 102.1 eV can be associated with either an O-rich $SiO_3C$ [167] or a sub-stoichiometric $SiO_x$ phase [168]. The oxygen counts are too low to be detected in the Si 2*p* spectra for the samples deposited at $T_D$ = 350 °C and 325 °C and hence no fits could be assigned related to a Si–O peak.

The O 1*s* spectra shown in Figure 6.2 (c) also show very low peak intensities for both 350 °C and 325 °C deposition temperatures, indicating a relatively low rate of oxidation in these two samples as time progressed. The intensity of O 1*s* increases in the 250 °C films and further more in the 150 °C films, indicating a higher rate of oxidation within those two samples. The spectra fitted with two peaks are identified as an O–Si–C bonding at 532.2 eV and an O–Si bonding at 533.2 eV. This also confirms that the peak at 102.1 eV in Si 2*p* is due to a sub-stoichiometric $SiO_x$.

The C 1*s* spectra in Figure 6.2 (b) is fitted using two peaks, namely at 284.7 eV which is due to a C–C or a C–H bonding and does not shift with respect to deposition temperature but increases in intensity as the temperature is reduced. The peak at 283.3 eV in both 350 °C and 325 °C sample is due to C–Si, which correlates with the Si 2*p* spectra. The peak, however, shifts at lower deposition temperature 250 °C and further shifts at 150 °C. It can be related to a C–Si–O peak which compliments the Si–O–C peaks in Si 2*p* due to the oxidation.

Figure 6.3 shows the infrared (IR) absorbance spectra of the silicon carbide films that were deposited on the DSP wafers. The spectra were collected 7 days and 150 days after deposition.

The peaks observed conform to those published in literature [169]–[173]. The peak at 607 $cm^{-1}$ is due to the Si–Si phonon absorption from the substrate [48]. The most intense peak at 785 $cm^{-1}$ has been reported to be the Si–C stretching mode, whereas the peak at ~2100 $cm^{-1}$ arises from the Si–H stretching and various C–$H_n$ stretching at ~2900 $cm^{-1}$ [174]. The shoulder at ~1000 $cm^{-1}$ has been identified as either a Si–$CH_2$ or a Si–O–Si stretching or both [169]–[171].

However, the increase in the intensity of the shoulder, especially in the 150 °C after 150 days, indicates that it is due to oxidation which thereby causes an increase in the Si–O–Si bonding

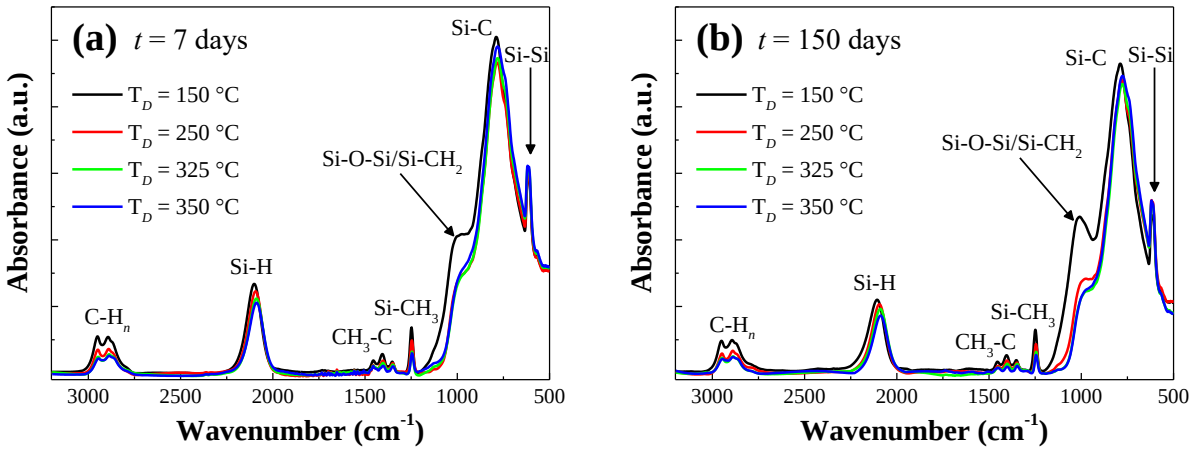


Figure 6.3. FTIR spectra of air-exposed a-SiC:H films deposited at various temperature and collected after (a) 7 day and (b) 150 days post-deposition.

density. This also conforms to the results obtained from the XPS. The sample $T_D$ = 250 °C shows a slight increase in the shoulder at ~1000 $cm^{-1}$ after 150 days, which indicates that the film is oxidizing over time as well. With decreasing deposition temperature, the Si–H stretching at ~2100 $cm^{-1}$ is observed to slightly shift towards higher wavenumber. Jean *et al*. [174] reported that the peak position of Si–H stretch is an indication of the stoichiometry of the SiC films. According to their estimate, the Si/(Si+C) ratio in our films is close to ~0.45. This suggests that these films are slightly carbon-rich. The peak intensity at ~2900 $cm^{-1}$, representing the C–$H_n$ stretching,

indicates the amount of unreacted methyl group in the film. At lower deposition temperature, the amount of methyl group is higher which causes an increase in the peak intensity.

### 6.3.3 Sources of Oxidation and Correlation with Stress Change

It is evident from the results presented so far that low-temperature a-SiC:H films are susceptible to oxidation in air exposure. However, whether this reaction is due to oxygen or water vapor (hydroxyl groups) from the ambient is still not clear. To sort this out, a new set of samples are prepared by depositing a-SiC:H films at 150 °C. They are monitored over a 24-hour time period under exposure to different ambient medium, including ambient air, dry air (7 ppm of $H_2O$), $N_2$ (99.998%), or $O_2$ (99.994%). Some samples are soaked in deionized water (DI water). Figure 6.4 shows the residual stress in the films measured at 4, 8 and 24 hours after exposure to their ambient

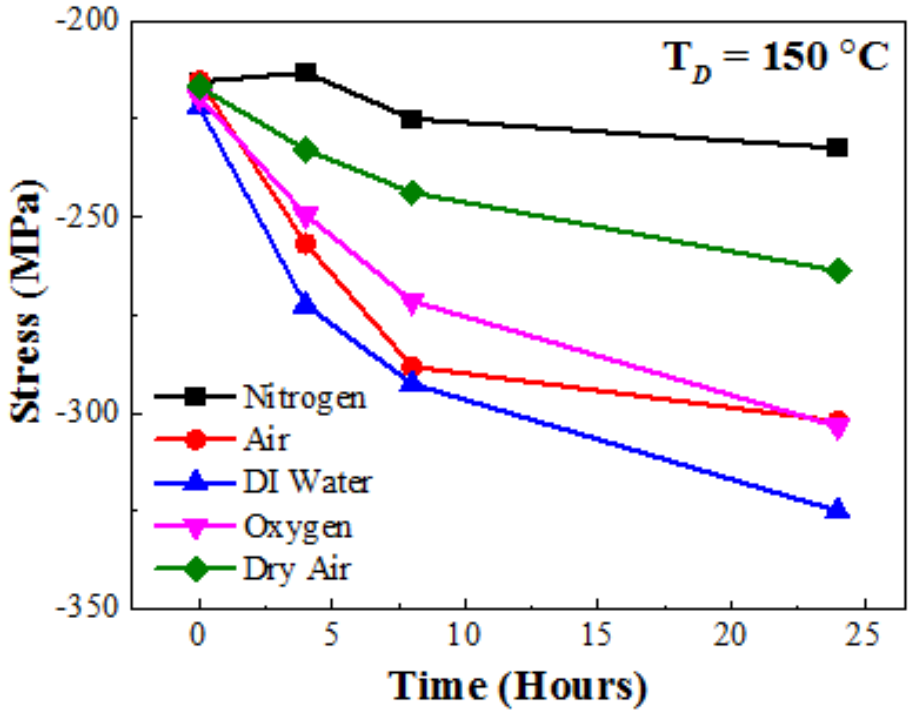


Figure 6.4. Residual stress in a-SiC:H films deposited at $T_D$ = 150 °C under exposure to various ambient environment over a period of 24 hours.

compared to the film stress as-deposited. For the films deposited at 150 °C, residual stress varies only insignificantly under exposure to $N_2$. This indicates that residual stress remains nearly unchanged in the absence of sufficient amount of oxygen or water vapor. On the contrary, an increase in oxygen concentration, as evident in $O_2$ ambient (~100% $O_2$), results in rapid increase in compressive stress. This clearly shows that these films are prone to react with oxygen and that such reaction causes a change in residual stress. A pronounced increase in compressive stress is also observed in air exposure (Air), but less in dry air. The dry air has a similar oxygen concentration but a lower humidity compared to the ambient air. This indicates that not only oxygen but also water vapor reacts with the films and promotes change in stress. This is also confirmed by the observation that soaking the films in DI water, which contains a large amount of oxygen and water vapor, results in the largest oxidative effect and subsequent increase in compressive stress. From these results, it is evident that both oxygen and water vapor are the sources of oxidation as well as a subsequent change in residual stress (increase in compressive stress) in low-temperature a-SiC:H films.

To confirm the correlation between the change in mechanical stress and the chemical bonding in the films, XPS spectra from the newly deposited samples at $T_D$ = 150 °C are collected immediately after deposition. The samples are then exposed to air and measured again after 24 hours, and after 30 days. Figure 6.5 presents the XPS spectra of the individual Si 2*p*, C 1*s*, and O 1*s* regions of the sample collected after each time period. The Si–O bonding in the Si 2*p* increases over time, as expected, confirming that the film is oxidizing. The C–Si–O peak in the C 1*s* spectra, an evidence of silicon oxycarbide ($SiC_xO_y$) formation during or immediately after deposition, is shifted to the higher binding energy over time indicating oxidation in the film.

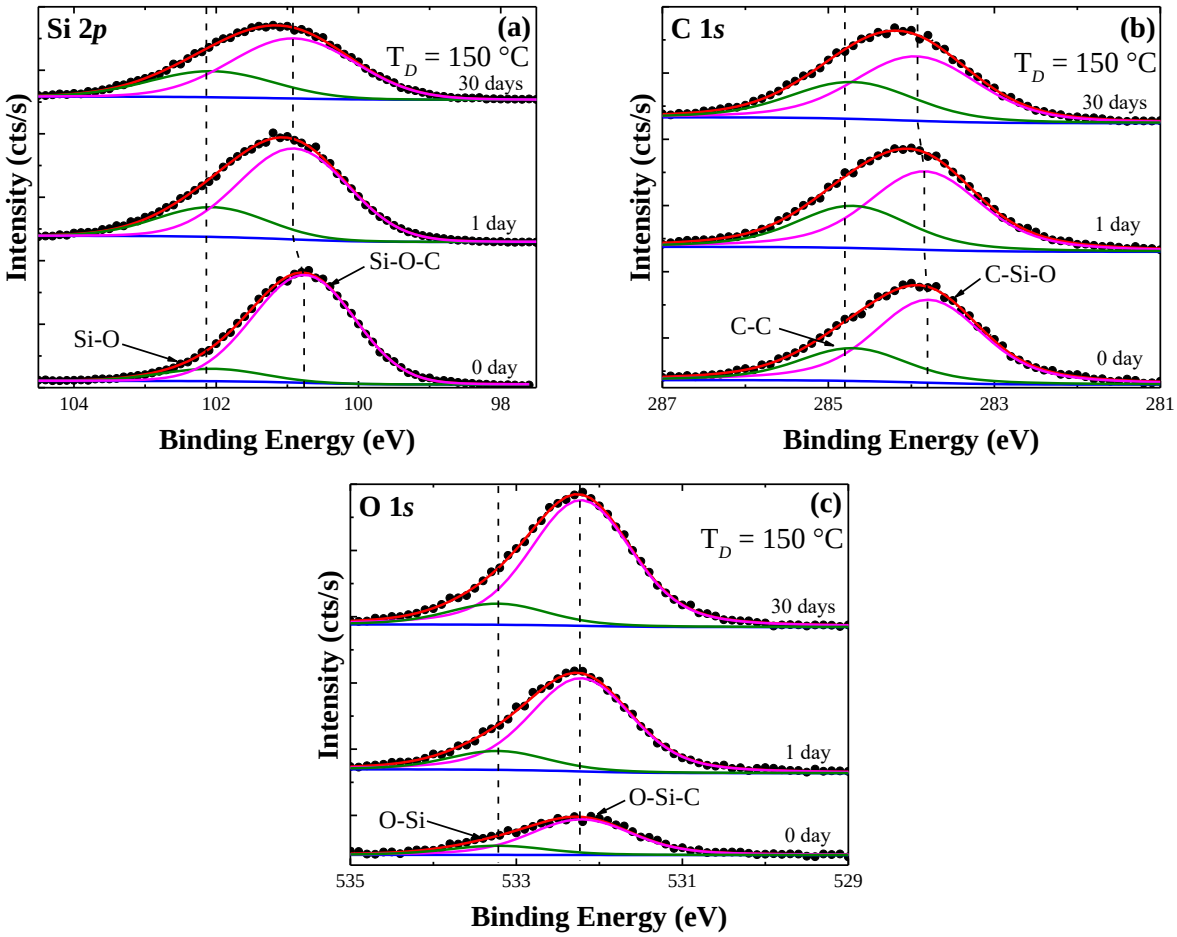


Figure 6.5. XPS spectra of a-SiC:H films deposited at $T_D$ = 150 °C and monitored over a time period of 0, 1, and 30 days. The dashed lines represent the peak position of different species in the regions of (a) Si 2*p*, (b) C 1*s* and (c) O 1*s*.

The O 1*s* spectra show the rate of oxidation with an increase in the peak intensity. The oxygen concentration has doubled within 24 hours after deposition, indicating a higher rate of oxidation. However, the rate of oxidation slows over time as seen from the O 1*s* spectra after 30 days. This shows that the films get oxidized faster soon after deposition as more reactive sites are available to oxygen. As time progresses, the oxidation recedes due to the reduction in the reactive sites in SiC. The temporal increase in compressive stress in the low-temperature films is attributed to the high-weight oxygen molecules into the Si–C lattice.

## 6.4 Discussion

The effects of deposition conditions on the residual stress of as-deposited a-SiC:H thin films have extensively been investigated previously [157], [158]. With increasing interest in a-SiC:H as dielectric coating for implantable medical devices (e.g. neural probes), it is important to understand the long-term reliability of these coatings and how to tailor the deposition parameters to achieve stable dielectric films. This study provides the first comprehensive assessment of the mechanical and molecular characteristics of a-SiC:H films post deposition. Usually, compressive intrinsic stress arises in a-SiC:H films due to the incorporation of hydrogen atoms into the Si–C bond lattice [159]. This is evident from stretch bands associated with Si–H at ~2100 $cm^{-1}$ and C-H at ~2900 $cm^{-1}$ in FTIR spectroscopy [174]. On the other hand, other impurities such as oxygen and water vapor have been shown to produce compressive stress in aluminum [160] and silicon monoxide [161]. It was previously reported that highly porous amorphous SiC, when exposed to oxygen or air ambient, oxidizes faster compared to single crystal SiC [167]. However, the influence of these impurities on residual stress in a-SiC:H films has not yet been reported.

While all the a-SiC:H films prepared in this study show surface oxidation irrespective of deposition conditions, lower-temperature deposited films also exhibit significant subsurface oxidation over time. At higher temperature, there is a complete decomposition of the reactive gases favoring the formation of dense and stable films, hindering the transmission of oxygen and water vapor into the subsurface of the film. On the contrary, the films deposited at lower temperature are highly porous and permit transmission of oxygen and water vapor, resulting in subsurface oxidation over time. A similar argument can also be drawn for the effect of deposition power; at higher power, more energized plasma forms a denser film, resulting in an improved film quality

and thereby reduced oxidation effect over time as shown in Figure 6.1 (b). Highly porous films have large Si-$CH_3$ content [175] and this is evident in the FTIR spectra in Figure 6.3 for low-temperature films.

## 6.5 Stability of Amorphous SiC at Lower Deposition Temperature

With the information obtained after studying the residual stress of a-SiC:H with deposition temperature, it was concluded that the samples deposited at higher temperature (≥ 325 °C) was suitable for stable low-stress films with minimal oxidation effect. However, the focus shifted towards developing a process that would reduce the thermal budget of SiC deposition. In order to coat certain devices with SiC, a lower deposition temperature is desired as the devices and the materials may sustain only up to certain temperatures. Since SiC deposited at 150 °C was oxidizing over time, it was not a suitable choice for depositing SiC on devices that would be implanted for a longer duration in a saline ambient. The a-SiC deposited at 250 °C underwent oxidation over time, but it was still at a lower rate compared to $T_D$ = 150 °C. Also, when investigating the power density dependence on the stress of a-SiC:H films over time (Figure 6.1 (b)), it was observed that the residual stress remained invariant for power densities ≥ 0.2 $Wcm^{-2}$. However, the result was obtained for samples deposited at $T_D$ = 350 °C. The sample deposited at 250 °C with a power density of 0.27 $Wcm^{-2}$ still oxidized over time. Therefore, it was desirable to deposit the material at 250 °C by increasing the power density while keeping all the other deposition parameters fixed. With that of view, samples were deposited at $T_D$ = 250 °C and the three variable power densities selected were 0.27, 032, and 0.37 $Wcm^{-2}$.

The residual stress of the thin films was measured soon after deposition and again monitored after 7, 14 and 35 days. Figure 6.6 represents the change in the residual stress of the three films deposited at 250 °C. The films become more compressive as the deposition power density increases from 0.27 to 0.32 $Wcm^{-2}$. This is similar to what was observed in Figure 6.1 (b) and also reported by Iliescu *et al*. [154]. However, the sample deposited at 0.37 $Wcm^{-2}$ shows a lower compressive stress, and with time although it becomes more compressive, the overall stress was lower than the other two samples. With the limited set of data points, it was not possible to understand the decrease in the residual stress at a higher power density. The stress in all three samples had increased in compression by an amount of ~60 MPa after 35 days. The relative change in the residual stress is still low compared to the samples deposited at 150 °C.

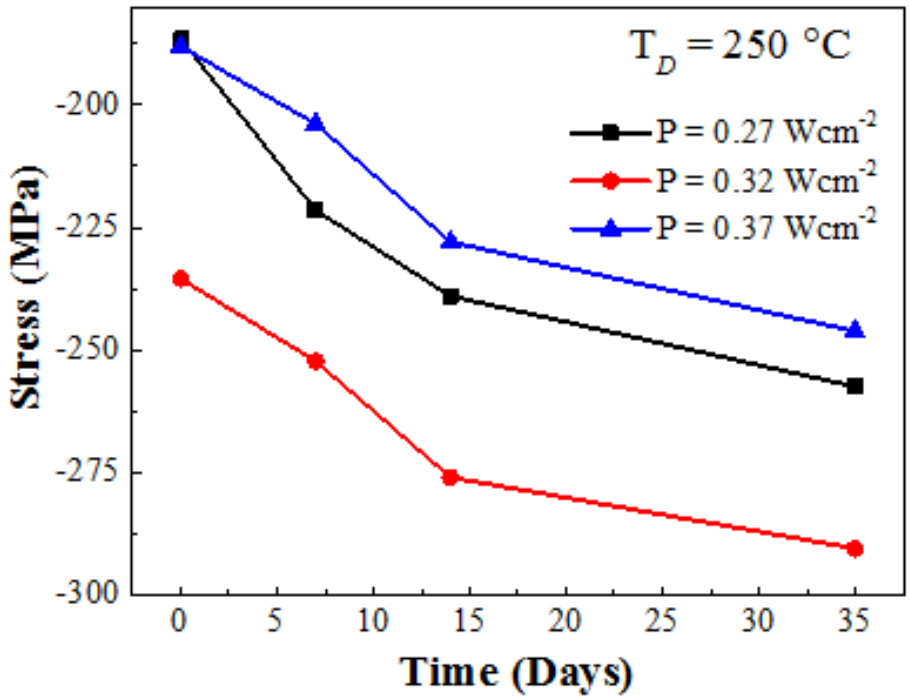


Figure 6.6. Residual stress in a-SiC:H films deposited at $T_D$ = 250 °C with variable power densities and monitored over a period of 35 days.

The FTIR measurement was performed on the samples soon after deposition and consequently after 7 days and 33 days of deposition. The spectral data is presented in Figure 6.7. As noted, no major change in the FTIR peaks observed, especially the shoulder at ~1000 $cm^{-1}$ which was identified as a contribution from the Si–O–Si stretching, had not changed for different power densities or long after deposition. Therefore, no significant oxidation of the films can be observed from the FTIR spectra. The slight increase in the Si–H stretch at ~2100 $cm^{-1}$ with lower power density indicates that there were incomplete reactions of $SiH_4$ present within the film. The

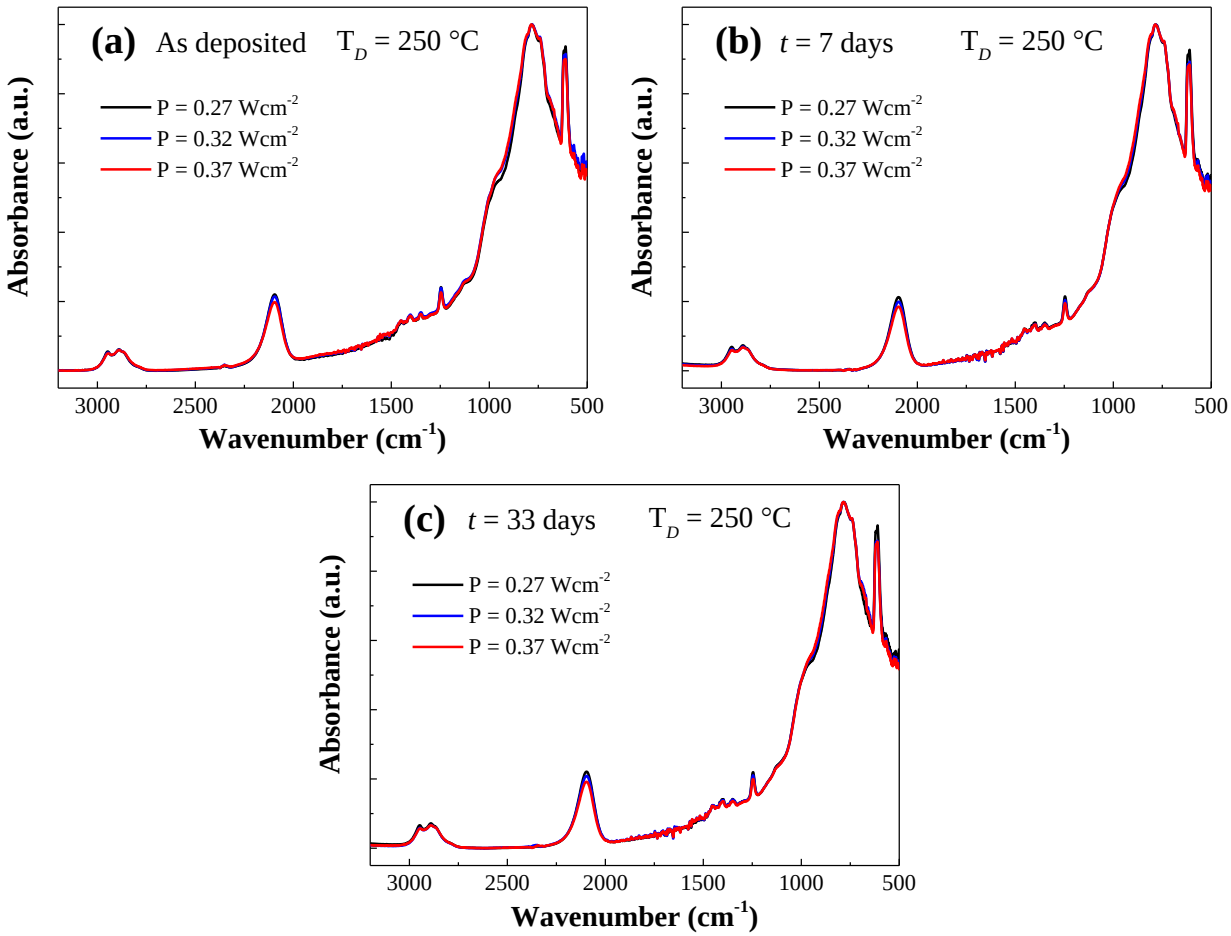


Figure 6.7. FTIR spectra of samples deposited at $T_D$ = 250 °C at various power densities and collected after (a) deposition, (b) 7 days, and (c) 33 days.

FTIR therefore could not correlate with the change in residual stress due to oxidation as it was observed for samples deposited at $T_D$ = 150 °C.

To further investigate the oxidation of the films, the XPS spectra was collected 30 days

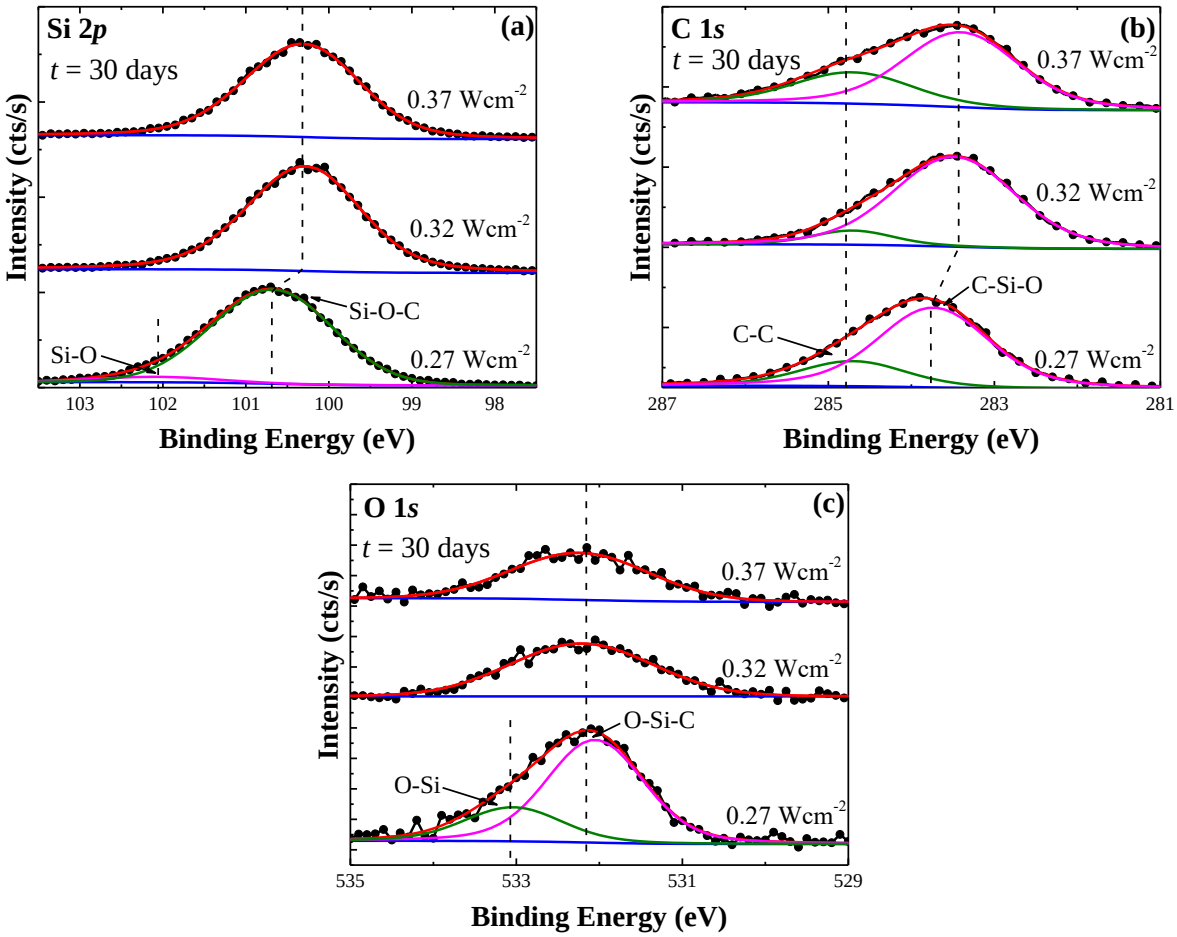


Figure 6.8. XPS spectra of a-SiC:H films deposited at $T_D$ = 250 °C collected after 30 days. The dashed lines represent the peak position of different species in the regions of (a) Si 2*p*, (b) C 1*s* and (c) O 1*s*.

after deposition and analyzed. Figure 6.8 shows the XPS spectral regions of Si 2*p*, C 1*s* and O 1*s* for the samples deposited at different power densities. The samples were sputtered for 10 minutes with 1 keV $Ar^+$ ions prior to collecting the spectra. The Si 2*p* spectra show that for higher power

densities, the films did not oxidize as the Si–C peak position remained at ~100.2 eV. However, at 0.27 $Wcm^{-2}$, the films had oxidized where the Si–C peak shifted to higher binding energy which correlates to a Si–O–C bonding and a second peak at ~102.1 eV appeared indicating the presence of Si–O bonding.

The C 1*s* spectra for the 0.27 $Wcm^{-2}$ sample also show a shift indicating the presence of a C–Si–O bonding. The O 1s spectra further presents the increase in the intensity in the 0.27 $Wcm^{-2}$ sample with an additional peak for O–Si at ~533.1 eV which correlates with the Si–O bonding in the Si 2*p* spectra. The concentration of oxygen in both 0.32 and 0.37 $Wcm^{-2}$ was low enough and was beyond detection in the Si 2*p* spectra.

The XPS results obtained for the 0.27 $Wcm^{-2}$ sample deposited at 250 °C was similar to what was observed previously in section 6.3.2. However, it is fairly evident that by increasing the power density, the oxidation effect can be a minimum for samples deposited at lower deposition temperature.

Although XPS strongly suggests that the films do not oxidize over time that are deposited at sufficiently higher power densities, it is still challenging to correlate the data with the change in the stress, which in the previous sections has been presented to be due to oxidation only. Further investigation is required to better understand the reason other than oxidation behind the change in the stress of these films.

## 6.6 Conclusion

The temporal change of residual stress in PECVD a-SiC:H films exposed to air and wet ambient has been investigated. A close correlation between film oxidation and stress change has been suggested. It is evident from the series of chemical bonding analyses performed in this study

that oxidation of a-SiC:H films is a consequence of the films reacting with both oxygen and water vapor in the ambient. The oxidation rate is shown to be dependent on the oxygen concentration and the amount of water vapor present. It has also been shown that the degree of oxidation in these films is influenced by the deposition conditions. The films deposited at low temperature or power exhibit pronounced increase in compressive stress over time. This is due to an increased rate of transmission of oxygen and water vapor into these porous films. In order to achieve time-invariant low-stress a-SiC:H films, it is important to deposit the films at sufficiently high temperature ($\geq$ 325 °C) and power density ($\geq$ 0.2 $Wcm^{-2}$). These findings will serve as a useful guide for developing SiC-based dielectric coatings for implantable medical devices where thin-film stress management and long-term wet stability are essential.

In addition, the stability of SiC films deposited at lower temperature was investigated. It was suggested from XPS that samples deposited at 250 °C and a sufficiently higher power density ($\geq$ 0.32 $Wcm^{-2}$) does not oxidize over time. A correlation between the change in the residual stress to the effect of oxidation could not be established for these samples, however. For coating devices that can sustain a lower temperature, and which do not require strict stress control, a-SiC can be deposited at 250 °C with higher power and can be used for long term studies with minimal to no oxidation effect.

# CHAPTER 7

# CONCLUSION AND FUTURE WORK

## 7.1 Conclusion

The primary focus of the dissertation was on the deposition and materials characterization techniques of silicon-rich silicon nitride (SRN) films in order to form and identify silicon nanocrystals for an improved light emission efficiency from silicon. Most of the foundation towards improved emission efficiency from Si-based structures was based upon Si-$SiO_2$ systems. However, our interest expanded to Si-$Si_3N_4$ systems due to the lower tunneling barrier of $Si_3N_4$ compared to $SiO_2$. This would have allowed an increase in the electron tunneling probability and more efficient transport of charges, both of which are essential for making electroluminescent and photovoltaic devices.

The initial challenge with SRN samples was the presence of a large number of defects within the film. The defects were primarily studied in SRN samples that were prepared using the LPCVD. Strong visible photoluminescence was observed from as deposited as well as annealed samples, and initially it was assumed that the origin of luminescence may have been from a Si-nanocrystal. However, the fast time decay constant could be correlated to a non-radiative state that was due to intrinsic defects from the nitride. These defects were identified as Si and N dangling bonds which play a significant role in the luminescence of the samples. The stoichiometries were measured using an ellipsometer, and were useful after extracting the bandgap of the material. It was noticed that the LPCVD samples in fact had a dual bandgap of silicon nitride. The PL was deconvoluted and the peak positions were assigned based on the possible transition that may have taken place between the band edges and the defect states. A shift in the PL peak energy was

observed as the films became more Si-rich and was related to the changing bandgap of $Si_3N_4$, not to a quantum confinement effect. Other characterization, namely XPS, FTIR, TEM, Raman and XRD were performed on the samples, which only indicated that the sample were Si-rich nitrides, but no significant presence of the Si-NC could be observed from the as deposited or the high temperature annealed samples.

The next challenge was to form Si-NCs in the $Si_3N_4$ matrix. With that end in view, the RF sputtering was explored as a viable option as it offered room temperature deposition and did not require any dilutant gases. Initially, Si was reactively sputtered with an $Ar/N_2$ mixture to prepare SRN films and annealed at temperatures ranging from 800 °C to 1000 °C. The films were characterized using TEM, which revealed an ordered structure within the $Si_3N_4$ matrix that is an indication of Si-NC. Further confirmation of the Si-NCs were observed from XRD and Raman where the annealed samples exhibited distinct peaks corresponding to crystalline Si. However, when the samples were illuminated under the laser, no detectable PL was observed, indicating that the Si-NCs were not luminescent. Interest then shifted towards developing $Si\text{-}SiO_2$ based materials where the quantum confinement has been extensively studied by other researchers. Si and $SiO_2$ targets were co-sputtered at various power ratios and were annealed at 1100 °C, which exhibited a very strong PL when excited at a low power setting. The width of the PL was narrower which could be fitted using a single Gaussian peak and the TRPL decay had a long component which confirmed that the PL was indeed coming from the quantum dots formed within the $SiO_2$ matrix. Further experimentation was performed with PL at lower measurement temperatures, where the intensity of the PL increased and reached a maximum at liquid nitrogen temperatures. The phenomenon could be related to the radiative transitions originating from the quantum dots.

With the newly found deposition conditions and annealing temperatures that effectively formed quantum dots in $SiO_2$ matrices, the focus then shifted to $Si_3N_4$ again and similar conditions were employed to mimic the results of $SiO_2$. A reference $SiN_x$ sample along with SRN samples were co-sputtered in the chamber and annealed at high temperatures. When excited using the laser, visible PL was observed rising from the annealed samples, including the $SiN_x$ reference sample. The intensity of the luminescence decreased as the Si concentration increased. And most importantly, the TRPL was still fast decaying similar to what was observed in LPCVD SRN samples. However, the characterization from XRD, Raman and XPS had strongly suggested that the samples undergoing high temperature anneal had formed Si-NCs. PL energy used was unable to excite these nanocrystals due to the high defect density. The origin of the luminescence was identified to be from oxygen related defects in addition to the intrinsic defects which may have formed during annealing.

In conclusion, the experimental evidence presented that despite having promise over $SiO_2$ or SiC for suitable application in light emission, the intrinsic defects dominated within the $Si_3N_4$ matrix which was always luminescent when excited under a laser. The defects were the major luminescent centers within the material irrespective of containing a Si-NC. The laser wavelength used was sufficient to excite the defects whereas the effects from Si-NC may have been suppressed. Therefore, $Si_3N_4$ system may not be an ideal candidate as an efficient material system over $SiO_2$ for light emitting applications due to its defects.

## 7.2 Future Work

The interfacial defects formed between the $Si/SiO_2$ interface have been a common issue in CMOS technology for a very long time. Strain form thermal oxidation of Si can create such defects,

which can trap charges and eventually affect the operation of the metal-oxide-semiconductor (MOS) devices. It is therefore essential to minimize these defects to improve the performance of these devices. Hydrogen has been known to effectively passivate these defects [36], especially the interfacial defects ($P_b$ centers), which are the major source of charge trapping in the $Si/SiO_2$ interface. Interfacial defects are found to be reduced when devices are introduced in hydrogen ambient at certain temperatures [37]. Typically annealing in a forming gas (5% – 10% $H_2$ in $N_2$) ambient at 400 °C works fairly well for MOS related devices [36].

In the fabrication of Si nanocrystals in $SiO_2$, it has been established that the interface defects present in MOS devices also occur at the interface between the Si-NC and the dielectric matrix [176], [177]. Lannoo *et al*. [35] also showed that a single dangling bond defect is sufficient to quench the visible luminescence from a Si nanocrystal. Hydrogen passivation, however, has been effective after improving the luminescence efficiency similar to MOS device passivation [39], [41], [178], [179]. The nanocrystals are annealed in forming gas to achieve the passivation.

Although good passivation results have been achieved after improving the device performance of $Si/SiO_2$ based MOS devices and Si-NCs in $SiO_2$, there has been very little development in passivating the defects in $Si_3N_4$. $Si_3N_4$ is expected to have interfacial defects at the $Si_3N_4/Si$ interface and it was discovered that the number of defects at the nitride interface is higher than its oxide counterpart [72], [73]. In addition, from electron spin resonance (ESR) measurements, numerous studies have identified various other defects within the nitride matrix that are induced due to Si or N dangling bonds or oxide related bonds, and the densities of some of the defects were found to increase from ~$10^{17}$ $cm^{-3}$ to ~$10^{18}$ $cm^{-3}$ when annealed at high

temperatures [136], [137], [139], [141]. Many of these defects were predicted to exist in silicon nitrides that were annealed at high temperature to form Si-NCs [76], [78], [81], [114].

The defects in the $Si_3N_4$ still impose a major challenge after developing a highly efficient device. It is therefore important to reduce the defects in such materials prior to making the device. Hydrogen passivation can still effectively reduce the dangling bond defects in SRN systems. The step immediately after forming Si-NC in $Si_3N_4$ would be to design experiments on the effect of forming gas annealing at different temperatures and annealing time. Additionally, passivation using atomic hydrogen can be used to increase the rate of diffusion of hydrogen in the bulk of the material. Other possible methods of introducing hydrogen may include ion implantation of $H^+$ ions or sputtering in a forming gas environment.

Throughout the project, photoluminescence spectroscopy had a major role after identifying both the defect and the quantum dot states. The PL setup was only available for an excitation energy of 400 nm (3.1 eV), which may have been sufficient enough to excite the defects in the $Si_3N_4$. A spectrometer capable of generating light at lower energy that does not excite the defects could be used to probe for the Si-NCs that are present in the SRN samples. Wang *et al*. [76] reported that when SRN samples were illuminated using a 325 nm He-Cd laser, the PL would be detected from defects alone. However, when samples were excited using a 514.5 nm Ar laser, the PL was different and it had also redshifted for excess Si-concentration. They related the PL to be originating from the quantum dots. Hence, it would be interesting to observe the evolution of PL with variable excitation energy.

The goal of the study was to validate if the Si-NCs in SRN samples would be a suitable choice over $SiO_2$ or SiC in a Si-based light emitting device. The device is typically fabricated on

a doped (either n- or p-type) Si-wafer, where the dielectric containing nanocrystals are deposited and a transparent carrier injection layer is lithographically defined on top. By applying an electric field across the device, electroluminescence can be measured coming from the transparent layer. There are a number of challenges to realizing a LED with such materials – 1) The carrier injection into the nanocrystal is still difficult and not very well understood for SRN type materials, 2) A very careful control of the excess Si is required that will contain enough Si-NCs for carrier injection and also will not be highly conductive and leaky. In addition, the selection of an active transparent layer from which light will be emitted remains a challenge. Several reports suggested using a thin polysilicon [180]–[182] layer whereas others used indium-tin-oxide (ITO) depositions [183]–[185]. However, the fabrication of a successful LED using the Si-NCs could serve as a standalone project.

With all the challenges Si-NCs in SRN currently impose, there is still plenty of work to be done in order to fully understand the behavior of the nanocrystals, their defects, and successful methods to reducing these defects before integrating them into a functional efficient device. Once these issues have been addressed, the successful integration of Si-NC in semiconductor devices can be realized.

## REFERENCES


[1] Z. Yuan, A. Anopchenko, N. Daldosso, R. Guider, D. Navarro-Urrios, A. Pitanti, R. Spano, and L. Pavesi, "Silicon Nanocrystals as an Enabling Material for Silicon Photonics," *Proc. IEEE*, vol. 97, no. 7, pp. 1250–1268, Jul. 2009.

[2] J. Liu, X. Sun, D. Pan, X. Wang, L. C. Kimerling, T. L. Koch, and J. Michel, "Tensile-strained, n-type Ge as a gain medium for monolithic laser integration on Si.," *Opt. Express*, vol. 15, pp. 11272–11277, 2007.

[3] E. O. Sveinbjörnsson and J. Weber, "Room temperature electroluminescence from dislocation-rich silicon," *Appl. Phys. Lett.*, vol. 69, p. 2686, 1996.

[4] V. Kveder, M. Badylevich, E. Steinman, A. Izotov, M. Seibt, and W. Schröter, "Room-temperature silicon light-emitting diodes based on dislocation luminescence," *Appl. Phys. Lett.*, vol. 84, pp. 2106–2108, 2004.

[5] C. Li, T. Suemasu, and F. Hasegawa, "Room-temperature electroluminescence of a Si-based p-i-n diode with β-FeSi[sub 2] particles embedded in the intrinsic silicon," *J. Appl. Phys.*, vol. 97, no. 4, p. 43529, 2005.

[6] D. Leong, M. Harry, K. J. Reeson, and K. P. Homewood, "A silicon/iron-disilicide light-emitting diode operating at a wavelength of 1.5 μm," *Nature*, vol. 387, pp. 686–688, 1997.

[7] H.-S. Han, S.-Y. Seo, and J. H. Shin, "Optical gain at 1.54 μm in erbium-doped silicon nanocluster sensitized waveguide," *Appl. Phys. Lett.*, vol. 79, no. 27, p. 4568, 2001.

[8] N. Daldosso, D. Navarro-Urrios, M. Melchiorri, C. García, P. Pellegrino, B. Garrido, C. Sada, G. Battaglin, F. Gourbilleau, R. Rizk, and L. Pavesi, "Er-coupled Si nanocluster waveguide," *IEEE J. Sel. Top. Quantum Electron.*, vol. 12, pp. 1607–1617, 2006.

[9] Z. Z. Yuan, D. S. Li, M. H. Wang, P. L. Chen, D. Gong, L. Wang, and D. Yang, "Photoluminescence of Tb3+ doped SiNx films grown by plasma-enhanced chemical vapor deposition," *J. Appl. Phys.*, vol. 100, p. 83106, 2006.

[10] L. T. Canham, "Silicon quantum wire array fabrication by electrochemical and chemical dissolution of wafers," *Appl. Phys. Lett.*, vol. 57, no. 10, p. 1046, 1990.

[11] H. Tamura, M. Rückschloss, T. Wirschem, and S. Vepřek, "Origin of the green/blue luminescence from nanocrystalline silicon," *Appl. Phys. Lett.*, vol. 65, no. 12, pp. 1537–1539, 1994.

[12] L. Pavesi, L. Dal Negro, C. Mazzoleni, G. Franzò, F. Priolo, L. Pavesi, L. D. Negro, C. Mazzoleni, G. Franzo, L. Dal Negro, C. Mazzoleni, G. Franzò, and F. Priolo, "Optical gain

in silicon nanocrystals.," *Nature*, vol. 408, no. 6811, pp. 440–4, Nov. 2000.

[13] L. Tsybeskov and D. J. Lockwood, "Silicon-germanium nanostructures for light emitters and on-chip optical interconnects," *Proc. IEEE*, vol. 97, pp. 1284–1303, 2009.

[14] W. D. A. M. de Boer, D. Timmerman, K. Dohnalová, I. N. Yassievich, H. Zhang, W. J. Buma, and T. Gregorkiewicz, "Red spectral shift and enhanced quantum efficiency in phonon-free photoluminescence from silicon nanocrystals.," *Nat. Nanotechnol.*, vol. 5, pp. 878–884, 2010.

[15] T.-W. Kim, C.-H. Cho, B.-H. Kim, and S.-J. Park, "Quantum confinement effect in crystalline silicon quantum dots in silicon nitride grown using SiH[sub 4] and NH[sub 3]," *Appl. Phys. Lett.*, vol. 88, no. 12, p. 123102, 2006.

[16] L. Pavesi, "Will silicon be the photonic material of the third millenium?," *J. Phys. Condens. Matter*, vol. 15, no. 26, pp. R1169–R1196, 2003.

[17] L. Mangolini, D. Jurbergs, E. Rogojina, and U. Kortshagen, "Plasma synthesis and liquid-phase surface passivation of brightly luminescent Si nanocrystals," *J. Lumin.*, vol. 121, no. 2, pp. 327–334, Dec. 2006.

[18] J. Valenta, A. Fucikova, F. Vácha, F. Adamec, J. Humpolíčková, M. Hof, I. Pelant, K. Kůsová, K. Dohnalová, and J. Linnros, "Light-emission performance of silicon nanocrystals deduced from single quantum dot spectroscopy," *Adv. Funct. Mater.*, vol. 18, no. 18, pp. 2666–2672, 2008.

[19] W. Shockley and W. T. Read, "Statistics of the Recombinations of Holes and Electrons," *Phys. Rev.*, vol. 87, no. 5, pp. 835–842, Sep. 1952.

[20] G. M. Credo, M. D. Mason, and S. K. Buratto, "External quantum efficiency of single porous silicon nanoparticles," *Appl. Phys. Lett.*, vol. 74, p. 1978, 1999.

[21] J. Heitmann, F. Müller, L. Yi, M. Zacharias, D. Kovalev, and F. Eichhorn, "Excitons in Si nanocrystals: Confinement and migration effects," *Phys. Rev. B - Condens. Matter Mater. Phys.*, vol. 69, no. 19, pp. 1–7, 2004.

[22] D. Kovalev, H. Heckler, G. Polisski, and F. Koch, "Optical Properties of Si Nanocrystals," *Phys. Status Solidi*, vol. 215, no. 2, pp. 871–932, Oct. 1999.

[23] H. Takagi, H. Ogawa, Y. Yamazaki, A. Ishizaki, and T. Nakagiri, "Quantum size effects on photoluminescence in ultrafine Si particles," *Appl. Phys. Lett.*, vol. 56, no. 24, pp. 2379–2380, 1990.

[24] A. Nakajima, Y. Sugita, K. Kawamura, H. Tomita, and N. Yokoyama, "Si Quantum Dot Formation with Low-Pressure Chemical Vapor Deposition," *Jpn. J. Appl. Phys.*, vol. 35,

no. Part 2, No. 2B, pp. L189–L191, Feb. 1996.

[25] T. Shimizu-Iwayama, S. Nakao, and K. Saitoh, “Visible photoluminescence in Si+-implanted thermal oxide films on crystalline Si,” *Appl. Phys. Lett.*, vol. 65, no. 14, pp. 1814–1816, 1994.

[26] Q. Zhang, S. C. Bayliss, and D. A. Hutt, “Blue photoluminescence and local structure of Si nanostructures embedded in SiO2 matrices,” *Appl. Phys. Lett.*, vol. 66, no. 15, pp. 1977–1979, 1995.

[27] U. Kahler and H. Hofmeister, “Silicon nanocrystallites in buried SiO[sub x] layers via direct wafer bonding,” *Appl. Phys. Lett.*, vol. 75, no. 5, p. 641, 1999.

[28] H. C. Le, R. W. Dreyfus, W. Marine, M. Sentis, and I. A. Movtchan, “Temperature measurements during laser ablation of Si into He, Ar and O2,” *Appl. Surf. Sci.*, vol. 96–98, pp. 164–169, 1996.

[29] F. Iacona, G. Franzò, C. Spinella, and G. Franzò, “Correlation between luminescence and structural properties of Si nanocrystals,” *J. Appl. Phys.*, vol. 87, no. 3, p. 1295, 2000.

[30] M. Bose, D. N. Bose, and D. K. Basa, “Plasma enhanced growth, composition and refractive index of silicon oxynitride films,” *Mater. Lett.*, vol. 52, no. 6, pp. 417–422, 2002.

[31] M. Zacharias, J. Heitmann, R. Scholz, U. Kahler, M. Schmidt, and J. Bläsing, “Size-controlled highly luminescent silicon nanocrystals: A SiO/SiO2 superlattice approach,” *Appl. Phys. Lett.*, vol. 80, no. 4, p. 661, 2002.

[32] L. A. Nesbit, “Annealing characteristics of Si-rich SiO2 films,” *Appl. Phys. Lett.*, vol. 46, no. 1, p. 38, 1985.

[33] A. V. Dvurechensky, F. L. Edelman, and I. A. Ryazantsev, “The phase composition of SiOx films,” *Thin Solid Films*, vol. 91, no. 1, pp. L55–L57, 1982.

[34] A. Hartstein, J. C. Tsang, D. J. Dimaria, and D. W. Dong, “Observation of amorphous silicon regions in silicon-rich silicon dioxide films,” *Appl. Phys. Lett.*, vol. 36, no. 10, pp. 836–837, 1980.

[35] M. Lannoo, C. Delerue, and G. Allan, “Theory of radiative and nonradiative transitions for semiconductor nanocrystals,” *J. Lumin.*, vol. 70, no. 1–6, pp. 170–184, Oct. 1996.

[36] Y. C. C. Cheng, “Electronic states at the silicon-silicon dioxide interface,” *Progress in Surface Science*, vol. 8, no. 5. pp. 181–218, 1977.

[37] E. H. Poindexter and P. J. Caplan, “Characterization of Si/SiO2 interface defects by electron spin resonance,” *Progress in Surface Science*, vol. 14, no. 3. pp. 201–294, 1983.

[38] E. Neufeld, S. Wang, R. Apetz, C. Buchal, R. Carius, C. W. White, and D. K. Thomas, "Effect of annealing and H2 passivation on the photoluminescence of Si nanocrystals in SiO2," *Thin Solid Films*, vol. 294, no. 1–2. pp. 238–241, 1997.

[39] S. Cheylan and R. G. Elliman, "Effect of particle size on the photoluminescence from hydrogen passivated Si nanocrystals in SiO2," *Appl. Phys. Lett.*, vol. 78, no. 13, pp. 1912–1914, 2001.

[40] A. Wilkinson and R. Elliman, "Kinetics of H2 passivation of Si nanocrystals in SiO2," *Phys. Rev. B*, vol. 68, no. 15, p. 155302, Oct. 2003.

[41] A. R. Wilkinson and R. G. Elliman, "Passivation of Si nanocrystals in SiO[sub 2]: Atomic versus molecular hydrogen," *Appl. Phys. Lett.*, vol. 83, no. 26, p. 5512, 2003.

[42] W. M. A. Bik, R. N. H. Linssen, F. H. P. M. Habraken, W. F. Van der Weg, and A. E. T. Kuiper, "Diffusion of hydrogen in low-pressure chemical vapor deposited silicon nitride films," *Appl. Phys. Lett.*, vol. 56, no. 25, pp. 2530–2532, 1990.

[43] K. S. Cho, N. M. Park, T. Y. Kim, K. H. Kim, G. Y. Sung, and J. H. Shin, "High efficiency visible electroluminescence from silicon nanocrystals embedded in silicon nitride using a transparent doping layer," *Appl. Phys. Lett.*, vol. 86, no. 7, pp. 1–3, 2005.

[44] K.-Y. Cheng, R. Anthony, U. R. Kortshagen, and R. J. Holmes, "Hybrid Silicon Nanocrystal−Organic Light-Emitting Devices for Infrared Electroluminescence," *Nano Lett.*, vol. 10, no. 4, pp. 1154–1157, Apr. 2010.

[45] G. Conibeer, M. Green, R. Corkish, Y. Cho, E. Cho, C. Jiang, T. Fangsuwannarak, E. Pink, Y. Huang, and T. Puzzer, "Silicon nanostructures for third generation photovoltaic solar cells," *Thin Solid Films*, vol. 511–512, pp. 654–662, Jul. 2006.

[46] E.-C. Cho, M. a. Green, G. Conibeer, D. Song, Y.-H. Cho, G. Scardera, S. Huang, S. Park, X. J. Hao, Y. Huang, and L. Van Dao, "Silicon Quantum Dots in a Dielectric Matrix for All-Silicon Tandem Solar Cells," *Adv. Optoelectron.*, vol. 2007, pp. 1–12, 2007.

[47] H. I. Hanafi, S. Tiwari, and I. Khan, "Fast and long retention-time nano-crystal memory," *IEEE Trans. Electron Devices*, vol. 43, no. 9, pp. 1553–1558, 1996.

[48] S. F. Cogan, D. J. Edell, A. a Guzelian, Y. Ping Liu, and R. Edell, "Plasma-enhanced chemical vapor deposited silicon carbide as an implantable dielectric coating," *J. Biomed. Mater. Res.*, vol. 67A, no. 3, pp. 856–867, Dec. 2003.

[49] J. M. Hsu, P. Tathireddy, L. Rieth, A. R. Normann, and F. Solzbacher, "Characterization of a-SiCx:H thin films as an encapsulation material for integrated silicon based neural interface devices," *Thin Solid Films*, vol. 516, no. 1, pp. 34–41, 2007.

[50] G. L. Knaack, D. G. McHail, G. Borda, B. Koo, N. Peixoto, S. F. Cogan, T. C. Dumas, and J. J. Pancrazio, “In vivo Characterization of Amorphous Silicon Carbide As a Biomaterial for Chronic Neural Interfaces,” *Front. Neurosci.*, vol. 10, no. June, p. 301, Jun. 2016.

[51] X. Lei, S. Kane, S. Cogan, H. Lorach, L. Galambos, P. Huie, K. Mathieson, T. Kamins, J. Harris, and D. Palanker, “SiC protective coating for photovoltaic retinal prosthesis,” *J. Neural Eng.*, vol. 13, no. 4, p. 46016, Aug. 2016.

[52] J. D. Plummer, M. D. Deal, and P. B. Griffin, *Silicon VLSI technology: fundamentals, practice and modeling*. 2000.

[53] T. H. Gfroerer, “Photoluminescence in Analysis of Surfaces and Interfaces,” in *Encyclopedia of Analytical Chemistry*, Chichester, UK: John Wiley & Sons, Ltd, 2006, pp. 9209–9231.

[54] P. Benalloul, J. Benoit, R. Mach, G. O. Müller, and G. U. Reinsperger, “Decay of ZnS:Mn emission in thin films — revisited,” *Journal of Crystal Growth*, vol. 101, no. 1–4. pp. 989–993, 1990.

[55] V. Suendo, “Low temperature plasma synthesis of silicon nanocrystals for photonic applications,” 2005.

[56] W. L. Bragg, “The Structure of Some Crystals as Indicated by Their Diffraction of X-rays,” *Proceedings of the Royal Society A: Mathematical, Physical and Engineering Sciences*, vol. 89, no. 610. pp. 248–277, 1913.

[57] Y. Leng, *Materials Characterization*. Chichester, UK: John Wiley & Sons, Ltd, 2008.

[58] P. Scherrer, “Bestimmung der Größe und der inneren Struktur von Kolloidteilchen mittels Röntgenstrahlen,” *Nachrichten von der Gesellschaft der Wissenschaften zu Göttingen, Math. Klasse*, vol. 1918, pp. 98–100, 1918.

[59] B. A. Sarsfield, M. Davidovich, S. Desikan, M. Fakes, S. Futernik, J. L. Hilden, J. S. Tan, S. Yin, G. Young, B. Vakkalagadda, and K. Volk, “Powder X-ray Diffraction Detection of Crystalline Phases in Amorphous Pharmaceuticals,” *Adv. X-ray Anal.*, vol. 49, pp. 322–327, 2006.

[60] D. A. Long, “Introductory Raman Spectroscopy. John R. Ferraro, Kazuo Nakamoto and Chris W. Brown. Academic Press, Amsterdam, Second Edition, 2003. xiii + 434,” *J. Raman Spectrosc.*, vol. 36, no. 10, pp. 1012–1012, Oct. 2005.

[61] N. B. Colthup, L. H. Daly, and S. E. Wiberley, *Introduction to Infrared and Raman Spectroscopy*. 1990.

[62] L. Ren, X. Su, Y. Wang, J. Xu, and K. Ning, “QSpec: online control and data analysis

system for single-cell Raman spectroscopy," *PeerJ*, vol. 2, p. e436, Jun. 2014.

[63] Z. H. Z. Lu, D. J. D. Lockwood, and J.-M. J. M. Baribeau, "Quantum confinement and light emission in SiO2/Si superlattices," *Lett. to Nat.*, vol. 378, no. 6554, pp. 258–260, 1995.

[64] M. Molinari, H. Rinnert, M. Vergnat, and P. Weisbecker, "Evolution with annealing treatments of the size of silicon nanocrystallites embedded in a SiNx matrix and correlation with optical properties," *Mater. Sci. Eng. B*, vol. 101, no. 1, pp. 186–189, 2003.

[65] A. Martínez, J. Blasco, P. Sanchis, J. V. Galán, J. García-Rupérez, E. Jordana, P. Gautier, Y. Lebour, S. Hernández, R. Guider, N. Daldosso, B. Garrido, J. M. Fedeli, L. Pavesi, J. Martí, and R. Spano, "Ultrafast all-optical switching in a silicon-nanocrystal-based silicon slot waveguide at telecom wavelengths," *Nano Lett.*, vol. 10, no. 4, pp. 1506–1511, May 2010.

[66] J. Yao, Z. Sun, L. Zhong, D. Natelson, and J. M. Tour, "Resistive switches and memories from silicon oxide.," *Nano Lett.*, vol. 10, no. 10, pp. 4105–10, Oct. 2010.

[67] W. Marine, L. Patrone, B. Luk'yanchuk, and M. Sentis, "Strategy of nanocluster and nanostructure synthesis by conventional pulsed laser ablation," *Appl. Surf. Sci.*, vol. 154–155, pp. 345–352, Feb. 2000.

[68] Y.-H. So, A. Gentle, S. Huang, G. Conibeer, and M. A. Green, "Size dependent optical properties of Si quantum dots in Si-rich nitride/Si3N4 superlattice synthesized by magnetron sputtering," *J. Appl. Phys.*, vol. 109, no. 6, p. 64302, 2011.

[69] N.-M. Park, C.-J. Choi, T.-Y. Seong, and S.-J. Park, "Quantum Confinement in Amorphous Silicon Quantum Dots Embedded in Silicon Nitride," *Phys. Rev. Lett.*, vol. 86, no. 7, pp. 1355–1357, Feb. 2001.

[70] V. E. Vamvakas, N. Vourdas, and S. Gardelis, "Optical characterization of Si-rich silicon nitride films prepared by low pressure chemical vapor deposition," *Microelectron. Reliab.*, vol. 47, no. 4–5, pp. 794–797, Apr. 2007.

[71] C.-W. W. Jiang and M. A. Green, "Silicon quantum dot superlattices: Modeling of energy bands, densities of states, and mobilities for silicon tandem solar cell applications," *J. Appl. Phys.*, vol. 99, no. 11, p. 114902, 2006.

[72] H. J. Stein, S. T. Picraux, and P. H. Holloway, "Analyses for stoichiometry and for Hydrogen and Oxygen in silicon nitride films," *IEEE Trans. Electron Devices*, vol. 25, no. 8, 1978.

[73] H. J. Stein, "Chemically Bound Hydrogen in CVD Si[sub 3]N[sub 4]: Dependence on NH[sub 3]/SiH[sub 4] Ratio and on Annealing," *J. Electrochem. Soc.*, vol. 124, no. 6, p. 908, 1977.

[74] H. Miyashita and Y. Watabe, “Flatband voltage shift of amorphous silicon nitride metal-insulator-semiconductor diodes,” *J. Appl. Phys.*, vol. 70, no. 4, p. 2452, 1991.

[75] C.-J. Lin, C.-K. Lin, C.-W. Chang, Y.-L. Chueh, H.-C. Kuo, E. W.-G. Diau, L.-J. Chou, and G.-R. Lin, “Photoluminescence of Plasma Enhanced Chemical Vapor Deposition Amorphous Silicon Oxide with Silicon Nanocrystals Grown at Different Fluence Ratios and Substrate Temperatures,” *Jpn. J. Appl. Phys.*, vol. 45, no. 2A, pp. 1040–1043, Feb. 2006.

[76] M. Wang, D. Li, Z. Yuan, D. Yang, and D. Que, “Photoluminescence of Si-rich silicon nitride: Defect-related states and silicon nanoclusters,” *Appl. Phys. Lett.*, vol. 90, no. 13, p. 131903, 2007.

[77] H. L. Hao, L. K. Wu, W. Z. Shen, and H. F. W. Dekkers, “Origin of visible luminescence in hydrogenated amorphous silicon nitride,” *Appl. Phys. Lett.*, vol. 91, no. 20, pp. 2005–2008, 2007.

[78] J. Kistner, X. Chen, Y. Weng, H. P. Strunk, M. B. Schubert, and J. H. Werner, “Photoluminescence from silicon nitride—no quantum effect,” *J. Appl. Phys.*, vol. 110, no. 2, p. 23520, 2011.

[79] Y. Liu, Y. Zhou, W. Shi, L. Zhao, B. Sun, and T. Ye, “Study of photoluminescence spectra of Si-rich SiNx films,” *Mater. Lett.*, vol. 58, no. 19, pp. 2397–2400, Jul. 2004.

[80] C. M. Mo, L. Zhang, C. Xie, and T. Wang, “Luminescence of nanometer-sized amorphous silicon nitride solids,” *J. Appl. Phys.*, vol. 73, no. 10, pp. 5185–5188, 1993.

[81] S. V. Deshpande, E. Gulari, S. W. Brown, and S. C. Rand, “Optical properties of silicon nitride films deposited by hot filament chemical vapor deposition,” *J. Appl. Phys.*, vol. 77, no. 12, pp. 6534–6541, 1995.

[82] L. Khriachtchev, M. Räsänen, S. Novikov, and J. Sinkkonen, “Optical gain in Si/SiO[sub 2] lattice: Experimental evidence with nanosecond pulses,” *Appl. Phys. Lett.*, vol. 79, no. 9, p. 1249, 2001.

[83] L. Dal Negro, J. H. Yi, J. Michel, L. C. Kimerling, T.-W. F. W. F. Chang, V. Sukhovatkin, and E. H. Sargent, “Light emission efficiency and dynamics in silicon-rich silicon nitride films,” *Appl. Phys. Lett.*, vol. 88, no. 23, p. 233109, 2006.

[84] V. Vinciguerra, G. Franzò, F. Priolo, F. Iacona, and C. Spinella, “Quantum confinement and recombination dynamics in silicon nanocrystals embedded in Si/SiO[sub 2] superlattices,” *J. Appl. Phys.*, vol. 87, no. 11, p. 8165, 2000.

[85] C. Garcia, B. Garrido, P. Pellegrino, R. Ferre, J. A. Moreno, J. R. Morante, L. Pavesi, and M. Cazzanelli, “Size dependence of lifetime and absorption cross section of Si nanocrystals embedded in SiO2,” *Appl. Phys. Lett.*, vol. 82, no. 10, pp. 1595–1597, 2003.

[86] B.-H. Lai, C.-H. Cheng, Y.-H. Pai, and G.-R. Lin, “Plasma power controlled deposition of SiO_x with manipulated Si Quantum Dot size for photoluminescent wavelength tailoring,” *Opt. Express*, vol. 18, no. 5, p. 4449, Mar. 2010.

[87] G. R. Lin, C. J. Lin, and K. C. Yu, “Time-resolved photoluminescence and capacitance-voltage analysis of the neutral vacancy defect in silicon implanted SiO2 on silicon substrate,” *J. Appl. Phys.*, vol. 96, no. 5, pp. 3025–3027, 2004.

[88] D. A. Shirley, “High-Resolution X-Ray Photoemission Spectrum of the Valence Bands of Gold,” *Phys. Rev. B*, vol. 5, no. 12, pp. 4709–4714, Jun. 1972.

[89] A.-S. Keita, A. En Naciri, F. Delachat, M. Carrada, G. Ferblantier, and A. Slaoui, “Spectroscopic ellipsometry investigation of the optical properties of nanostructured Si/SiN[sub x] films,” *J. Appl. Phys.*, vol. 107, no. 9, p. 93516, 2010.

[90] G. E. Jellison, Jr, F. a. Modine, P. Doshi, and A. Rohatgi, “Spectroscopic ellipsometry characterization of thin-film silicon nitride,” *Thin Solid Films*, vol. 313–314, pp. 193–197, Feb. 1998.

[91] G. E. Jellison and F. A. Modine, “Erratum: ‘“Parameterization of the optical functions of amorphous materials in the interband region”’ [Appl. Phys. Lett. 69, 371 (1996)],” *Appl. Phys. Lett.*, vol. 69, no. 14, p. 2137, 1996.

[92] G. E. Jellison and F. A. Modine, “Parameterization of the optical functions of amorphous materials in the interband region,” *Appl. Phys. Lett.*, vol. 69, no. 3, p. 371, Dec. 1996.

[93] W. L. Warren, J. Robertson, and J. Kanicki, “Si and N dangling bond creation in silicon nitride thin films,” *Appl. Phys. Lett.*, vol. 63, no. 19, pp. 2685–2687, 1993.

[94] G. Lucovsky, J. Yang, S. S. Chao, J. E. Tyler, and W. Czubatyj, “Nitrogen-bonding environments in glow-discharge—deposited a−Si:H films,” *Phys. Rev. B*, vol. 28, no. 6, pp. 3234–3240, Sep. 1983.

[95] S. Hasegawa, M. Matsuda, and Y. Kurata, “Si-H and N-H vibrational properties in glow-discharge amorphous SiNx:H films (0<x<1.55),” *Appl. Phys. Lett.*, vol. 57, no. 21, p. 2211, 1990.

[96] G. Scardera, T. Puzzer, G. Conibeer, and M. A. Green, “Fourier transform infrared spectroscopy of annealed silicon-rich silicon nitride thin films,” *J. Appl. Phys.*, vol. 104, no. 10, p. 104310, 2008.

[97] J. Robertson, “Electronic structure of silicon nitride,” *Philos. Mag. Part B*, vol. 63, no. 1, pp. 47–77, 1991.

[98] J. Robertson and M. J. Powell, “Gap states in silicon nitride,” *Appl. Phys. Lett.*, vol. 44, no.

4, p. 415, 1984.

[99] O. Debieu, R. P. Nalini, J. Cardin, X. Portier, J. Perrière, and F. Gourbilleau, "Structural and optical characterization of pure Si-rich nitride thin films.," *Nanoscale Res. Lett.*, vol. 8, no. 1, p. 31, Jan. 2013.

[100] B.-H. H. Kim, C.-H. H. Cho, T.-W. W. Kim, N.-M. M. Park, G. Y. Sung, and S.-J. J. Park, "Photoluminescence of silicon quantum dots in silicon nitride grown by NH[sub 3] and SiH[sub 4]," *Appl. Phys. Lett.*, vol. 86, no. 9, pp. 1–3, 2005.

[101] M. Ribeiro and I. Pereyra, "Study of phase separation and photoluminescent emission in silicon nanostructured PECVD systems," *Phys. Status Solidi Curr. Top. Solid State Phys.*, vol. 7, no. 3–4, pp. 624–627, Jan. 2010.

[102] S. Charvet, R. Madelon, R. Rizk, B. Garrido, O. González-Varona, M. López, a Pérez-Rodríguez, and J. . Morante, "Substrate temperature dependence of the photoluminescence efficiency of co-sputtered Si/SiO2 layers," *J. Lumin.*, vol. 80, no. 1–4, pp. 241–245, 1998.

[103] F. Delachat, M. Carrada, G. Ferblantier, J.-J. Grob, a Slaoui, and H. Rinnert, "The structural and optical properties of SiO2/Si rich SiNx multilayers containing Si-ncs.," *Nanotechnology*, vol. 20, no. 27, p. 275608, Jul. 2009.

[104] M. Luppi and S. Ossicini, "Ab initio study on oxidized silicon clusters and silicon nanocrystals embedded in SiO2: Beyond the quantum confinement effect," *Phys. Rev. B*, vol. 71, no. 3, pp. 1–15, Jan. 2005.

[105] J.-M. Wagner, K. Seino, F. Bechstedt, A. Dymiati, J. Mayer, R. Rölver, M. Först, B. Berghoff, B. Spangenberg, and H. Kurz, "Electronic band gap of Si/SiO[sub 2] quantum wells: Comparison of ab initio calculations and photoluminescence measurements," *Journal of Vacuum Science & Technology A: Vacuum, Surfaces, and Films*, vol. 25. p. 1500, 2007.

[106] S. Charvet, R. Madelon, F. Gourbilleau, and R. Rizk, "Spectroscopic ellipsometry analyses of sputtered Si/SiO[sub 2] nanostructures," *J. Appl. Phys.*, vol. 85, no. 8, p. 4032, 1999.

[107] M. Dovrat, Y. Goshen, J. Jedrzejewski, I. Balberg, and A. Sa'ar, "Radiative versus nonradiative decay processes in silicon nanocrystals probed by time-resolved photoluminescence spectroscopy," *Phys. Rev. B*, vol. 69, no. 15, pp. 1–8, Apr. 2004.

[108] H. Rinnert, O. Jambois, and M. Vergnat, "Photoluminescence properties of size-controlled silicon nanocrystals at low temperatures," *J. Appl. Phys.*, vol. 106, no. 2, p. 23501, 2009.

[109] J. Linnros, N. Lalic, A. Galeckas, and V. Grivickas, "Analysis of the stretched exponential photoluminescence decay from nanometer-sized silicon crystals in SiO[sub 2]," *J. Appl. Phys.*, vol. 86, no. 11, p. 6128, 1999.

[110] Y. Kanemitsu, "Photoluminescence spectrum and dynamics in oxidized silicon nanocrystals: A nanoscopic disorder system," *Phys. Rev. B*, vol. 53, no. 20, pp. 13515–13520, May 1996.

[111] Y. Varshni, "Temperature dependence of the energy gap in semiconductors," *Physica*, vol. 34, no. 1. pp. 149–154, 1967.

[112] G. Y. Sung, "Physics and Device Structures of Highly Efficient Silicon Quantum Dots Based Silicon Nitride Light-Emitting Diodes," *IEEE J. Sel. Top. Quantum Electron.*, vol. 86, no. 6, pp. 173504-1–1555, Nov. 2006.

[113] P. D. Nguyen, D. M. Kepaptsoglou, Q. M. Ramasse, and A. Olsen, "Direct observation of quantum confinement of Si nanocrystals in Si-rich nitrides," *Phys. Rev. B - Condens. Matter Mater. Phys.*, vol. 85, no. 8, pp. 1–8, Feb. 2012.

[114] D. Hiller, A. Zelenina, S. Gutsch, S. A. Dyakov, L. López-Conesa, J. López-Vidrier, S. Estradé, F. Peiró, B. Garrido, J. Valenta, M. Kořínek, F. Trojánek, P. Malý, M. Schnabel, C. Weiss, S. Janz, and M. Zacharias, "Absence of quantum confinement effects in the photoluminescence of Si3N4–embedded Si nanocrystals," *J. Appl. Phys.*, vol. 115, no. 20, p. 204301, May 2014.

[115] L. Dal Negro, J. H. J. Yi, L. C. L. Kimerling, S. Hamel, a. Williamson, G. Galli, L. D. Negro, J. H. J. Yi, L. C. L. Kimerling, S. Hamel, and A, "Light emission from silicon-rich nitride nanostructures," *Appl. Phys.*, vol. 88, no. 18, pp. 88–90, 2006.

[116] P. D. Nguyen, D. M. Kepaptsoglou, Q. M. Ramasse, M. F. Sunding, L. O. Vestland, T. G. Finstad, and a. Olsen, "Impact of oxygen bonding on the atomic structure and photoluminescence properties of Si-rich silicon nitride thin films," *J. Appl. Phys.*, vol. 112, no. 7, p. 73514, 2012.

[117] M. Vila, C. Prieto, and R. Ramírez, "Electrical behavior of silicon nitride sputtered thin films," in *Thin Solid Films*, 2004, vol. 459, no. 1–2, pp. 195–199.

[118] B. El-Kareh, *Fundamentals of Semiconductor Processing Technology*. Springer US, 2012.

[119] K. N. Andersen, W. E. Svendsen, T. Stimpel-Lindner, T. Sulima, and H. Baumgärtner, "Annealing and deposition effects of the chemical composition of silicon-rich nitride," *Appl. Surf. Sci.*, vol. 243, no. 1–4, pp. 401–408, Apr. 2005.

[120] S. Mohammed, M. T. Nimmo, A. V. Malko, and C. L. Hinkle, "Chemical bonding and defect states of LPCVD grown silicon-rich Si3N4 for quantum dot applications," *J. Vac. Sci. Technol. A Vacuum, Surfaces, Film.*, vol. 32, no. 2, p. 21507, 2014.

[121] T.-Y. Kim, N.-M. Park, K.-H. Kim, G. Y. Sung, Y.-W. Ok, T.-Y. Seong, and C.-J. Choi, "Quantum confinement effect of silicon nanocrystals in situ grown in silicon nitride films,"

*Appl. Phys. Lett.*, vol. 85, no. 22, p. 5355, 2004.

[122] L. K. Bekessy, N. A. Raftery, and S. Russell, "Anomalous Scattering from Single Crystal Substrate," *Adv. X-ray Anal.*, vol. 50, pp. 177–181, 2007.

[123] E. Bustarret, M. A. Hachicha, and M. Brunel, "Experimental determination of the nanocrystalline volume fraction in silicon thin films from Raman spectroscopy," *Appl. Phys. Lett.*, vol. 52, no. 20, p. 1675, 1988.

[124] G. M. Ingo, "X-ray photoelectron spectroscopy investigation on the chemical structure of amorphous silicon nitride (a-SiNx)," *J. Vac. Sci. Technol. A Vacuum, Surfaces, Film.*, vol. 7, no. 5, p. 3048, Sep. 1989.

[125] G.-E. Yu, M. Edirisinghe, D. Finch, B. Ralph, and J. Parrick, "Synthesis of silicon oxynitride from a polymeric precursor," *J. Mater. Sci.*, vol. 30, no. 21, pp. 5371–5380, Jan. 1995.

[126] J. Finster, E. D. Klinkenberg, J. Heeg, and W. Braun, "ESCA and SEXAFS investigations of insulating materials for ULSI microelectronics," *Vacuum*, vol. 41, no. 7–9, pp. 1586–1589, 1990.

[127] P. Cova, S. Poulin, O. Grenier, and R. A. Masut, "A method for the analysis of multiphase bonding structures in amorphous SiOxNy films," *J. Appl. Phys.*, vol. 97, no. 7, 2005.

[128] A. P. Li, L. Zhang, Y. X. Zhang, G. G. Qin, X. Wang, and X. W. Hu, "Electroluminescence from Au/Si nitride film/Si with the film prepared by electron cyclotron resonance method," *Appl. Phys. Lett.*, vol. 69, no. 1, p. 4, 1996.

[129] S. Jou, I.-C. Liaw, Y.-C. Cheng, and C.-H. Li, "Light emission of silicon oxynitride films prepared by reactive sputtering of silicon," *J. Lumin.*, vol. 134, pp. 853–857, Feb. 2013.

[130] Y. Mitsui, H. Kambara, M. Kojima, H. Tomita, K. Katoh, and K. Satoh, "Determination of trace impurities in highly purified nitrogen gas by atmospheric pressure ionization mass spectrometry," *Anal. Chem.*, vol. 55, no. 3, pp. 477–481, Mar. 1983.

[131] B. E. Deal and A. S. Grove, "General relationship for the thermal oxidation of silicon," *J. Appl. Phys.*, vol. 36, no. 12, pp. 3770–3778, 1965.

[132] D. J. Choi, D. B. Fischbach, and W. D. Scott, "Oxidation of Chemically-Vapor-Deposited Silicon Nitride and Slnglem-Crystal Silicon," *J. Am. Ceram. Soc.*, vol. 72, no. 7, pp. 1118–1123, Jul. 1989.

[133] S. Hasegawa, H. Anbutsu, and Y. Kurata, "Connection between Si–N and Si–H vibrational properties in amorphous SiNx: H films," *Philos. Mag. Part B*, vol. 59, no. 3, pp. 365–375, 1989.

[134] A. Szekeres, T. Nikolova, S. Simeonov, A. Gushterov, F. Hamelmann, and U. Heinzmann, "Plasma-assisted chemical vapor deposited silicon oxynitride as an alternative material for gate dielectric in MOS devices," *Microelectronics J.*, vol. 37, no. 1, pp. 64–70, 2006.

[135] B. H. Augustine, E. A. Irene, Y. J. He, K. J. Price, L. E. McNeil, K. N. Christensen, and D. M. Maher, "Visible light emission from thin films containing Si, O, N, and H," *J. Appl. Phys.*, vol. 78, no. 6, pp. 4020–4030, 1995.

[136] Y. Cros and J. Krautwurm, "Structural identification of point defects in amorphous silicon oxynitrides," *J. Non. Cryst. Solids*, vol. 187, pp. 385–394, Jul. 1995.

[137] W. L. Warren, J. Kanicki, and E. H. Poindexter, "Paramagnetic point defects in silicon nitride and silicon oxynitride thin films on silicon," *Colloids Surfaces A Physicochem. Eng. Asp.*, vol. 115, pp. 311–317, Aug. 1996.

[138] F. Rebib, E. Tomasella, S. Aida, M. Dubois, E. Bêche, J. Cellier, and M. Jacquet, "Influence of the structure of a-SiOxNy thin films on their electrical properties," *Plasma Process. Polym.*, vol. 4, no. SUPPL.1, pp. 59–63, 2007.

[139] J. Robertson, "Defects and hydrogen in amorphous silicon nitride," *Philos. Mag. Part B*, vol. 69, no. 2, pp. 307–326, 1994.

[140] E. P. O'Reilly and J. Robertson, "Theory of defects in vitreous silicon dioxide," *Phys. Rev. B*, vol. 27, no. 6, pp. 3780–3795, 1983.

[141] C. Savall, J. C. Bruyere, and J. Krautwurm, "Correlations between ESR and photoluminescence in slightly hydrogenated silicon nitride," *J. Phys. D. Appl. Phys.*, vol. 28, no. 3, pp. 565–570, Mar. 1995.

[142] A. Stesmans and G. Van Gorp, "Si≡Si3 defect at thermally grown (111)Si/Si3N4 interfaces," *Phys. Rev. B*, vol. 52, no. 12, pp. 8904–8920, Sep. 1995.

[143] W. L. Warren, J. Kanicki, J. Robertson, and P. M. Lenahan, "Energy level of the nitrogen dangling bond in amorphous silicon nitride," *Appl. Phys. Lett.*, vol. 59, no. 14, pp. 1699–1701, 1991.

[144] N. Hata and S. Wagner, "A comprehensive defect model for amorphous silicon," *J. Appl. Phys.*, vol. 72, no. 7, pp. 2857–2872, 1992.

[145] C. A. Zorman, "Silicon Carbide as a Material for Biomedical Microsystems," in *EDA Publishing*, 2009, pp. 1–7.

[146] R. G. Azevedo, Jingchun Zhang, D. G. Jones, D. R. Myers, A. V. Jog, B. Jamshidi, M. B. J. Wijesundara, R. Maboudian, and A. P. Pisano, "Silicon carbide coated MEMS strain sensor for harsh environment applications," in *2007 IEEE 20th International Conference*

*on Micro Electro Mechanical Systems (MEMS)*, 2007, pp. 643–646.

[147] S. Santavirta, M. Takagi, L. Nordsletten, A. Anttila, R. Lappalainen, and Y. T. Konttinen, "Biocompatibility of silicon carbide in colony formation test in vitro," *Arch. Orthop. Trauma Surg.*, vol. 118, no. 1–2, pp. 89–91, Nov. 1998.

[148] U. Kalnins, A. Erglis, I. Dinne, I. Kumsars, and S. Jegere, "Clinical outcomes of silicon carbide coated stents in patients with coronary artery disease.," *Med. Sci. Monit.*, vol. 8, no. 2, p. PI16-20, Feb. 2002.

[149] W.-Y. Lee, "X-ray photoelectron spectroscopy and Auger electron spectroscopy studies of glow discharge Si1−xCx:H films," *J. Appl. Phys.*, vol. 51, no. 6, p. 3365, 1980.

[150] J. M. Eldridge, J. O. Moore, G. Olive, and V. Dunton, "Oxidation of Plasma-Deposited α-Si[sub x]C[sub 1−x]:H Films," *J. Electrochem. Soc.*, vol. 137, no. 7, p. 2266, 1990.

[151] V. Mastelaro, A. M. Flank, M. C. A. Fantini, D. R. S. Bittencourt, M. N. P. Carreño, and I. Pereyra, "On the structural properties of a-Si1−xCx:H thin films," *J. Appl. Phys.*, vol. 79, no. 3, p. 1324, 1996.

[152] M. Avram, A. Avram, A. Bragaru, B. C. B. Chen, D. P. Poenar, and C. Iliescu, "Low stress PECVD amorphous silicon carbide for MEMS applications," in *Semiconductor Conference (CAS), 2010 International*, 2010, vol. 1, pp. 239–242.

[153] A. R. Oliveira and M. N. P. Carreño, "Post thermal annealing crystallization and reactive ion etching of SiC films produced by PECVD," *J. Non. Cryst. Solids*, vol. 352, no. 9–20, pp. 1392–1397, Jun. 2006.

[154] C. Iliescu, B. Chen, D. P. Poenar, and Y. Y. Lee, "PECVD amorphous silicon carbide membranes for cell culturing," *Sensors Actuators, B Chem.*, vol. 129, no. 1, pp. 404–411, 2008.

[155] P. M. Sarro, C. R. Deboer, E. Korkmaz, and J. M. W. Laros, "Low-stress PECVD SiC thin films for IC-compatible microstructures," *Sensors Actuators, A Phys.*, vol. 67, no. 1–3 pt 1, pp. 175–180, 1998.

[156] D.-S. Wuu, R.-H. Horng, C.-C. Chan, and Y.-S. Lee, "Plasma-deposited amorphous silicon carbide films for micromachined fluidic channels," *Appl. Surf. Sci.*, vol. 144–145, pp. 708–712, 1999.

[157] C. Iliescu, M. Avram, B. Chen, A. Popescu, V. Dumitrescu, D. P. Poenar, A. Sterian, D. Vrtacnik, S. Amon, and P. Sterian, "Residual stress in thin films PECVD depositions: A review," *J. Optoelectron. Adv. Mater.*, vol. 13, no. 4, pp. 387–394, 2011.

[158] H. Windischmann, "Intrinsic stress and mechanical properties of hydrogenated silicon

carbide produced by plasma-enhanced chemical vapor deposition," *J. Vac. Sci. Technol. A Vacuum, Surfaces, Film.*, vol. 9, no. 4, pp. 2459–2463, 1991.

[159] H. Windischmann, R. W. Collins, and J. M. Cavese, "Effect of hydrogen on the intrinsic stress in ion beam sputtered amorphous silicon films," *J. Non. Cryst. Solids*, vol. 85, no. 3, pp. 261–272, Aug. 1986.

[160] F. M. D'Heurle, "Aluminum films deposited by rf sputtering," *Metall. Mater. Trans. B*, vol. 1, no. 3, pp. 725–732, 1970.

[161] J. Priest, H. L. Caswell, and Y. Budo, "Mechanical stresses in silicon oxide films," *Vacuum*, vol. 12, no. 6, pp. 301–306, Nov. 1962.

[162] G. G. Stoney, "The Tension of Metallic Films Deposited by Electrolysis," *Proc. R. Soc. A Math. Phys. Eng. Sci.*, vol. 82, no. 553, pp. 172–175, May 1909.

[163] K. Ohishi and T. Hattori, "Periodic Changes in SiO2/Si(111) Interface Structures with Progress of Thermal Oxidation," *Jpn. J. Appl. Phys.*, vol. 33, no. Part 2, No. 5A, pp. L675–L678, May 1994.

[164] K. L. Smith and K. M. Black, "Characterization of the treated surfaces of silicon alloyed pyrolytic carbon and SiC," *J. Vac. Sci. Technol. A Vacuum, Surfaces, Film.*, vol. 2, no. 2, p. 744, 1984.

[165] J. M. Powers and G. A. Somorjai, "The surface oxidation of alpha-silicon carbide by O2 from 300 to 1373 K," *Surf. Sci.*, vol. 244, no. 1–2, pp. 39–50, 1991.

[166] S. Schelz and P. Oelhafen, "Interface properties of hydrogenated amorphous carbon films on SiO2 and SiO1.2: an in situ photoelectron study," *Surf. Sci.*, vol. 279, no. 1–2, pp. 137–148, Dec. 1992.

[167] C. Önneby and C. G. Pantano, "Silicon oxycarbide formation on SiC surfaces and at the SiC/SiO[sub 2] interface," *J. Vac. Sci. Technol. A Vacuum, Surfaces, Film.*, vol. 15, no. 3, p. 1597, May 1997.

[168] R. C. Lee, C. R. Aita, and N. C. Tran, "The air-exposed surface of sputter deposited silicon carbide studied by x-ray photoelectron spectroscopy," *J. Vac. Sci. Technol. A Vacuum, Surfaces, Film.*, vol. 9, no. 3, p. 1351, May 1991.

[169] J. L. C. Fonseca, D. C. Apperley, and J. P. S. Badyal, "Plasma polymerization of tetramethylsilane," *Chem. Mater.*, vol. 5, no. 11, pp. 1676–1682, Nov. 1993.

[170] F. Demichelis, G. Crovini, C. F. Pirri, and E. Tresso, "Infrared vibrational spectra of hydrogenated amorphous and microcrystalline silicon-carbon alloys," *Philos. Mag. Part B*, vol. 68, no. 3, pp. 329–340, 1993.

[171] F. Fujimoto, A. Ootuka, K. Komaki, Y. Iwata, I. Yamane, H. Yamashita, Y. Hashimoto, Y. Tawada, K. Nishimura, H. Okamoto, and Y. Hamakawa, "Hydrogen Content in a-SiC:H Films Prepared by Plasma Decomposition of Silane and Methane or Ethylene," *Jpn. J. Appl. Phys.*, vol. 23, no. Part 1, No. 7, pp. 810–814, Jul. 1984.

[172] J. Huran, L. Hrubcin, A. Kobzev, and J. Liday, "Properties of amorphous silicon carbide films prepared by PECVD," *Vacuum*, vol. 47, no. 10, pp. 1223–1225, Oct. 1996.

[173] P. R. McCurdy, J. M. Truitt, and E. R. Fisher, "Pulsed and continuous wave plasma deposition of amorphous, hydrogenated silicon carbide from SiH[sub 4]/CH[sub 4] plasmas," *J. Vac. Sci. Technol. A Vacuum, Surfaces, Film.*, vol. 17, no. 5, p. 2475, 1999.

[174] A. Jean, M. Chaker, Y. Diawara, P. K. Leung, E. Gat, P. P. Mercier, H. Pépin, S. Gujrathi, G. G. Ross, and J. C. Kieffer, "Characterization of a-SiC:H films produced in a standard plasma enhanced chemical vapor deposition system for x-ray mask application," *J. Appl. Phys.*, vol. 72, no. 7, pp. 3110–3115, 1992.

[175] F. Ibrahim, J. I. B. Wilson, and P. John, "Photo-oxidation of a-Si : C : H films," *J. Non. Cryst. Solids*, vol. 164–166, pp. 1051–1054, Dec. 1993.

[176] M. S. Brandt and M. Stutzmann, "Spin-dependent effects in porous silicon," *Appl. Phys. Lett.*, vol. 61, no. 21, pp. 2569–2571, 1992.

[177] M. López, B. Garrido, C. García, P. Pellegrino, A. Pérez-Rodríguez, J. R. Morante, C. Bonafos, M. Carrada, and A. Claverie, "Elucidation of the surface passivation role on the photoluminescence emission yield of silicon nanocrystals embedded in SiO2," *Appl. Phys. Lett.*, vol. 80, no. 9, pp. 1637–1639, 2002.

[178] K. S. Min, K. V. Shcheglov, C. M. Yang, H. a. Atwater, M. L. Brongersma, and A. Polman, "Defect-related versus excitonic visible light emission from ion beam synthesized Si nanocrystals in SiO2," *Appl. Phys. Lett.*, vol. 69, no. 14, p. 2033, 1996.

[179] S. P. Withrow, C. W. White, A. Meldrum, and J. D. Budai, "Effects of hydrogen in the annealing environment on photoluminescence from Si nanoparticles in SiO2," *J. Appl. Phys.*, vol. 86, no. 1, pp. 396–401, 1999.

[180] W. L. Ng, M. a Lourenço, R. M. Gwilliam, S. Ledain, G. Shao, and K. P. Homewood, "An efficient room-temperature silicon-based light-emitting diode.," *Nature*, vol. 410, no. 6825, pp. 192–4, Mar. 2001.

[181] L. Heikkilä, T. Kuusela, and H.-P. Hedman, "Electroluminescence in Si/SiO[sub 2] layer structures," *J. Appl. Phys.*, vol. 89, no. 4, p. 2179, 2001.

[182] A. Morales-Sánchez, K. Monfil-Leyva, A. A. González-Fernández, M. Aceves-Mijares, J. Carrillo, J. A. Luna-López, C. Domínguez, G. H.-K. Barreto, and F. J. Flores-Gracia,

"Strong blue and red luminescence in silicon nanoparticles based light emitting capacitors," *Appl. Phys. Lett.*, vol. 99, no. 17, p. 171102, 2011.

[183] S. Yerci, R. Li, and L. Dal Negro, "Electroluminescence from Er-doped Si-rich silicon nitride light emitting diodes," *Appl. Phys. Lett.*, vol. 97, no. 8, p. 81109, 2010.

[184] S. Prucnal, L. Rebohle, and W. Skorupa, "Electroluminescence from Er and Yb co-doped silicon dioxide layers: The excitation mechanism," *J. Non. Cryst. Solids*, vol. 357, no. 3, pp. 915–918, Feb. 2011.

[185] W. Zhang, S. Zhang, M. Yang, Z. Liu, and Z. Cen, "Electroluminescence of as-sputtered silicon-rich SiOx films," *Vacuum*, vol. 84, no. 8, pp. 1043–1048, 2010.

# VITA

Shakil Mohammed was born in Dhaka, Bangladesh on December 25, 1980. After completing his higher secondary certificate from the prestigious Notre Dame College in 1999, he went on to pursue his bachelor's degree in physics from the University of Dhaka. He was ranked as the top student in the graduating class of 2003 and was awarded the Prof. Ali Imam gold medal for his outstanding achievement at the university. He completed his master's degree in physics from the University of South Carolina in 2009 and afterwards moved to UT Dallas to further continue his PhD in the materials science and engineering program.

Shakil has two younger siblings and is the father of two daughters. He loves teaching and reading.

**List of publications and presentations:**

1. F. Deku, **S. Mohammed**, J. Maeng, V. R. Danda, A. Imre-Joshi, T. J. Gardner, and S. F. Cogan, *Effect of Oxidation on the Residual Stress of Amorphous Silicon Carbide Films* (In preparation).
2. L. A. Walsh, **S. Mohammed**, S. C. Sampat, Y. J. Chabal, A. V. Malko, and C. L. Hinkle, *Oxide-related defects in quantum dot containing Si-rich silicon nitride*. Applied Surface Science (Submitted).
3. Moreno, S., Baniasadi, M., **Mohammed, S.**, Mejia, I., Chen, Y., Quevedo-Lopez, M. A., Kumar, N., Dimitrijevich, S., and Minary-Jolandan, M., *Biocompatible Collagen Films as Substrates for Flexible Implantable Electronics*, Advanced Electronic Materials (2015).
4. **S. Mohammed,** M. T. Nimmo, A. V. Malko, and C. L. Hinkle, *Chemical bonding and defect states of LPCVD deposited silicon-rich $Si_3N_4$ for quantum dot applications*, Journal of Vacuum Science and Technology A **32**, 021507 (2014).
5. A. C. Duran-Martinez, F. Deku, **S. Mohammed**, A. Joshi-Imre, A. Garcia-Sandoval, S. F. Cogan, W. E. Voit, *Plasma-enhanced chemical vapor deposited silicon carbide as encapsulation layer for flexible neural interfaces*, XXV International Materials Research Congress, Mexico, 18 August 2016.
6. **S. Mohammed**, M. T. Nimmo, Y. J. Chabal, A. V. Malko, and C. L. Hinkle, *Chemical bonding and defect states in Si quantum dots embedded in $Si_3N_4$*, 2012 Materials Research Society Fall Meeting, Boston, MA, 25 – 30 November 2012, contributed speaker.